D3.10 Validation Report

This project has received funding from the European Union's Horizon 2020 research and innovation programme under grant agreement No 776348.

Project no.	776348
Project acronym:	CoastObs
Project title:	Commercial service platform for user-relevant coastal water monitoring services based on Earth Observation
Instrument:	H2020-EO-2017
Start date of project:	01.11.2017
Duration:	36 months
Deliverable title:	D3.10 Validation Report
Due date of deliverable:	Month 24

Organisation name of lead contractor for this deliverable: *USTIR*

Author list:

Name	Organisation
Caitlin Riddick	University of Stirling
Shenglei Wang	University of Stirling
Evangelos Spyrakos	University of Stirling
Peter Hunter	University of Stirling
Andrew Tyler	University of Stirling
Federica Braga	Consiglio Nazionale Delle Ricerche
Vittorio Brando	Consiglio Nazionale Delle Ricerche
Gian Marco Scarpa	Consiglio Nazionale Delle Ricerche
Laura Zoffoli	Universite de Nantes
Pierre Gernez	Universite de Nantes
Laurent Barillé	Universite de Nantes
Anne-Laure Barillé	Bio-Littoral
Nicolas Harin	Bio-Littoral
Luis Gonzalez Vilas	Universidad de Vigo
Jesus Torres Palenzuela	Universidad de Vigo
Tony van der Hiele	HZ University of Applied Sciences
Steef Peters	Water Insight

This project has received funding from the European Union's Horizon 2020 research and innovation programme under grant agreement No 776348

History			
Version	**Date**	**Reason**	**Revised by**
01	01/10/2019	Draft outline	Caitlin Riddick, USTIR
02	23/10/2019	Draft for internal review	Caitlin Riddick, USTIR Shenglei Wang, USTIR
03	29/10/2019	Internal Review	Evangelos Spyrakos, USTIR
04	31/10/2019	Internal Review	Anne-Laure Barillé, Bio-Littoral
05	31/10/2019	Revisions to Draft	Caitlin Riddick, USTIR Shenglei Wang, USTIR

Dissemination level		
PU	Public	X
CO	Confidential, restricted under conditions set out in Model Grant Agreement	
CI	Classified, information as referred to in Commission Decision 2001/844/EC	

Please cite as:

Riddick, C., Wang, S., Spyrakos, E., Hunter, P., Tyler, A., Braga, F., Brando, V., Scarpa, G., Zoffoli, L., Gernez, P., Barille, A-L., Barille, L., Harin, N., Gonzalez Vilas, L., Torres Palenzuela, J., van der Hiele, T., Peters, S. (2019). D3.10 Validation Report. CoastObs Project.

CoastObs Project

CoastObs is an EU H2020 funded project that aims at using satellite remote sensing to monitor coastal water environments and to develop a user-relevant platform that can offer validated products to users including monitoring of seagrass and macroalgae, phytoplankton size classes, primary production, and harmful algae as well as higher level products such as indicators and integration with predictive models.

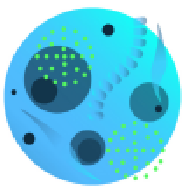
phytoplankton


seagrass


harmful algal blooms


primary production

To fulfil this mission, we are in dialogue with users from various sectors including dredging companies, aquaculture businesses, national monitoring institutes, among others, in order to create tailored products at highly reduced costs per user that stick to their requirements.

With the synergistic use of Sentinel-3 and Sentinel-2, CoastObs aims at contributing to the sustainability of the Copernicus program and assisting in implementing and further fine-tuning of European Water Quality related directive.

This project has received funding from the European Union's Horizon 2020 research and innovation programme under grant agreement No 776348

Partnership

Water Insight BV. (WI)

The University of Stirling (USTIR)

Consiglio Nazionale Delle Ricerche (CNR)

Universite de Nantes (UN)

HZ University of Applied Sciences (HZ)

Universidad de Vigo (UVIGO)

Bio-Littoral (BL)

Geonardo Environmental Technologies Ltd. (GEO)

This project has received funding from the European Union's Horizon 2020 research and innovation programme under grant agreement No 776348

Contents

Abbreviations and symbols 14

1 Summary 18

2 Introduction 19

2.1 Product Validation Method 20

2.2 Summary of CoastObs validation campaigns 21

3 CoastObs Product Validation (2018) 25

3.1 Basic Products 25

3.1.1 Remote sensing reflectance 25

3.1.2 Chlorophyll-*a* (Chl-*a*) 54

3.1.3 Total Suspended Matter (TSM) and Turbidity 69

3.1.4 Sea surface temperature (SST) 84

3.1.5 Euphotic Depth (Z_{eu}) 89

3.1.6 Daily irradiance (E_0) 90

3.2 Innovative and Supplementary Products 92

3.2.1 Seagrass and Macro-Algae (SMA) 92

3.2.2 Phytoplankton Size Classes (PSC) 104

3.2.3 Primary Production (PP) 112

3.2.4 Harmful Algal Blooms and Indicator Species (HABs) 120

3.3 Higher level products 122

3.3.1 Integration with modelling: mussel culture potential 122

4 References 125

This project has received funding from the European Union's Horizon 2020
research and innovation programme under grant agreement No 776348

FIGURES

Figure 1 - Locations of CoastObs field campaigns from 2018-2019 23

Figure 2- Map of 2018-2019 CoastObs stations in Venice Lagoon and Adriatic Sea, Italy 23

Figure 3- Map of 2018-2019 CoastObs stations in Ria de Vigo, Spain.. 24

Figure 4- Map of 2018-2019 CoastObs stations in (a) Wadden Sea and (b) Oosterschelde, Netherlands 24

Figure 5- Map of 2018-2019 CoastObs stations in (a) Borgenouf bay and (b) Glenan Archipelago, France 25

Figure 6- Study area with location of fieldwork activities carried out from January to May 2019 (red dots: measurement stations on 20th March 2019 in the central sector of the LV; yellow dots: revisited stations at the Lido inlet).. 31

Figure 7 - Validation scatterplots for R_{rs} CoastObs product, indicating R^2 and linear regression fit.... 32

Figure 8 - Validation scatterplots between *in situ* R_{rs} from WISP-3 and R_{rs} from Sentinel-3 using: a) Polymer; b) C2RCC; c)augC2RCC; d) WFR. 34

Figure 9- Validation scatterplots between *in situ* R_{rs} from WISP-3 and R_{rs} from Sentinel-3 using: a) ACOLITE; b) C2RCC; c)C2X; d) Polymer. 35

Figure 10 - Validation scatterplots for Sentinel-2 MSI C2RCC atmospheric correction, indicating R^2 and linear regression fit at each band 37

Figure 11 - Validation scatterplots for Sentinel-2 MSI Polymer atmospheric correction (v4.9), indicating R^2 and linear regression fit at each band 38

Figure 12 - Validation scatterplots for Sentinel-2 MSI ACOLITE atmospheric correction, indicating R^2 and linear regression fit at each band 38

Figure 13 - Validation scatterplots for Sentinel-2 MSI C2X atmospheric correction, indicating R^2 and linear regression fit at each band 38

Figure 14 - Validation scatterplots for Sentinel-2 MSI iCOR atmospheric correction, indicating R^2 and linear regression fit at each band (B4-B8A not shown due to zero values for all iCOR R_{rs} at these bands) 39

Table 10 – Error metrics for Sentinel-2 MSI C2RCC atmospheric correction at each band, for the combined Venice and Vigo 2018 datasets (n=49) 40

Figure 15 - Validation scatterplots for Sentinel-3 OLCI C2RCC atmospheric correction, indicating R^2 and linear regression fit at each band (Bands Oa1-Oa12) 41

This project has received funding from the European Union's Horizon 2020 research and innovation programme under grant agreement No 776348

Figure 16 - Validation scatterplots for Sentinel-3 OLCI Polymer v4.9 atmospheric correction, indicating R^2 and linear regression fit at each band (Bands Oa1-Oa16) 42
Figure 17 - Location of the pixel extraction location relative to the actual measurement station 45
Figure 18 - Validation results, expressed in MAPE (Mean Absolute Percentage Error) values, of atmospheric correction for Sentinel-3 45
Figure 19 - Validation results, expressed in MAPE values, of atmospheric correction for Sentinel-2 .. 46
Figure 20 - Validation measures for the mean spectra for S2..... 46
Figure 21 - ACOLITE: Validation result of mean spectra..... 47
Figure 22 - ACOLITE: Validation result of actual spectra. 47
Figure 23 - C2X: Validation result of mean spectra. 48
Figure 24 - C2X: Validation result of actual spectra. 48
Figure 25 - C2RCC: Validation result of actual spectra (left) and mean spectra (right) 48
Figure 26 - Mean values of the resulting spectra. The dashed lines (u/l) are the upper and lower bounds of *in situ* spectra. Aco stands for ACOLITE..... 49
Figure 27 - Validation scatterplot for Reflectance in intertidal areas in Bourgneuf bay during 2018 and 2019, indicating R^2 and linear regression fit..... 51
Figure 28 - Validation scatterplot for R_{rs} over shallow waters in the Glenan Archipelago during 2019, including bands 1 to 5 (443- 705 nm)..... 53
Figure 29 - Example map of stations for validation of R_{rs} over shallow waters 54
Figure 30 - Validation scatterplots for Venice 2018 Sentinel-2 Chl-*a* (unit: mg/m^3), indicating R^2 and linear regression fits 56
Figure 31 - Validation scatterplots for Venice 2018 Sentinel-3 Chl-*a* (unit: mg/m^3), indicating R^2 and linear regression fits 58
Figure 32 - Example map of Sentinel-3 Chl-*a* product (Colour Index) for Venice Lagoon, Italy on 26 June 2018. 59
Figure 33 - Validation of S3 derived Chl-*a* concentrations using the Eemshaven data set..... 60
Figure 34 - Validation of S2 derived Chl-*a* concentrations using the Eemshaven data set..... 61
Figure 35 - Validation scatterplots for S3 standard Chl-*a* product for the study areas Oosterschelde estuary (n=47) and Wadden Sea (n=17), indicating R^2 and linear regression fit. 62
Figure 36 - Example map of S3 standard CoastObs Chl-*a* product (unit: mg/m^3) for the Wadden Sea study area on 03.05.2018. Intertidal areas are excluded. 63

This project has received funding from the European Union's Horizon 2020 research and innovation programme under grant agreement No 776348

Figure 37 - Validation scatterplots for the Vigo 2018 Sentinel-2 Chl-*a* product (unit: mg/m^3), indicating R^2 and linear regression fits 64
Figure 38 - Validation scatterplots for Vigo 2018 Sentinel-3 Chl-*a* (unit: mg/m^3), indicating R^2 and linear regression fit 65
Figure 39 - Example map of Sentinel-3 Chl-*a* product (NDCI) for Galician Rias, Spain on 08 July 2018. 66
Figure 40 - Validation scatterplots obtained from the independent test dataset. a) NNRB-Cl#1 b) NNRB-Cl#2 67
Figure 41 - Chl-*a* map from NNRB-Cl#2 for 19 June 2018 69
Figure 42 - Validation scatterplot for TSM CoastObs product, indicating R^2 and linear regression fit. 71
Figure 43 - a) Study area with location of fieldwork activities carried out from January to May 2019 (red dots: measurement stations on 20th March 2019 in the central sector of the LV; yellow dots: revisited stations at the Lido inlet; b) Zoom on the revisited stations at the Lido inlet; c) Coordinates of the revisited stations at the Lido inlet. 73
Figure 44 - Validation scatterplot(s) for Turbidity CoastObs product, indicating R^2 and linear regression fit. a) Sentinel-2; b) Landsat 8. In both plots, the number of samples (n) and the 1:1 line is plotted as dotted lines. 75
Figure 45 - Example maps of Turbidity CoastObs product for 24.01.2019. a) Sentinel-2 (overpass time 10:13 UTC); b) Landsat 8 (overpass time 09:58 UTC). 76
Figure 46 - The intercomparison of Turbidity products for near-simultaneous overpasses of L8 and S2 with the available matchups (3 field campaigns). On the left, the S2 pseudo true-color images, corresponding to the match-ups. 77
Figure 47 - Validation scatterplot(s) for SPM CoastObs product, indicating R^2 and linear regression fit. a) Sentinel-2; b) Landsat 8. In both plots, the number of samples (n) and the 1:1 line is plotted as dotted lines. 79
Figure 48 - Example map of SPM CoastObs product for S2 acquired on 20.03.2019 80
Figure 49 -The intercomparison of *in situ* Turbidity and SPM/SPIM concentration. 80
Figure 50 - Validation of S3-SPM products using the Eemshaven data set. Outliers are highlighted in red boxes but not excluded for the Goodness of Fit (GoF) parameter calculations 81
Figure 51 - Validation of S2 derived SPM concentrations using the Eemshaven data set. GoF parameters calculated without excluding the outlier in the red box. 82

This project has received funding from the European Union's Horizon 2020 research and innovation programme under grant agreement No 776348

Figure 52 - Validation scatterplot(s) for TSM CoastObs product in Ria de Vigo, respectively, indicating R^2 and linear regression fit for the Vigo 2018 dataset 83
Figure 53 - Example map of TSM products for the Galician coastal waters, Spain (8 July 2018)......... 84
Figure 54 - Validation scatterplot for the Sea Surface Temperature (SST) product, indicating R^2 and linear regression fit.. 85
Figure 55 - Example map of GHRSST product for 03.06.2019 (SST, Kelvin) 86
Figure 56 - Location of SST *in situ* stations in the Wadden Sea, Netherlands.................................... 87
Figure 57 - Scatterplot *in situ* (daily median) versus GHRSST 1km data for SST for the 7 stations in the study area (2017)... 87
Figure 58 - Scatterplot *in situ* (2-hour median) versus Landsat8 data for SST for the 24 stations in the Wadden Sea (2017) 88
Figure 59 - Calibration scatterplot to tune Zeu as a functin oof R_{rs} (560)/ R_{rs} (490) (left) and validation scatterplot(s) for Euphotic Depth (Z_{eu}; m), indicating R^2 and linear regression fit (right).................... 90
Figure 60 - Calibration scatterplot to tune Meteosat SSI as a function of *in situ* daily modelled irradiance, E0, (left) and validation scatterplot for E0, indicating R^2 and linear regression fit (right).. 91
Figure 61 - Algorithm validation for seagrass percent cover as a function of NDVI. Red dots correspond to Bourgneuf bay dataset collected in 2018; blue dots correspond to Bourgneuf bay dataset collected in 2019; and green dots correspond to Marenne Oléron dataset collected in 2019.......................... 93
Figure 62 - Validation of seagrass percent cover product. It is shown R^2 and linear regression fit..... 94
Figure 63 - Spatial distribution of stations used to validate seagrass percent cover CoastObs product in 2018 over intertidal areas 95
Figure 64 - Example map seagrass percent cover CoastObs product over intertidal areas in 2018.... 95
Figure 65 - Validation scatterplot for depth CoastObs product derived from *in situ* radiometric data, as hyperspectral data (blue dots) and simulated S2 bands.. 97
Figure 66 - Validation scatterplot for CoastObs product derived from *in situ* radiometric data in shallow waters, as hyperspectral data (blue dots) and simulated S2 bands: (a) sand percent cover, (b) seagrass percent cover (SPC), (c) macroalgae percent cover (MPC), and (d) vegetation percent cover (VPC). . 99
Figure 67 - Validation scatterplot for CoastObs product derived from Sentinel2 acquired on the 6/7/2019 in shallow waters: (a) sand percent cover, (b) seagrass percent cover (SPC), (c) macroalgae percent cover (MPC), and (d) vegetation percent cover (VPC).. 100
Figure 68 - Validation stations sampled in the Glénan Archipelago during July/2019 102
Figure 69 - Example map of seagrass percent cover CoastObs product for 06.07.2019 102

This project has received funding from the European Union's Horizon 2020 research and innovation programme under grant agreement No 776348

Figure 70 - Example map of macroalgae percent cover CoastObs product for 06.07.2019 103
Figure 71 - Example map of vegetation percent cover CoastObs product for 06.07.2019 103
Figure 72 - Validation scatterplot(s) for the Abundance-based PSC CoastObs product, indicating R^2 and linear regression fit for the Vigo 2018 dataset for C1 (picophytoplankton), C2 (nanophytoplankton) and C3 (microphytoplankton) Chl-*a* (note there were no picoplankton present in 2018). 104
Figure 73 - Validation scatterplot(s) for the Abundance-based PSC CoastObs product, indicating R^2 and linear regression fit for the Venice 2018 dataset for C1 (picophytoplankton), C2 (nanophytoplankton) and C3 (microphytoplankton) Chl-*a* 104
Figure 74 - Example map of Abundance-based 3-class PSC products for the Galician coastal waters, Spain (8 July 2018) 106
Figure 77 - Validation scatterplot for *in situ* m2VGPM depth integrated Primary Productivity (PP_{eu}) as a function of Act2 Primary Productivity, indicating R^2 and linear regression fit 115
Figure 78 - Validation scatterplot for S3 NDCI Chl-a product tuned with the Vigo and Venice 2019 dataset, indicating R^2 and linear regression fit 116
Figure 79 - Validation scatterplot for the Primary Productivity (PP_{eu}) CoastObs product, indicating R^2 and linear regression fit (note for Act2 *in situ* PP, $\phi_{E:C}$= 20 mol e- mol C^{-1}). 118
Figure 80 - Example map of PP_{eu} CoastObs product for the Venice Lagoon, Italy, 16.07.2019 119
Figure 81 - Bloom probability map on 1 August 2018 obtained using the *Pseudo-nitzschia* spp. indicator 121
Figure 82 - Validation scatterplots for modeled shell length output (cm) from the spatio temporal mussel growth DEB model and observed growth in the Oosterschelde estuary and Wadden Sea, indicating R^2 and linear regression fit. Open circles represent 2017 data, black circles 2018 data. .. 123
Figure 83 - Example of monthly aggregates from DEB model outputs transformed to relative growth rate (lenght increase in %) for the Wadden Sea in 2018 124

This project has received funding from the European Union's Horizon 2020 research and innovation programme under grant agreement No 776348

TABLES

Table 1 – Summary of dedicated CoastObs field campaign efforts for product validation 21

Table 2 – List of Sentinel-2 atmospheric corrections tested 26

Table 3 – List of Sentinel-3 atmospheric corrections tested 27

Table 4 Performance of atmospheric correction algorithms over studied regions 28

Table 5– Expeditive fieldworks carried out in the LV to validate CoastObs standard products 30

Table 6 – Error metrics for R_{rs} CoastObs product 33

Table 7 – Error metrics comparing *in situ* R_{rs} from WISP-3 and Sentinel-3 using different atmospheric correction algorithms. 34

Table 8 - Error metrics comparing *in situ* R_{rs} from WISP-3 and Sentinel-2 using different atmospheric correction algorithms. 35

Table 9 – Error metrics for Sentinel-2 MSI Polymer atmospheric correction at each band, for the combined Venice and Vigo 2018 datasets (n=42) 39

Table 10 – Error metrics for Sentinel-2 MSI C2RCC atmospheric correction at each band, for the combined Venice and Vigo 2018 datasets (n=49) 40

Table 11 – Error metrics for Sentinel-3A OLCI C2RCC atmospheric correction for bands Oa1-Oa12, for the combined Venice and Vigo 2018 datasets (n=44).. 42

Table 12 – Error metrics for Sentinel-3A OLCI Polymer atmospheric correction for bands Oa1-Oa12, for the combined Venice and Vigo 2018 datasets (n=60).. 43

Table 13 - Validation measures for the mean spectra for S3. 46

Table 14 - Validation measures for the mean spectra. 49

Table 15 - Validation measures of actual spectra. 49

Table 16 - Error metrics for Reflectance CoastObs product in Bourgneuf Bay over intertidal areas ... 52

Table 17 - Error metrics for R_{rs} CoastObs product in the Glenan Archipelago over shallow waters, computed independently for bands 1 to 5 (443 to 705 nm).. 53

Table 18 - Best-performing Chl-a algorithms by region 55

Table 19 - Error metrics for CoastObs Sentinel-2 Chl-*a* product (unit: mg/m^3), Venice 2018 dataset (n=12) 56

Table 20 - Error metrics for CoastObs Sentinel-3 Chl-*a* product (unit: mg/m^3), Venice 2018 dataset (n=11) 58

Table 21- Accuracy of S2 and S3 retrievals of Chl-*a* 61

Table 22 - Error metrics for S3 standard Chl-*a* product for the Netherlands 62
Table 23 - Error metrics for CoastObs Sentinel-2 Chl-*a* product (unit: mg/m^3), Vigo 2018 dataset (n=29) 64
Table 24 - Error metrics for CoastObs Sentinel-3 Chl-*a* product (unit: mg/m^3), Vigo 2018 dataset (n=14) 66
Table 25 - Error metrics for NNRB-Cl#1 and NNRB-Cl#2, computed from the datasets used for the developent of the algorithms and from the independent test set. 68
Table 26 - Best-performing TSM and turbidity algorithms by region 70
Table 27 - Error metrics for TSM CoastObs product 71
Table 28 - Error metrics for Turbidity CoastObs products 76
Table 29 - Error metrics for SPM CoastObs products 79
Table 30 - Overall accuracy of S2 and S3 retrievals of SPM for the Netherlands 82
Table 31 - Error metrics for TSM CoastObs product in Ria de Vigo 83
Table 32 - Error metrics for SST CoastObs product 85
Table 33 - Statistics for SST retrieval for GHRSST data in the Netherlands 88
Table 34 - Statistics for SST retrieval for medium resolution data in the Netherlands 89
Table 35 - Error metrics for Z_{eu} CoastObs product 90
Table 36 – Error metrics for the daily PAR, E_0, CoastObs product 92
Table 37 - Error metrics for seagrass percent cover CoastObs product in intertidal areas 94
Table 38 – Error metrics for depth CoastObs product 97
Table 39 – Error metrics for seagrass percent cover (SPC) CoastObs product 101
Table 40 - Error metrics for macroalgae percent cover (MPC) CoastObs product 101
Table 41 - Error metrics for vegetation percent cover (VPC) CoastObs product 101
Table 42 – Error metrics for Abundance-based PSC CoastObs product 105
Table 43 - Error metrics for absorption-based PSC CoastObs product 111
Table 44 - Error metrics for *in situ* m2VGPM PP_{eu} 115
Table 45 - Error metrics for 2019 NDCI Chl-a product 117
Table 46 - Error metrics for satellite m2VGPM PP_{eu} product (2019 dataset) 119
Table 47 - A confusion matrix indicating instances of true positives (TP), true negatives (TN), false positives (FP) and false negatives (FN). It was obtained applying the *Pseudo-nitzschia* spp. indicator to the complete dataset (development + test). 120
Table 48 - Error metrics for the *Pseudo-nitzschia* spp. indicator 121

This project has received funding from the European Union's Horizon 2020 research and innovation programme under grant agreement No 776348

Table 49 - Error metrics for higher level CoastObs product Spatio temporal DEB model for mussel growth 123

Abbreviations and symbols

Abbreviation/symbol	Description
a	Absorption coefficient
a^*_{chl}	Chlorophyll-specific absorption coefficient of phytoplankton cells
a^*_{ci}	Specific absorption coefficient of Chl-a inside a cell
a_{cm}	Absorption coefficient of the cell material
a_{ph}	Phytoplankton absorption coefficient
a_w	Water absorption coefficient
AC	Atmospheric correction
AOP	Apparent optical propertY
b_b	Backscattering coefficient
BOA	Bottom of atmosphere
C	Carbon
CDOM	Colored dissolved organic matter
Chl-*a*	Chlorophyll-a concentration
CI	Color Index
D	Cell diameter
E_0	Daily irradiance
E_s	Downwelling irradiance
E_{wu}	Upwelling irradiance below water
EO	Earth Observation
ESA	European Space Agency
FLC	Fluorescence light curve
FNU	Formazin nephelometric unit
FRRf	Fast repeitition rate fluorometry
GHRSST	Group for high resolution sea surface temperature
GoF	Goodness of Fit
Gons-m	The Gons modification algorithm

This project has received funding from the European Union's Horizon 2020 research and innovation programme under grant agreement No 776348

Abbreviation/symbol	Description
HABs	Harmful algal blooms
HPLC	High-performance liquid chromatography
IOP	Inherent optical property
JV_{PSII}	PSII electron flux
K	Kappa statistic
K_d	Diffuse attenuation coefficient
LED	Light emitting diodes
L_s	Sky radiance
L_t	Spectral water-leaving radiance
L_u	Upwelling radiance above water
L_{wu}	Upwelling radiance below water
LV	Lagoon of Venice
m2VGPM	A modified version of the Vertically Generalised Production Model
MAE	Mean absolute error
MAPE	Mean absolute percentage error
MSI	Multispectral Instrument onboard Sentinel-2
MW_c	Molecular weight of carbon
NNRB	Neural Network for *rias* Baixas
OA	Overall accuracy
OC3E	NASA Ocean colour standard 3-band algorithm for MERIS bands
OC4E	NASA Ocean colour standard 4-band algorithm for MERIS bands (https://oceancolor.gsfc.nasa.gov/atbd/chlor_a/)
OC4Me	Sentinel-3 Ocean colour standard 4-band algorithm for MERIS bands (https://sentinel.esa.int/web/sentinel/technical-guides/sentinel-3-olci/level-2/oc4me-chlorophyll)
OLCI	Ocean and Land Colour Instrument onboard Sentinel-3
PAR	Photosynthetic available radiation
P^B_{opt}	Maximum Carbon fixation rate

This project has received funding from the European Union's Horizon 2020 research and innovation programme under grant agreement No 776348

Abbreviation/symbol	Description
PC_{FRRf}	Rate of carbon fixation
PP	Primary production
PSC	Phytoplankton size class
PSII	Photosystem II
Q_a	Dimensionless absorption efficiency of a cell
QAA	Quasi-analytical Algorithm
R^2	Coefficient of determination
RMSE	Root mean square error
R_{rs}	Remote-sensing reflectance
S2	Sentinel-2
S3	Sentinel-3
SDI	Substrate detectability index
SMA	Seagrass and Macro-Algae
SPC	Seagrass percent cover
SPM	Suspended particulate matter
SSI	Daily shortwave solar irradiance
SST	Sea surface temperature
SVM	Support vector machine
TFR	True false rate
TOA	Top of atmosphere
TPR	True positive rate
TSM	Total suspended matter
USGS	United States Geological Survey
WP	Work Package
Z_{eu}	Euphotic depth
ρ_c	Dimensionless optical thickness
ρ_s	Sky radiance reflectance on the water surface
ξ	The exponent of the phytoplankton size spectrum

This project has received funding from the European Union's Horizon 2020 research and innovation programme under grant agreement No 776348

Abbreviation/symbol	Description
$\varphi_{E:C}$	Electron requirement for carbon fixation

1 Summary

Rationale:

The aim of the H2020 CoastObs project is to develop a commercial service platform for user-relevant coastal water monitoring and environmental reporting based on validated Earth Observation (EO) and *in situ* optical data. As part of WP3, several innovative and higher level EO products were developed for use in coastal waters, primarily using the European Space Agency (ESA) Sentinel-2 and -3 satellite instruments (Multispectral Instrument (MSI) and Ocean and Land Colour Instrument (OLCI), respectively). This new generation of ESA Sentinel satellites provides improved spectral, temporal and spatial capabilities to monitor the coastal region from space. These data provide the opportunity to develop a products to monitor coastal waters that can be included in this service.

However, substantial validation is required in order to define the accuracy of the CoastObs products. Product validation will ensure each product is robust and fit-for-purpose. Clear and transparent error metrics for each product will also provide users with confidence in the CoastObs products and is therefore a fundamental process in advance of the service implementation. Therefore, several dedicated field campaigns were conducted in the coastal waters of France, Italy, the Netherlands and Spain during 2018-2019, where biogeochemical, radiometric and optical measurements were made in order to develop and test the CoastObs products. Thus, the results of these validation efforts will be presented in this deliverable for each CoastObs product and region, implementing the methods and error metrics as defined in the D2.4 Validation Plan.

Objective:

This deliverable presents the validation results for all CoastObs products, by region, satellite sensor and/or method. Both "basic" and innovative product validation are included in this deliverable, however the data and methods for products, if not described here, are included in the relevant deliverables for Product Documentation (D3.3, D3.4,D3.5 and D3.6) and Higher Level Products (D3.8). Additionally, as the 2019 field season has recently concluded, this deliverable includes validation results for the 2018 field campaigns, unless otherwise specified.

This project has received funding from the European Union's Horizon 2020 research and innovation programme under grant agreement No 776348

2 Introduction

The aim of the H2020 CoastObs project is to develop a commercial service platform for user-relevant coastal water monitoring and environmental reporting based on validated Earth Observation (EO) and *in situ* optical data. As part of WP3, several innovative and higher level EO products were developed for use in coastal waters, primarily using the European Space Agency (ESA) Sentinel-2 and -3 satellite instruments (Multispectral Instrument (MSI) and Ocean and Land Colour Instrument (OLCI), respectively). This new generation of ESA Sentinel satellites provides improved spectral, temporal and spatial capabilities to monitor the coastal region from space. It is in this context that the CoastObs products were developed, in order to make the most of freely accessible EO data to develop a coastal monitoring service.

Dedicated field campaigns were conducted in the coastal waters of France, Italy, the Netherlands and Spain in 2018-2019, during which biogeochemical, radiometric and optical measurements were made in order to test and develop these products for use in the CoastObs service. Over 680 stations were sampled over all regions during the course of these campaigns, producing a vast validation dataset for product testing and development of CoastObs products. As the 2019 field season has only just finished, this deliverable will focus on the validation results for the 2018 field campaigns only, unless otherwise specified.

These novel CoastObs products require validation in order to ensure they are robust and fit-for-purpose. Validation can be defined as the process of assessing the reliability of the data products derived from a system output with independent means (Kleywegt, 2007). The validation methods for use with quantitative and qualitative data were described in detail in D2.4 Validation Plan, and summarised in Section 2.1. Clear and transparent error metrics for each product will provide users with confidence in the CoastObs products and is therefore a fundamental component of the product development stage. It is of great importance to understand the errors associated with the measurements and resulting products first, in order to ensure that the products can then be implemented reliably in the service.

This deliverable presents the validation results for all CoastObs products, by region, satellite sensor and/or method. First, the "basic" products are demonstrated, including satellite remote sensing reflectance ($R_{rs}(\lambda)$; i.e. atmospheric correction validation), chlorophyll-a (Chl-*a*; a proxy for total phytoplankton biomass), total suspended matter (TSM) or suspended particulate matter (SPM), turbidity, sea surface temperature (SST), euphotic depth (Z_{eu}; the depth at which photosynthetically available radiation (PAR) is 1% of the surface PAR), and daily irradiance or PAR (E_0). These basic CoastObs products are the best-performing algorithms for each region, derived either from existing or re-tuned algorithms, and are the building blocks for the innovative and higher level products.

This project has received funding from the European Union's Horizon 2020 research and innovation programme under grant agreement No 776348

Secondly, we present validation of the CoastObs innovative products in this deliverable, building on the robust basic products. These include seagrass and macroalgae (SMA), phytoplankton size classes (PSC), primary productivity (PP) and harmful algal blooms (HABs). The data and methods for these products were described in the relevant Product Documentations (D3.3, D3.4, D3.5 and D3.6), however any details not included in these previous deliverables is presented here. The validation results for the innovative products are shown by region or method. Lastly, validation for the higher level product mussel culture potential is presented, however all higher level products are described in detail elsewhere (D3.8 Higher Level Products Report).

2.1 Product Validation Method

The error metrics for product validation have been described in detail in the preceding CoastObs deliverable, D2.4 Validation Plan. As a single index is unlikely to adequately describe model performance, a suite of complementary measures is used to report accuracy of each product.

The Validation Plan outlined the error measures for validation of **quantitative** data as follows:

- Intercept (b) and slope (a) of a regression line of a scatterplot of EO retrieved data vs. *in situ* or laboratory measured data (with a 1:1 prediction line)
- Root mean square error (RMSE)
- Mean absolute error (MAE)
- Bias

Additionally, the Validation Plan outlined the key methods for validation of **qualitative** data as follows:

- True false rate (TFR)
- True positive rate (TPR)
- Overall accuracy (OA)
- Kappa statistic (*K*)

Throughout this Validation Report, the appropriate metrics have been used to assess the best performing products. We have thus aimed to achieve product accuracy to the satisfaction of the users and their requirements.

This project has received funding from the European Union's Horizon 2020 research and innovation programme under grant agreement No 776348

2.2 Summary of CoastObs validation campaigns

A summary of the dedicated CoastObs field campaigns from 2018-2019 is provided in Table 1, with regional maps of 2018-2019 sampling stations presented in Figure 1-Figure 5.

Table 1 – Summary of dedicated CoastObs field campaign efforts for product validation

Country	Region	Survey Dates	Number of Stations	Biogeochemical data collected	IOPs / AOPs collected
France	Bourgneuf Bay	14 and 26 September 2018	20 for algorithm calibration; 54 for product validation	Percent cover and biomass of seagrass	R (ASD)
	Bourgneuf Bay	01 and 13 September 2019	59 for algorithm validation	Percent cover and biomass of seagrass	R (ASD)
	Marenne Oléron	03 September 2019	28 for algorithm validation	Percent cover of seagrass	R (ASD)
	Glénan Archipelago	08 to 11 July 2019	38 for R_{rs} validation; 210 for product validation	Bottom depth and bottom type percent cover	R_{rs} (ASD)
Italy	Venice Lagoon & Adriatic Sea	14 campaigns (January-May 2019)	120	SPM, SPIM, SPOM, Turbidity, Secchi depth, CTD profiles	R_{rs}(WISP-3)
Netherlands	Wadden Sea / NIOZ Jetty	2015-2017	1	R_{rs}(Trios)	R_{rs} (TriOS, WISP-3), IOPs (AC-S, BB3)

This project has received funding from the European Union's Horizon 2020 research and innovation programme under grant agreement No 776348

Country	Region	Survey Dates	Number of Stations	Biogeochemical data collected	IOPs / AOPs collected
	Wadden Sea / Eemshaven pole	2017	1	Chl-*a*, TSM	R_{rs} (TriOS, WISP-3), IOPs (AC-S, BB3)
	Wadden Sea	2017	7-24	SST	
Spain	Ria de Vigo	May -June 2018	73	Chl-*a*, TSM, CDOM, HPLC, pabs, fractionated Chl-*a*, fractionated pabs,	R_{rs} (TriOS, WISP-3), IOPs (AC-S, BB3)
		3-21 June 2019	53	Chl-*a*, TSM, CDOM, HPLC, pabs, fractionated Chl-*a*, FastOcean FLCs	R_{rs} (TriOS, WISP-3), IOPs (AC-S, BB3)

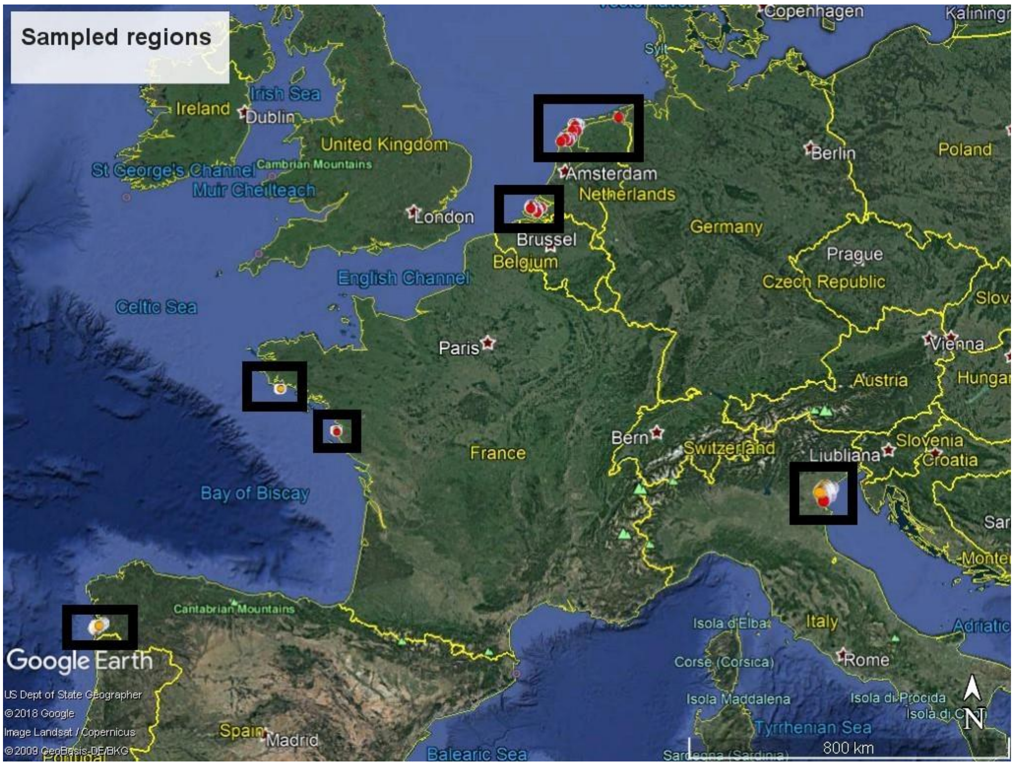

Figure 1 - Locations of CoastObs field campaigns from 2018-2019

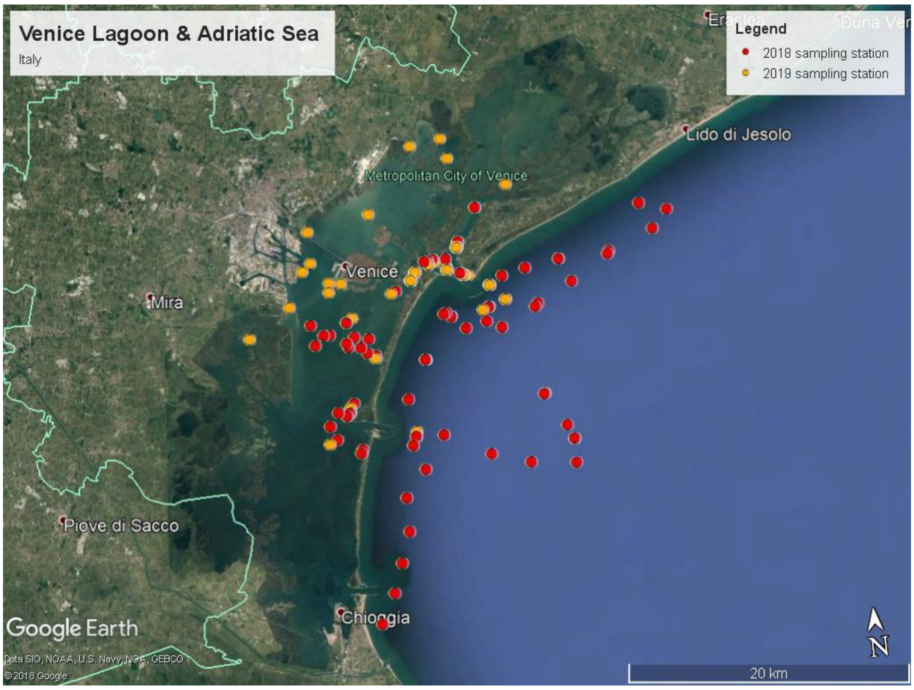

Figure 2- Map of 2018-2019 CoastObs stations in Venice Lagoon and Adriatic Sea, Italy

This project has received funding from the European Union's Horizon 2020
research and innovation programme under grant agreement No 776348

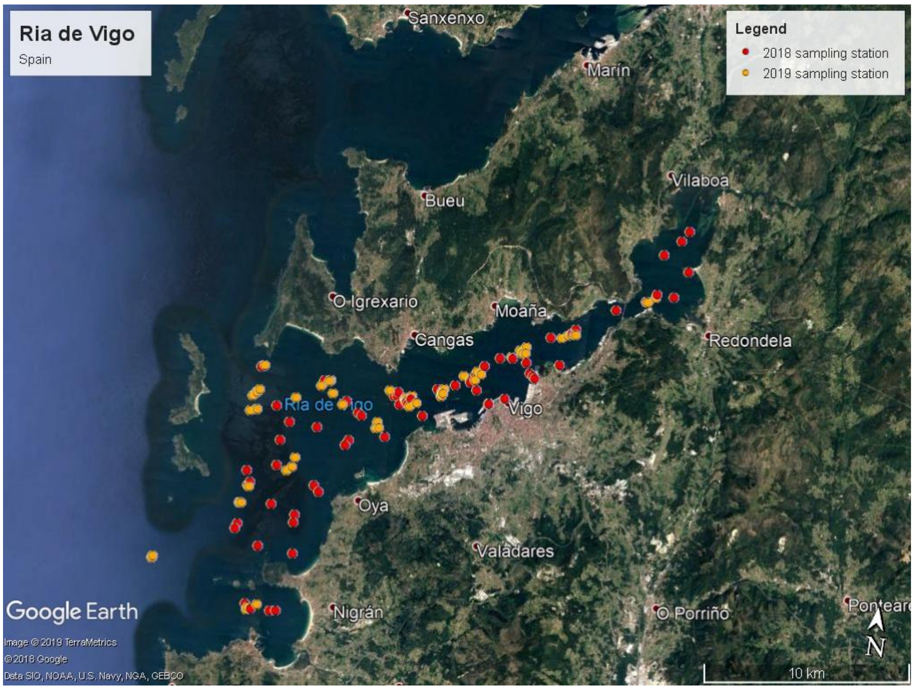

Figure 3- Map of 2018-2019 CoastObs stations in Ria de Vigo, Spain

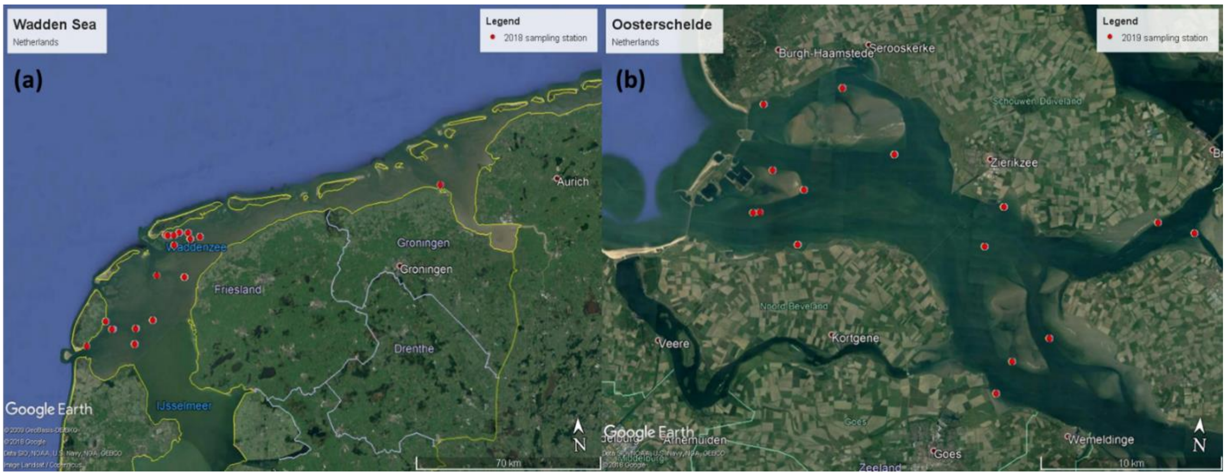

Figure 4- Map of 2018-2019 CoastObs stations in (a) Wadden Sea and (b) Oosterschelde, Netherlands

This project has received funding from the European Union's Horizon 2020 research and innovation programme under grant agreement No 776348

Figure 5- Map of 2018-2019 CoastObs stations in (a) Borgenouf bay and (b) Glenan Archipelago, France

3 CoastObs Product Validation (2018)

This Validation Report will cover primarily product validation results from 2018 field campaign data, as at this stage these data have been processed completely. However, the 2019 field data has been used on occasion where there were no data collected for 2018 (e.g. Primary Production). Validation of basic products are presented first, including remote sensing reflectance, chlorophyll-a (Chl-*a*), total suspended matter (TSM) and turbidity, sea surface temperature (SST), euphotic depth (Z_{eu}) and daily irradiance (E_0). This is followed by validation of the innovative and supplementary products, including Seagrass and Macro-algae (SMA), phytoplankton size classes (PSC), Primary Production (PP) and Harmful Algal Blooms (HABs). These products are described in detail in the relevant product documentation (D3.3, D3.4, D3.5 and D3.6), however any addition or change to the method for these products is outlined here. Finally, we present validation of the higher level CoastObs products, which are also described in further detail in the previous deliverable (D3.8).

3.1 Basic Products

3.1.1 Remote sensing reflectance

In order to produce robust CoastObs products, the remote sensing reflectance ($R_{rs}(\lambda)$) retrieved from atmospheric correction of the satellite data must first be validated.

This project has received funding from the European Union's Horizon 2020 research and innovation programme under grant agreement No 776348

Image preprocessing

The Sentinel-3 OLCI archive was processed using the Level 1 data available at Eumetsat's website. The first step was to remove cloudy, hazy, land and invalid pixels. This was done using the IdePix algorithm available at the SNAP 6.0 software (Lebreton et al., 2016). Finally, the valid pixels would be atmospherically corrected using corresponding processors. At this point, the processing results in 300 meter spatial resolution, atmospherically corrected flagged data of water leaving radiance reflectance (R_{rs}). No further processing took place, as we were interested to assess the quality of the AC comparing with available *in situ* datasets.

The Sentinel-2 MSI imagery was pre-processed in a similar way as the Sentinel-3 OLCI data.

Atmospheric corrections

Several atmospheric corrections were tested for both Sentinel-2 MSI and Sentinel-3 OLCI (Table 2 and Table 3), and the validation results for these are presented here. For further detail, please see associated references provided in the tables.

Table 2 – List of Sentinel-2 atmospheric corrections tested

Sentinel-2			
Atmospheric Correction	Reference	Details	Link
ACOLITE	Vanhellemont (2019); Vanhellemont and Ruddick (2018), Vanhellemont and Ruddick (2016; 2015; 2014)	v20180925	https://odnature.naturalsciences.be/remsem/software-and-data/acolite
Case 2 Regional CoastColour (C2RCC)	Doerffer and Schiller (2008); Brockmann and Doerffer (2016)	v1.0	https://www.brockmann-consult.de/portfolio/water-quality-from-space/
Case-2 Extreme Waters (C2X)	Nechad, et al. (2017)	v1.0	http://www.brockmann-consult.de/c2x/
Image correction for atmospheric	De Keukelaere et al. (2018); Sterckx et al (2015)	v 1.0	https://eo.belspo.be/en/news/icor-atmospheric-image-correction-made-accessible

This project has received funding from the European Union's Horizon 2020 research and innovation programme under grant agreement No 776348

Sentinel-2			
Atmospheric Correction	Reference	Details	Link
effects (iCOR)			
Polymer	Steinmetz et al (2011)	v4.8	https://www.hygeos.com/polymer

Table 3 – List of Sentinel-3 atmospheric corrections tested

Sentinel-3			
Atmospheric Correction	Reference	Details	Link
Augmented Case 2 Regional CoastColour (augC2RCC)	Doerffer and Schiller (2008); Brockmann and Doerffer (2016); Same source, just with a different training set for the NN	V1.0	https://www.brockmann-consult.de/portfolio/water-quality-from-space/
Case 2 Regional CoastColour (C2RCC)	Doerffer and Schiller (2008); Brockmann and Doerffer (2016)	V1.0	https://www.brockmann-consult.de/portfolio/water-quality-from-space/
Polymer	Steinmetz et al (2011)	v4.9 (2018 data)	https://www.hygeos.com/polymer
		V4.10 (2019 data)	
WFR	ESA OLCI Level-2 Full Resolution (OL_2_WRF) Product	standard product	https://sentinel.esa.int/web/sentinel/user-guides/sentinel-3-olci/product-types/level-2-water

This project has received funding from the European Union's Horizon 2020 research and innovation programme under grant agreement No 776348

Overall AC algorithm performance

The performance of atmospheric corrections (ACs) for every region are summarized in Table 4. In general, the best performing algorithms vary by region and satellite sensor, which indicates the need for testing atmospheric correction algorithms regionally. The best performing algorithm for each dataset and region was used to produce the satellite $R_{rs}(\lambda)$ data, which were inputs for the corresponding downstream products. We note that further validation and analyses are required by acquiring *more in situ* data to evaluate and demonstrate the robustness of a chosen AC over regions and time. For further validation results, please see the following sub-sections.

Table 4 Performance of atmospheric correction algorithms over studied regions

Algorithm performance							
Country	**Regions**	**Time**	***In situ* radiometer**	**Satellite data**	**AC algorithm(s) evaluated**	**Best performing AC algorithm**	**N**
Italy	Venice Lagoon	2019	WISP-3	Sentinel-2 MSI	ACOLITE	ACOLITE	104
Spain	Ria de Vigo	2018	WISP-3	Sentinel-2 MSI	ACOLITE, C2RCC, C2X, iCor, Polymer	C2RCC, C2X	32
				Sentinel-3 OLCI	augC2RCC, C2RCC, Polymer, WFR	Polymer	32
Italy and Spain	Venice Lagoon, and Ria de Vigo	2018	TriOS RAMSES	Sentinel-2 MSI	ACOLITE, C2RCC, iCOR, Polymer, C2X	C2RCC, Polymer	42
				Sentinel-3 OLCI	C2RCC, Polymer	C2RCC	44
Netherlands	NIOZ Jetty and Eemshaven pole, Wadden Sea	2015 - 2017	TriOS RAMSES	Sentinel-2 MSI	ACOLITE, C2RCC, C2X	C2X	13
				Sentinel-3 OLCI	ACOLITE, augC2RCC, C2RCC	augC2RCC	20

This project has received funding from the European Union's Horizon 2020 research and innovation programme under grant agreement No 776348

Algorithm performance							
Country	**Regions**	**Time**	***In situ* radiometer**	**Satellite data**	**AC algorithm(s) evaluated**	**Best performing AC algorithm**	**N**
France	Bourgneuf Bay (intertidal areas)	2018 - 2019	ASD	Sentinel-2 MSI	Sen2Cor	Sen2Cor	45
	Glénan archipelago (shallow waters)	2019	TriOS RAMSES and ASD	Sentinel-2 MSI	ACOLITE, C2RCC, Polymer	Polymer	38

3.1.1.1 Validation with WISP-3

The WISP-3 handheld radiometer (Water Insight) was one instrument used to collect *in situ* radiometry for validation of satellite R_{rs}. WISP-3 radiance and irradiance spectra are processed according to the following equation to obtain subsurface irradiance reflectance ($R(0^-)$):

$$R(0\text{-}) = Q \times f\,(L_u - r_{sky} \times L_d)/E_d \qquad \text{Equation 1}$$

where Q denotes the conversion coefficient for L_{wu} (upwelling radiance below water) to E_{wu} (upwelling irradiance below water), *f* is the conversion constant of L_u (upwelling radiance above water) to L_{wu} (upwelling radiance below water), r_{sky} is the radiance of skylight at zenith angle of 420°.

R_{rs} is calculated from the WISP by Water Insight using the following equation:

$$R_{rs}(\lambda) = \frac{L_t(\lambda) - \rho_s L_s(\lambda)}{E_s(\lambda)} \qquad \text{Equation 2}$$

Where L_t is the spectral water-leaving radiance, L_s is the sky radiance, E_s is the downwelling irradiance, and ρ_s is the fraction of Ls reflected specularly on the water surface. ρ is taken as a constant (ρ= 0.028).

Italy

Sentinel-2 MSI

Intensive and expeditive fieldworks were undertaken in the Lagoon of Venice (LV) to gather data for the purpose of validating CoastObs standard products, including water reflectance and water-quality parameters (turbidity and SPM).

Starting from January 2019 to May 2019, 14 campaigns were carried out, synchronous with the passage of Landsat 8 (L8) and Sentinel-2 (S2) satellites. The measurement stations were located in the area of the Lido tidal mouth and in the central sector of the lagoon. A total of 120 stations were visited with a maximum time difference of 1 h from the satellite overpasses. Two campaigns were excluded from the validation analysis, because of atmospheric conditions (partly cloudy sky). At each station, above water remote sensing reflectances were measured with the WISP-3 spectroradiometer (Water Insight).

The list of campaigns carried out is summarized in Table 5. Figure 6 show the map and the coordinates of the stations investigated.

Table 5– Expeditive fieldworks carried out in the LV to validate CoastObs standard products

Date	Site	Number of stations	S2A	S2B	L8	Sky conditions
24/01/2019	Lido inlet	6 (ST1-ST6)	X		X	Clear Sky
05/02/2019	Lido inlet	7 (ST1-ST7)		X		Clear Sky
08/02/2019	Lido inlet	7 (ST1-ST7)		X		Clear Sky
15/02/2019	Lido inlet	7 (ST1-ST7)		X		Partly Cloudy
25/02/2019	Lido inlet	7 (ST1-ST7)		X	X	Clear Sky
28/02/2019	Lido inlet	7 (ST1-ST7)		X		Clear Sky
20/03/2019	Central sector of LV	6 (ST1-ST6)		X		Clear Sky
22/03/2019	Lido inlet	7 (ST1-ST7)	X		X	Clear Sky
29/03/2019	Lido inlet	7 (ST1-ST7)			X	Clear Sky
01/04/2019	Lido inlet	7 (ST1-ST7)	X			Clear Sky
16/04/2019	Lido inlet	8 (ST1-ST8)		X		Clear Sky
19/04/2019	Lido inlet	8 (ST1-ST8)		X		Clear Sky
24/05/2019	Lido inlet	8 (ST1-ST8)	X			Partly Cloudy
31/05/2019	Lido inlet	8 (ST1-ST8)	X			Clear Sky

This project has received funding from the European Union's Horizon 2020 research and innovation programme under grant agreement No 776348

Figure 6- Study area with location of fieldwork activities carried out from January to May 2019 (red dots: measurement stations on 20th March 2019 in the central sector of the LV; yellow dots: revisited stations at the Lido inlet).

L8 and S2 data were processed with the same methodology. Briefly, L8 imagery, obtained from USGS, and S2 data, downloaded from Copernicus Open Access Hub, were radiometrically calibrated according to Pahlevan et al. (2014) and Pahlevan et al. (2019), respectively. The vicarious calibration, reported in Pahlevan et al. (2014) and Pahlevan et al. (2019), considering the differences in their spectral and spatial sampling, is important for combining Sentinel-2 and Landsat data products and for generating consistent data for global water quality monitoring. TOA reflectances were atmospherically corrected with ACOLITE (Atmospheric Correction for OLI 'lite'), an automatic method for L8 OLI atmospheric correction in coastal and inland waters (Vanhellemont and Ruddick, 2014, 2015) and adapted to Sentinel-2 data (Vanhellemont and Ruddick, 2016). ACOLITE was run selecting the "dark spectrum fitting" approach (Vanhellemont and Ruddick, 2018; Vanhellemont, 2019). This approach uses multiple dark targets in the subscene to construct a "dark spectrum" which is used to estimate the atmospheric path reflectance (ρpath) according to the best fitting aerosol model. ACOLITE represents an unified processor publicly available for water applications of multi-sensor long-term archive and was originally developed for remote sensing of water turbidity in turbid and extremely turbid waters (Vanhellemont and Ruddick, 2016) using Landsat and Sentinel-2 type sensors. It was successfully applied in turbid environments, thus it was also selected as the AC method for the present intensive and expeditive validation activities, considering that the optical water quality was influenced mainly by suspended sediments.

This project has received funding from the European Union's Horizon 2020 research and innovation programme under grant agreement No 776348

In situ WISP-3 data were used to assess the accuracy of ACOLITE -derived R_{rs} from synchronous L8 and S2 imagery. During fieldwork activities, we performed about 10 measurements for each station in a period of 1-2 minutes. WISP-3 data were upload on WISPweb and a first data check was made before saving the measurements on the website. A total of 104 match-ups (28 with S2A, 49 with S2B and 27 with L8, 20 of those with both S2 and L8) between satellite and *in situ* data collection were available by considering a maximum time difference of 1 h. Figure 7 shows the scatter plots of the L8 and S2A and B derived R_{rs} versus *in situ* WISP-3 measurements. The correlations were statistically significant with better performances for the Green and Red bands, which have generally the highest reflectance range, and which are of general of interest to retrieve turbidity at low to moderate turbidities. For the three sensors and for all the bands, an overestimation is observable when R_{rs} is medium-low, while it is underestimated for R_{rs} higher values. See Table 6 for the complete statistics of fitting.

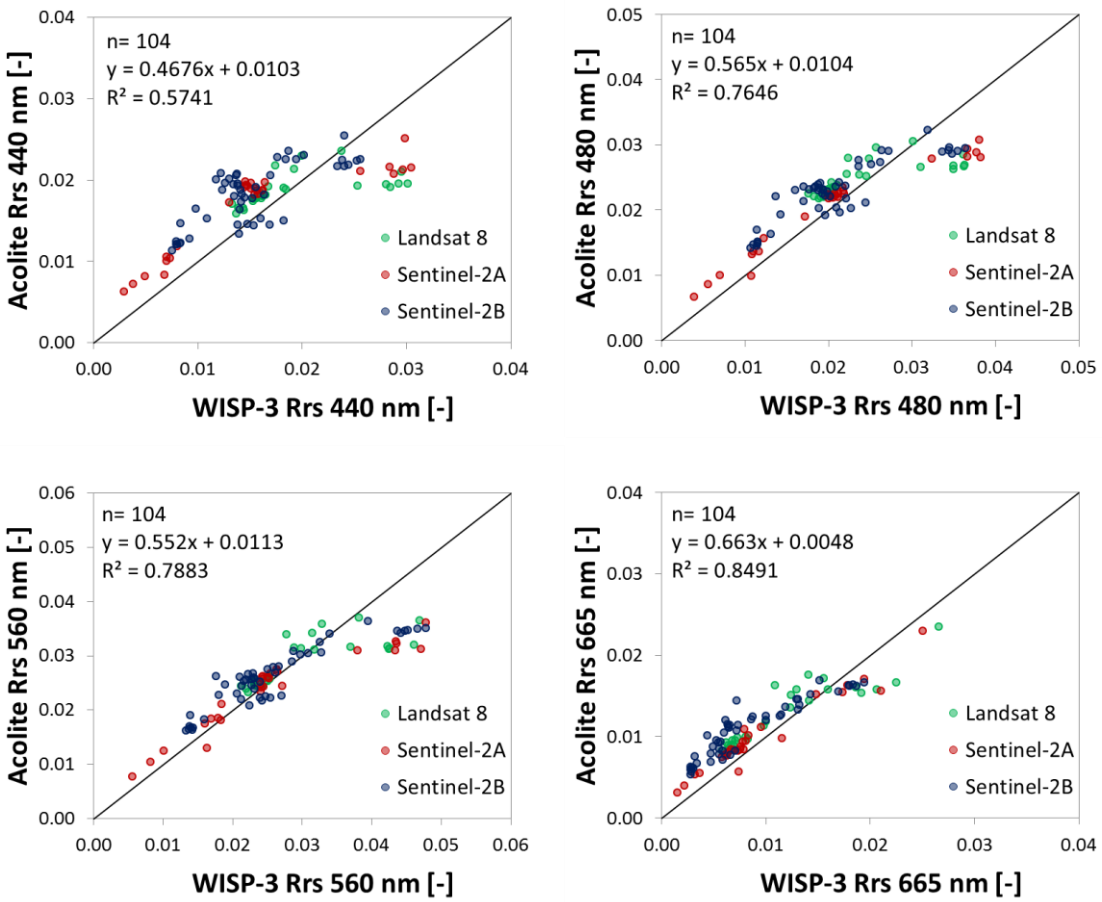

Figure 7 - Validation scatterplots for R_{rs} CoastObs product, indicating R^2 and linear regression fit.

This project has received funding from the European Union's Horizon 2020 research and innovation programme under grant agreement No 776348

Table 6 – Error metrics for R_{rs} CoastObs product

Product	R^2	slope	RMSE	Bias	MAE	N
LV/ R_{rs} 443	0.574121	0.467627	0.004527	0.001664	0.003912	104
LV/ R_{rs} 490	0.764604	0.564954	0.00431	0.000959	0.00365	104
LV/ R_{rs} 560	0.788292	0.552028	0.005198	-0.00074	0.003616	104
LV/ R_{rs} 665	0.849082	0.663042	0.002855	0.001536	0.002492	104

Spain

Valid match-ups for validating R_{rs} from Sentinel-3 images using simulated R_{rs} spectra from *in situ* WISP-3 measurements were obtained from 32 sampling stations during 6 days in July 2018, within the dedicated CoastObs campaign conducted in the Ria de Vigo (Galicia).

Sentinel-3 OLCI

Figure 8 shows the relationship between *in situ* reflectances from WISP-3 and R_{rs} derived from the four atmospheric correction (AC) methods proposed for Sentinel-3. A linear trend can be seen in all the methods, with determination coefficients (R^2) ranging from 0.48 to 0.57, as well as generalized negative deviations from the identity line indicating that they tend to underestimate the R_{rs}.

Table 7 shows the errors metrics comparing *in situ* WISP-3 and Sentinel-3 R_{rs} derived from the four AC methods. According to these results, Polymer outperformed other the AC methods, showing a better fitting (higher R^2) and a lower error (lower RMSE and MAE). The tendency to understimate observed in Figure 7 is confirmed by negative bias values in all the methods.

This project has received funding from the European Union's Horizon 2020 research and innovation programme under grant agreement No 776348

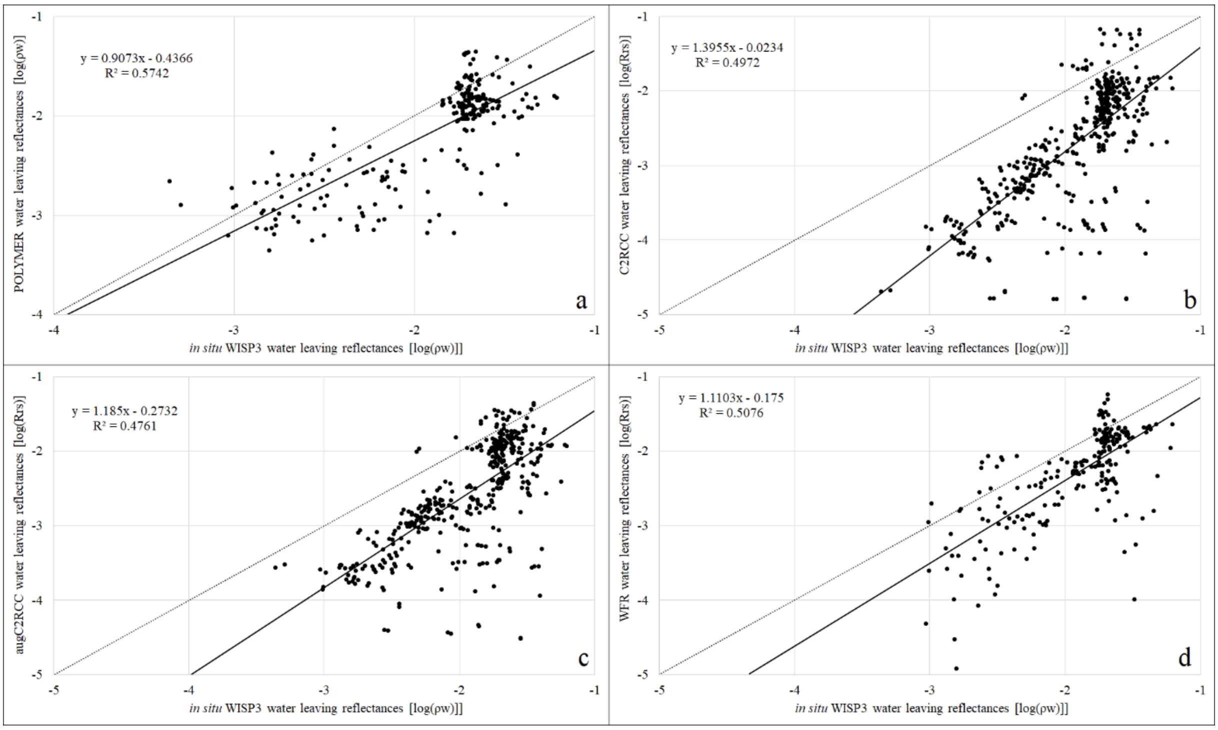

Figure 8 - Validation scatterplots between *in situ* R_{rs} from WISP-3 and R_{rs} from Sentinel-3 using: a) Polymer; b) C2RCC; c)augC2RCC; d) WFR.

Table 7 – Error metrics comparing *in situ* R_{rs} from WISP-3 and Sentinel-3 using different atmospheric correction algorithms.

AC	R^2	slope	RMSE	Bias	MAE
Polymer	0.57	0.91	0.44	-0.26	0.32
C2RCC	0.50	1.40	0.99	-0.79	0.82
augC2RCC	0.48	1.18	0.81	-0.63	0.65
WFR	0.51	1.11	0.60	-0.39	0.45

Sentinel-2 MSI

Five AC methods for Sentinel-2 were also tested using WISP-3 *in situ* measurements from 32 sampling stations during four days in July 2018 within the CoastObs campaign in the Ria de Vigo (Galicia).

This project has received funding from the European Union's Horizon 2020 research and innovation programme under grant agreement No 776348

Table 8 shows the errors metrics comparing *in situ* WISP-3 and Sentinel-2 R_{rs} derived from the five AC methods. Figure 8 shows the relationship between *in situ* reflectances from WISP-3 and R_{rs} derived from Sentinel-2 using only the four best AC methods.

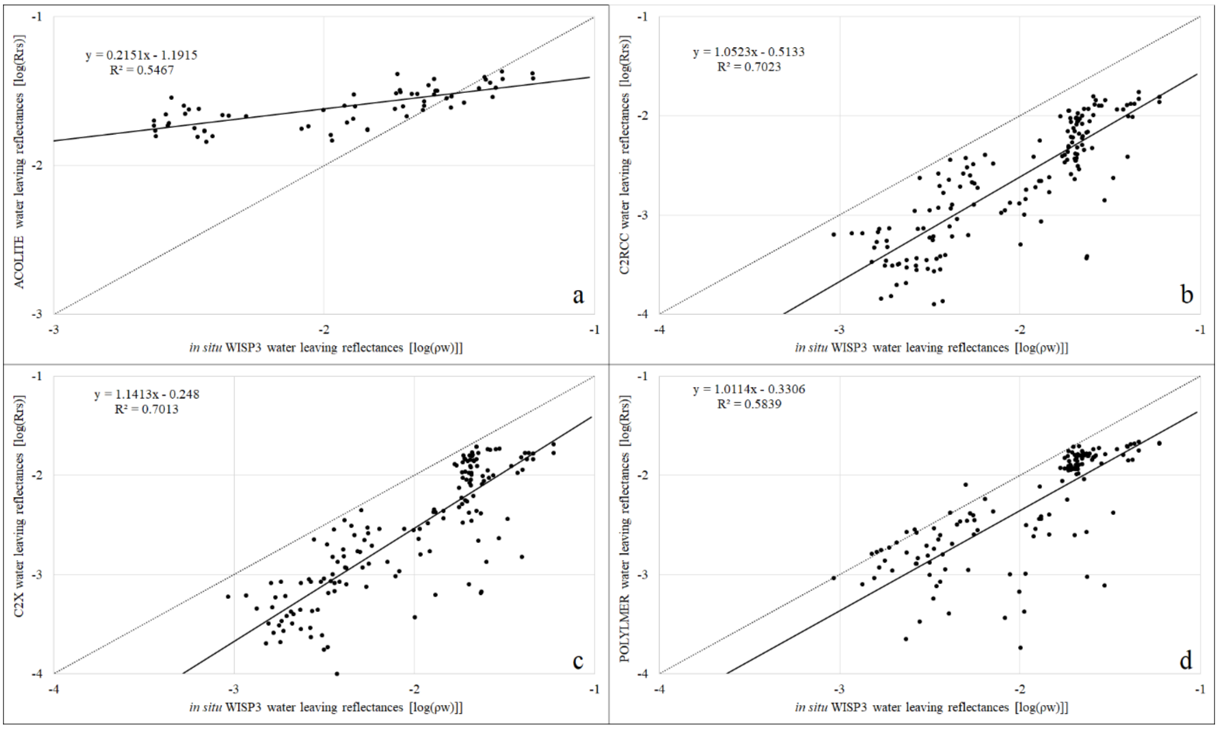

Figure 9- Validation scatterplots between *in situ* R_{rs} from WISP-3 and R_{rs} from Sentinel-3 using: a) ACOLITE; b) C2RCC; c)C2X; d) Polymer.

Table 8 - Error metrics comparing *in situ* R_{rs} from WISP-3 and Sentinel-2 using different atmospheric correction algorithms.

AC	R^2	slope	RMSE	Bias	MAE
ACOLITE	0.55	0.22	0.48	0.33	0.36
C2RCC	0.70	1.05	0.70	-0.62	0.62
C2X	0.70	1.14	0.64	-0.54	0.54
Polymer	0.58	1.01	0.52	-0.35	0.36
iCOR	0.01	-0.06	0.91	0.69	0.76

Results from iCOR are remarkably poorer than the other AC methods, which show linear fittings with positive correlations (R^2 ranging from 0.55 to 0.70). While ACOLITE tends to overestimate

This project has received funding from the European Union's Horizon 2020 research and innovation programme under grant agreement No 776348

with low R_{rs} values (bias = 0.33), the other three models in Figure 9 show negative deviations with respect to the identity line and negative bias values.

Although C2RCC and C2X outperform Polymer in terms of correlation (higher R^2 values), these methods show also higher error values (higher RMSE and MAE) and higher deviations from the identity line (slopes far from one, lower bias values). As a consequence, further analysis would be required by adding the 2019 dataset to make a decision about the best performing AC method for Sentinel-2.

3.1.1.2 Validation with TriOS RAMSES

In situ reflectance was measured also measured during the Venice and Vigo 2018-2019 campaigns using a set of TriOS RAMSES hyperspectral radiometers. For the TriOS data, R_{rs} was processed from the measured irradiance and radiance spectra according to the following equation:

$$R_{rs}(\lambda) = \frac{L_t(\lambda) - \rho_s L_s(\lambda)}{E_s(\lambda)} - \varepsilon \qquad \text{Equation 3}$$

Where L_t is the spectral water-leaving radiance, L_s is the sky radiance, E_s is the downwelling irradiance, and ρ_s is the fraction of Ls reflected specularly on the water surface. ρ_s is obtained using the procedure in Simis and Olsson (2013), a spectral optimisation procedure to minimise the presence of features in R_{rs} associated with atmospheric absorption.

Spectra resulting from this procedure may have a spectrally neutral offset, ε (Qin et al. 2017). The offset is calculated using the near infrared reflectance where the absorption by pure water is assumed to dominate the shape of R_{rs}. ε is calculated from the ratio of bands at 779 and 865 nm as:

$$\varepsilon = \frac{(R_{rs}(865)\, a_w(865)) - R_{rs}(779)}{a_w(865) - a_w(779)} \qquad \text{Equation 4}$$

where $a_w(\lambda)$ is the absorption by pure water, as in Roettgers et al. (2011).

Italy and Spain

For the 2018 Venice and Vigo campaigns, reflectance data were collected *in situ* using the TriOS RAMSES radiometers. The results of these are presented for the two datasets together, for both Sentinel-2 and -3 reflectances.

Sentinel-2 MSI

The scatterplots at each Sentinel-2 band for the four atmospheric corrections (ACs) tested are shown in Figure 10 to Figure 13. The best performing ACs for Sentinel-2 were Polymer and

C2RCC, and the validation error metrics for R_{rs} are presented in Figure 14 - Validation scatterplots for Sentinel-2 MSI iCOR atmospheric correction, indicating R2 and linear regression fit at each band (B4-B8A not shown due to zero values for all iCOR Rrs at these bands)

Table 9 and Table 10, respectively. These two ACs both outperformed iCOR, C2X and ACOLITE. C2RCC had higher errors than Polymer for the NIR bands (B6-B8A), however C2RCC outperformed Polymer in the Blue to NIR bands (B1-B5).

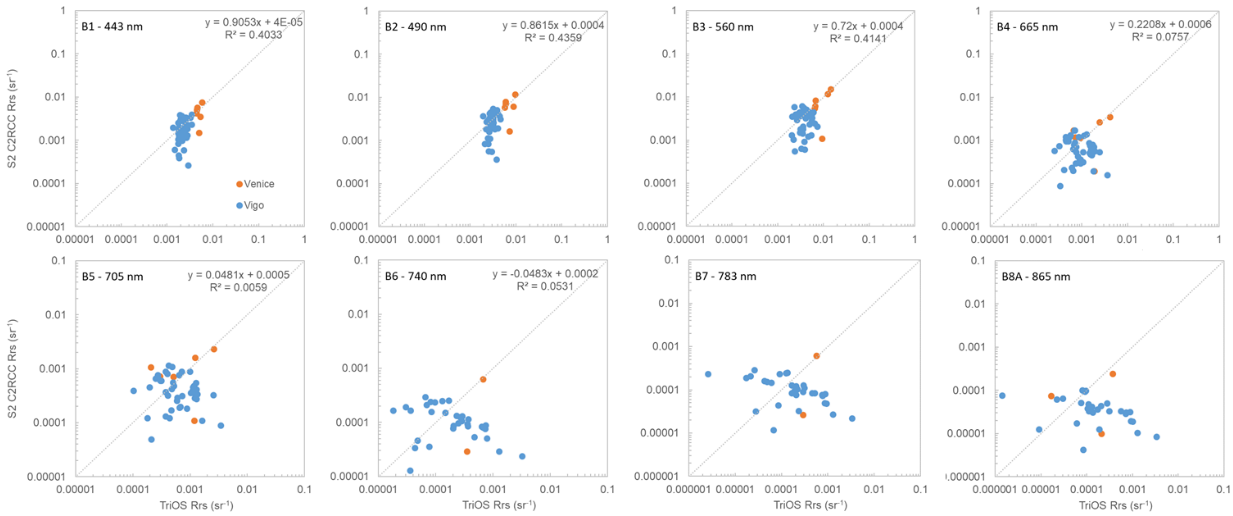

Figure 10 - Validation scatterplots for Sentinel-2 MSI C2RCC atmospheric correction, indicating R^2 and linear regression fit at each band

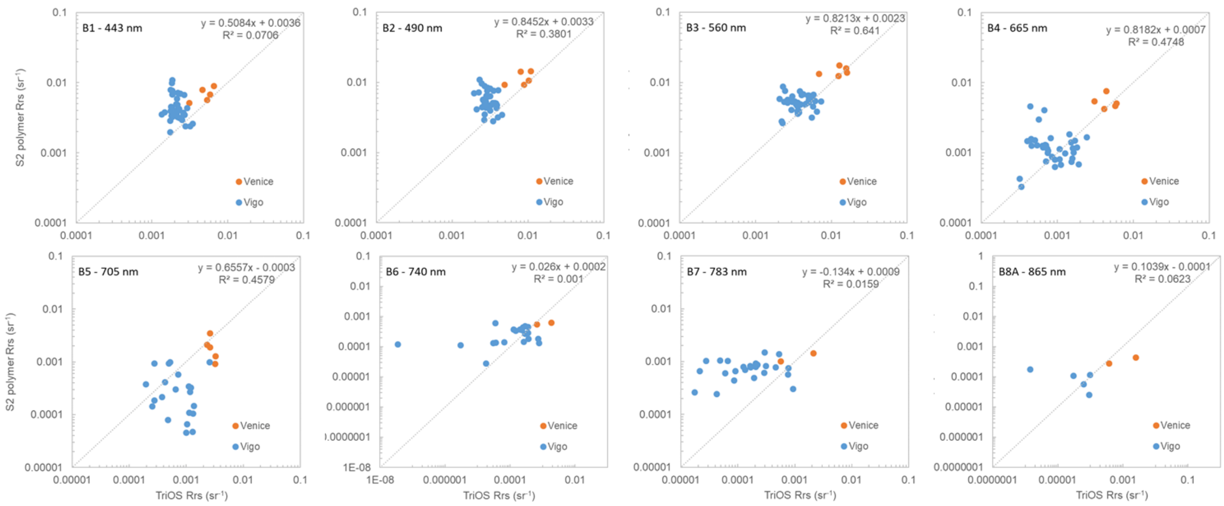

This project has received funding from the European Union's Horizon 2020 research and innovation programme under grant agreement No 776348

Figure 11 - Validation scatterplots for Sentinel-2 MSI Polymer atmospheric correction (v4.9), indicating R² and linear regression fit at each band

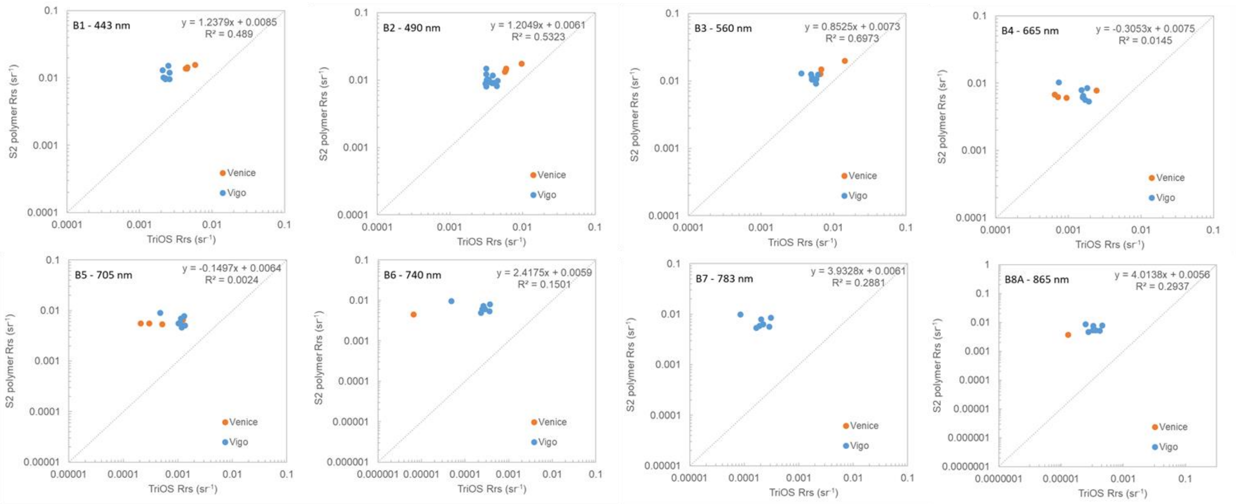

Figure 12 - Validation scatterplots for Sentinel-2 MSI ACOLITE atmospheric correction, indicating R² and linear regression fit at each band

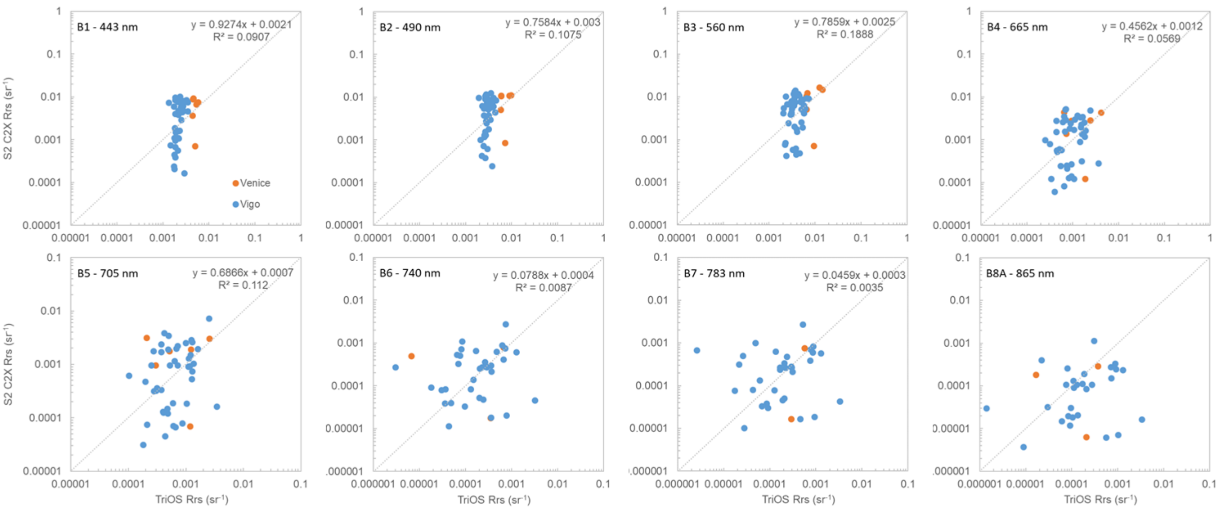

Figure 13 - Validation scatterplots for Sentinel-2 MSI C2X atmospheric correction, indicating R² and linear regression fit at each band

This project has received funding from the European Union's Horizon 2020 research and innovation programme under grant agreement No 776348

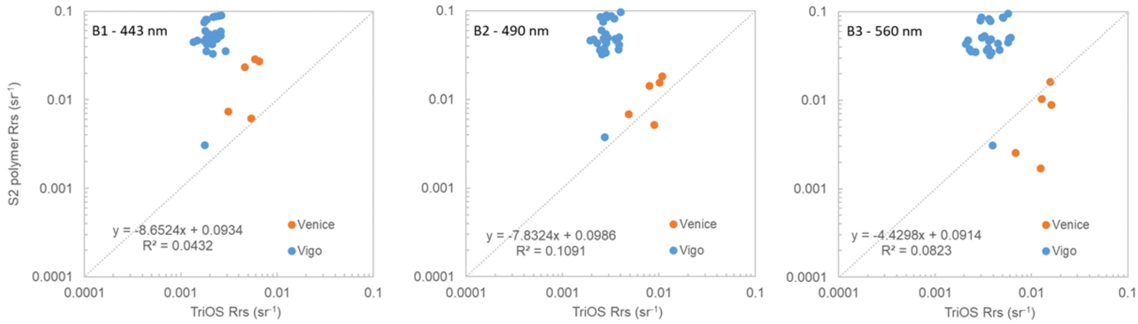

Figure 14 - Validation scatterplots for Sentinel-2 MSI iCOR atmospheric correction, indicating R^2 and linear regression fit at each band (B4-B8A not shown due to zero values for all iCOR R_{rs} at these bands)

Table 9 – Error metrics for Sentinel-2 MSI Polymer atmospheric correction at each band, for the combined Venice and Vigo 2018 datasets (n=42)

S2 Band	Band Centre (nm)	R^2	slope	$RMSE_{log}$	$Bias_{log}$	MAE_{log}	MAPE (%)
B1	443	0.0706	0.508	0.351	0.284	0.298	119%
B2	490	0.380	0.845	0.309	0.250	0.264	97.4%
B3	560	0.641	0.821	0.214	0.125	0.161	52.0%
B4	665	0.475	0.818	0.341	0.132	0.257	106%
B5	705	0.458	0.656	0.781	-0.475	0.587	110%
B6	740	0.001	0.0260	0.941	0.341	0.573	9318%
B7	783	0.0159	-0.134	0.925	0.698	0.753	2616%
B8A	865	0.0623	0.104	0.899	0.186	0.603	641%

This project has received funding from the European Union's Horizon 2020 research and innovation programme under grant agreement No 776348

Table 10 – Error metrics for Sentinel-2 MSI C2RCC atmospheric correction at each band, for the combined Venice and Vigo 2018 datasets (n=49)

S2 Band	Band Centre (nm)	R^2	slope	$RMSE_{log}$	$Bias_{log}$	MAE_{log}	MAPE (%)
B1	443	0.403	0.905	0.283	-0.0990	0.206	37.7%
B2	490	0.436	0.862	0.280	-0.0755	0.193	35.5%
B3	560	0.414	0.720	0.334	-0.146	0.253	44.3%
B4	665	0.0757	0.221	0.446	-0.158	0.369	71.1%
B5	705	0.00590	0.0481	0.521	-0.186	0.426	84.3%
B6	740	0.0531	-0.0483	0.995	-0.0999	0.732	7858%
B7	783	0.0743	-0.0524	0.886	-0.275	0.721	642%
B8A	865	0.0907	-0.0226	1.09	-0.650	0.874	279%

Sentinel-3A OLCI

The best performing atmospheric correction for Sentinel-3A was C2RCC, with low errors and high R^2 values where compared with TriOS *in situ* data (Figure 15). Polymer v4.9 also performed adequately, but with greater scatter and higher errors the C2RCC (Figure 16). As with Sentinel-2 data corrected with Polymer, there are also frequently negative R_{rs} values in the Red and NIR bands (e.g. Oa 11). This is particularly an issue when using Polymer corrected data for deriving Chl-*a* concentrations, which often use a ratio of reflectance in the NIR to Red bands. Furthermore, none of the Polymer corrected R_{rs} values were significantly correlated with the *in situ* R_{rs} at any band (R^2<0.121).

This project has received funding from the European Union's Horizon 2020 research and innovation programme under grant agreement No 776348

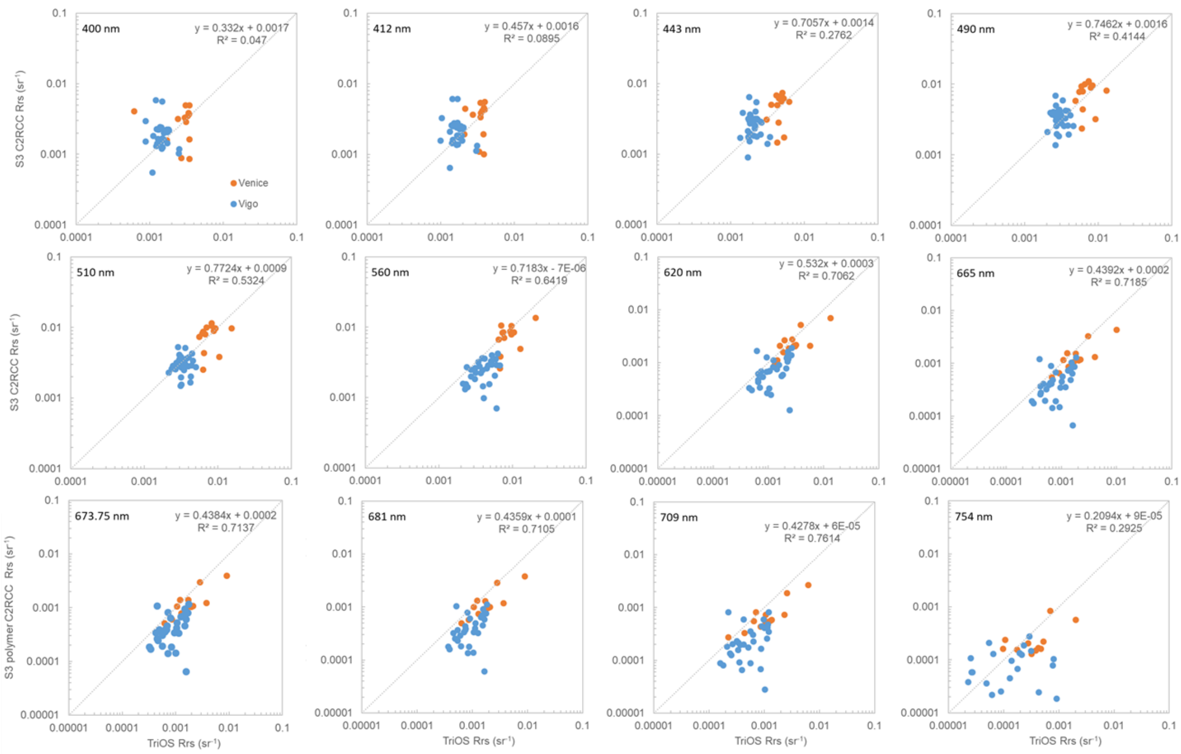

Figure 15 - Validation scatterplots for Sentinel-3 OLCI C2RCC atmospheric correction, indicating R^2 and linear regression fit at each band (Bands Oa1-Oa12)

This project has received funding from the European Union's Horizon 2020 research and innovation programme under grant agreement No 776348

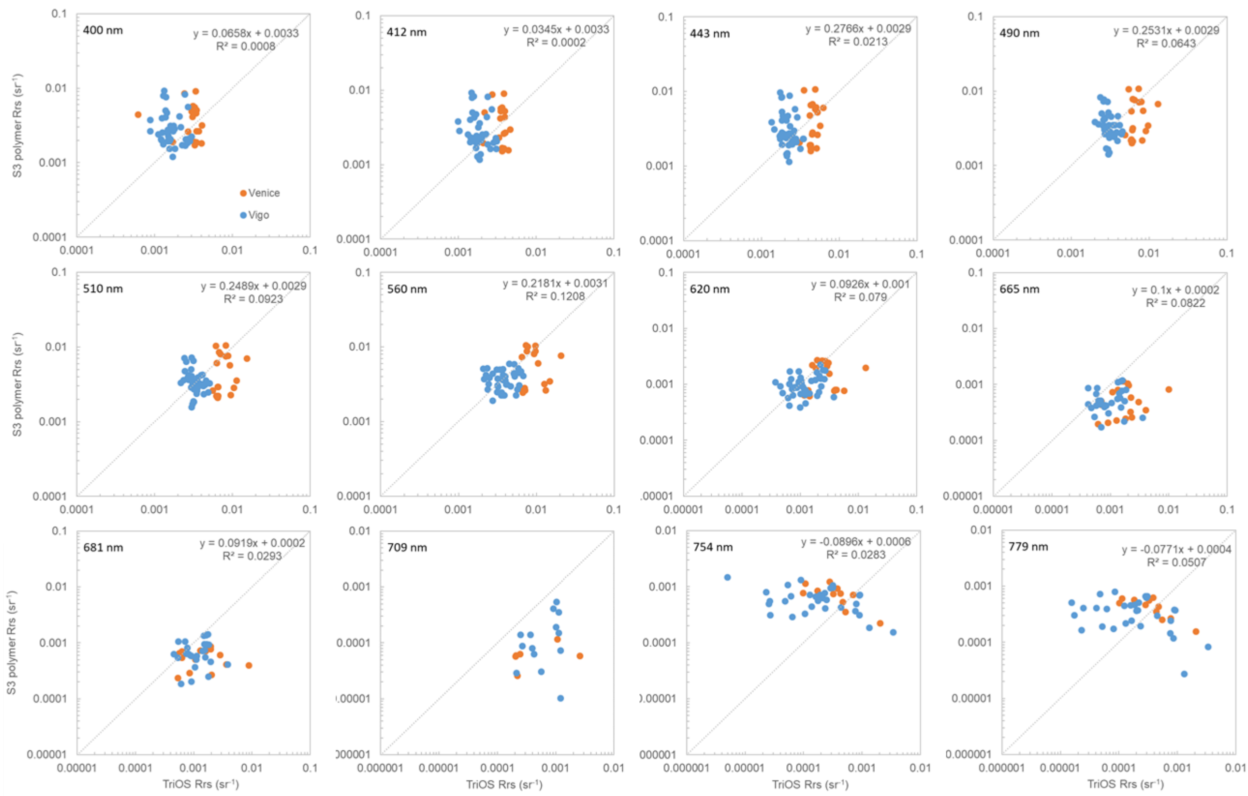

Figure 16 - Validation scatterplots for Sentinel-3 OLCI Polymer v4.9 atmospheric correction, indicating R^2 and linear regression fit at each band (Bands Oa1-Oa16)

Table 11 – Error metrics for Sentinel-3A OLCI C2RCC atmospheric correction for bands Oa1-Oa12, for the combined Venice and Vigo 2018 datasets (n=44)

S3A Band	Band Centre (nm)	R^2	slope	$RMSE_{log}$	$Bias_{log}$	MAE_{log}	MAPE (%)
Oa1	400	0.047	0.332	0.280	0.0784	0.201	65.8%
Oa2	412.5	0.0895	0.457	0.250	0.0589	0.186	52.5%
Oa3	442.5	0.276	0.706	0.226	0.0692	0.182	49.7%
Oa4	490	0.414	0.746	0.192	0.0355	0.161	40.0%
Oa5	510	0.532	0.772	0.175	-0.0367	0.135	28.0%
Oa6	560	0.642	0.718	0.272	-0.187	0.206	33.9%
Oa7	620	0.706	0.532	0.328	-0.203	0.247	41.6%

This project has received funding from the European Union's Horizon 2020 research and innovation programme under grant agreement No 776348

S3A Band	Band Centre (nm)	R^2	slope	$RMSE_{log}$	$Bias_{log}$	MAE_{log}	MAPE (%)
Oa8	665	0.718	0.439	0.372	-0.250	0.285	45.7%
Oa9	673.75	0.714	0.438	0.389	-0.281	0.305	46.7%
Oa10	681.25	0.711	0.436	0.425	-0.329	0.404	56.9%
Oa11	708.75	0.761	0.428	0.466	-0.330	0.370	55.5%
Oa12	753.75	0.293	0.209	0.605	-0.224	0.467	260%

Table 12 – Error metrics for Sentinel-3A OLCI Polymer atmospheric correction for bands Oa1-Oa12, for the combined Venice and Vigo 2018 datasets (n=60)

S3A Band	Band Centre (nm)	R^2	slope	$RMSE_{log}$	$Bias_{log}$	MAE_{log}	MAPE (%)
Oa1	400	0.0008	0.0658	0.342	0.179	0.275	110%
Oa2	412.5	0.0002	0.0345	0.313	0.109	0.254	88.5%
Oa3	442.5	0.0213	0.277	0.289	0.0650	0.231	73.4%
Oa4	490	0.0643	0.253	0.258	-0.0443	0.207	48.6%
Oa5	510	0.0923	0.249	0.256	-0.7323	0.202	43.3%
Oa6	560	0.121	0.218	0.260	-0.0969	0.201	39.4%
Oa7	620	0.0790	0.0926	0.330	-0.154	0.250	45.0%
Oa8	665	0.0822	0.100	0.500	-0.373	0.399	82.0%
Oa10	681.25	0.0293	0.0919	0.449	-0.300	0.336	84.7%
Oa11	708.75	3 E-09	-4 E-05	0.915	-0.796	0.796	259%
Oa12	753.75	0.0283	-0.0896	0.837	0.465	0.678	1835%
Oa16	778.78	0.0507	-0.0771	0.735	0.189	0.597	1132%

This project has received funding from the European Union's Horizon 2020 research and innovation programme under grant agreement No 776348

Netherlands

The *in situ* dataset we used to compare and assess the quality of the atmospheric correction consists of automated TriOS measurements of water, at the NIOZ jetty station on Texel (NJS) for the years 2015 to 2017 was kindly provided by NIOZ. The location of the jetty is Lat 53.001707 and Lon 4.789045. The *in situ* measurements come from a Trios radiometer measuring reflectance on the water surface every 10 minutes. The time span for matchup used for both low and medium resolution is 120 minutes. The processing methods for these data can be found at the COLOURS documentation pages (accessed 18 September 2017). The data were used as provided without further processing. The TRIOS set-up at NIOZ consists of two sets of sensors, looking respectively to the SW and SE.

We tested the following tools/approaches for atmospheric correction over the Netherlands coastal waters:

1. ACOLITE (van Hellemont and Ruddick, 2014)
2. C2X (http://www.brockmann-consult.de/c2x/index.php/home/)
3. C2RCC (Brockmann et al., 2016)
4. Polymer (Steinmetz et al., 2011)

Sentinel-3 OLCI

The satellite values were extracted from a pixel location close to the sensor but in open water to prevent mixed pixels (land and water in the same pixel) were used (see Figure 17). The *in situ* data for cloud free pixels were used with standard processing.

For S3 we were able to collect 20 Match-up images over 2017. These were processed with the CoastColour neural network AC: C2RCC, which was trained using global coastal observations. For S3 it became clear that the net should be retrained to take into account some calibration deviations of the satellite sensor itself: this version is known as the alternative version of the C2RCC. Our statistical analyses were done using rather simple indicators because of the low number of match-up data. Both the neural networks show rather high R^2 values and slopes close to 1 which is very encouraging. The alternative version performs better in the blue spectral range. The differences in the green, red and NIR range are negligible.

This project has received funding from the European Union's Horizon 2020 research and innovation programme under grant agreement No 776348

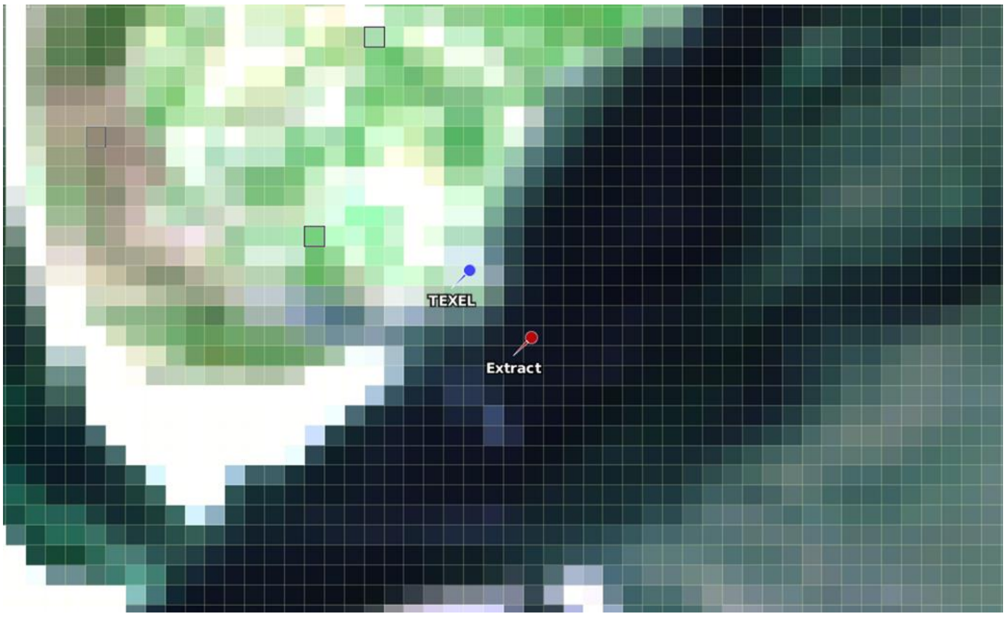

Figure 17 - Location of the pixel extraction location relative to the actual measurement station

The results from three atmospheric correction (AC) methods, namely Polymer, C2RCC and alternative C2RCC (augC2RCC) were validated with radiometric field data matching satellite observations. These AC methods were applied to Sentinel-3-OLCI (S3) images over the Ems Dollard estuary and compared to matching field-spectra. Figure 18 and Table 13 show the validation results of these methods, Polymer validation results were excluded as it yielded a large MAPE error.

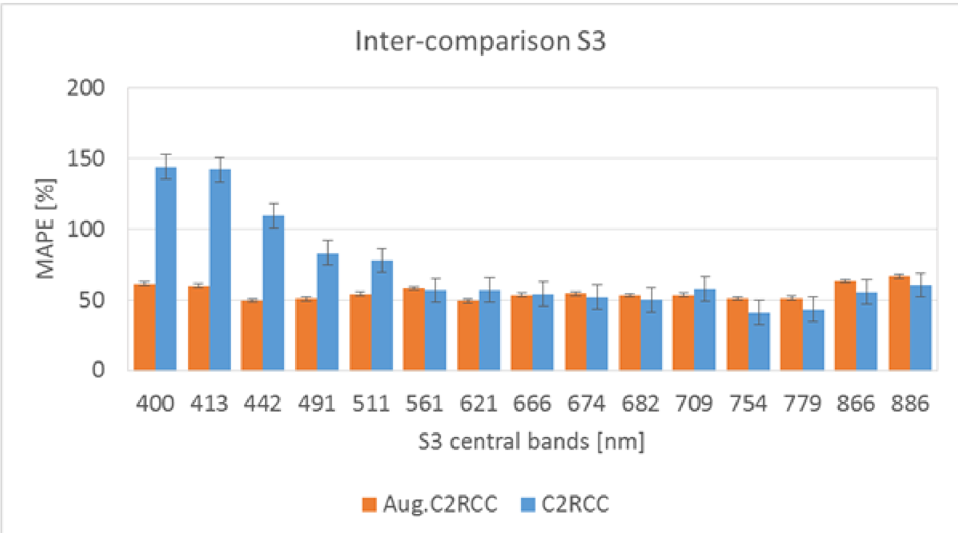

Figure 18 - Validation results, expressed in MAPE (Mean Absolute Percentage Error) values, of atmospheric correction for Sentinel-3

This project has received funding from the European Union's Horizon 2020 research and innovation programme under grant agreement No 776348

Table 13 - Validation measures for the mean spectra for S3.

	C2RCC	Aug. C2RCC
Slope	1.2	1.05
Intercept [sr^{-1}]	-8E-3	-6E-3
R^2	0.86	0.92
MAPE [%]	38.22	29.54

Sentinel-2 MSI

As above (S3 Matchup generation), the NIOZ jetty *in situ* spectral data were used, matching Sentinel-2 images that were cloud free near the location of the *in situ* station. However, Sentinel-2 has a higher spatial resolution (10-60 meters, depending on the spectral band) which let us extract the reflectance values closer to the actual station without risking a mixed pixel. For 2017, 16 cloud free dates were available for matchup.

In total there were 13 matchups between S2 MSI observations and NIOZ Jetty *in situ* measurements: 7 for ACOLITE, 9 for C2X and 10 for C2RCC.

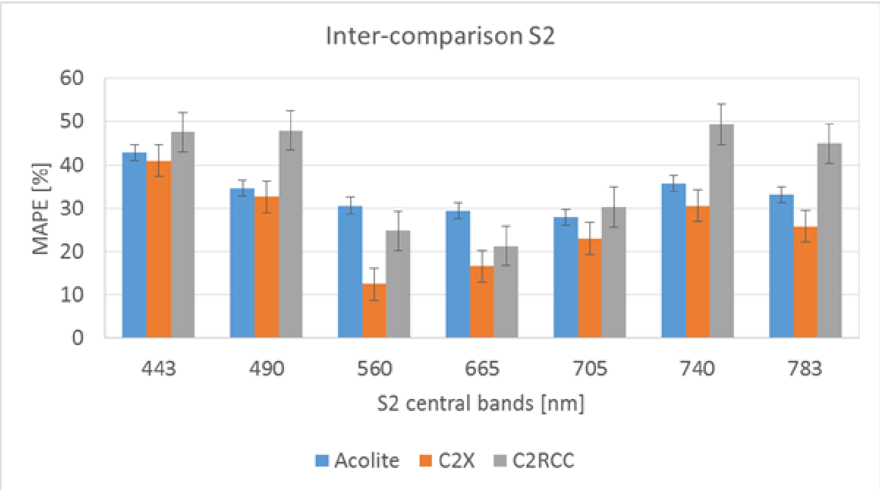

Figure 19 - Validation results, expressed in MAPE values, of atmospheric correction for Sentinel-2

Figure 20 - Validation measures for the mean spectra for S2.

	ACOLITE	C2X	C2RCC
Slope	0.54	0.9	0.69
Intercept [sr^{-1}]	6E-06	-2E-3	-2E-3
R^2	0.99	0.98	0.98
MAPE [%]	33.45	26.00	38.02

This project has received funding from the European Union's Horizon 2020 research and innovation programme under grant agreement No 776348

ACOLITE processor results

The atmospherically corrected spectra from ACOLITE are averaged per band and plotted against the averaged *in situ* spectra in Figure 21.

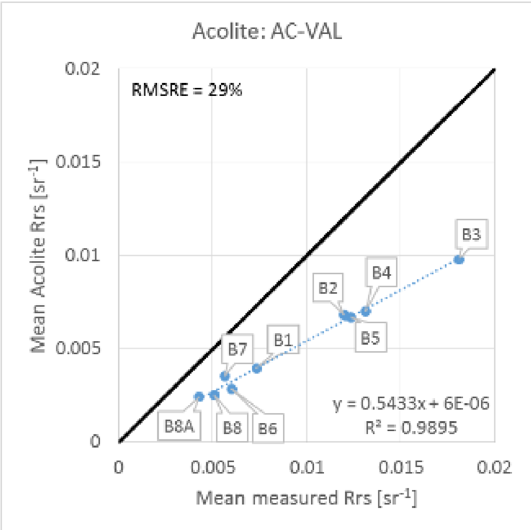

Figure 21 - ACOLITE: Validation result of mean spectra

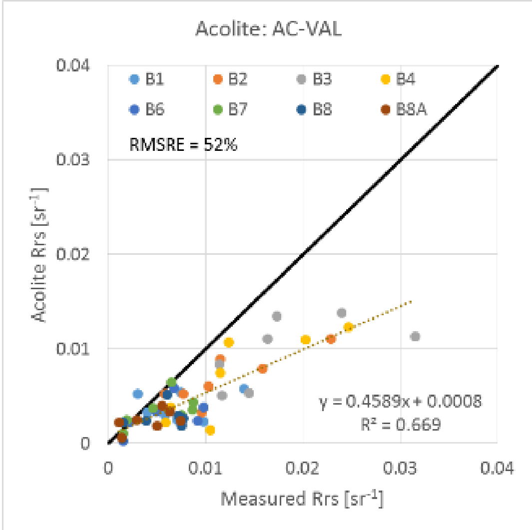

Figure 22 - ACOLITE: Validation result of actual spectra.

ACOLITE spectra are underestimated (overcorrected), in particular for 490-705 nm bands. Bands of longer wavelength and the blue band at 443 have less overcorrection. The underestimation of ACOLITE is about 54% (the slope). The RMSRE is 29% for all bands. This RMSRE is for the mean values, the RMSRE for actual values is higher ~52%. Figure 22 shows the validation per band (coloured symbol).

C2X processor results

The validation results of C2X for the mean and actual values are shown in Figure 23 and Figure 24 respectively. C2X results are much better than ACOLITE, for the mean values however. C2X slightly overcorrect (about 10%) the S2MSI spectra, with RMSRE of 26% (Figure 23).

Figure 24 shows the validation with respect to actual spectra. The RMSRE is now 55% (compare to the 26% in Figure 23) with data points closer to the 1:1 line.

This project has received funding from the European Union's Horizon 2020 research and innovation programme under grant agreement No 776348

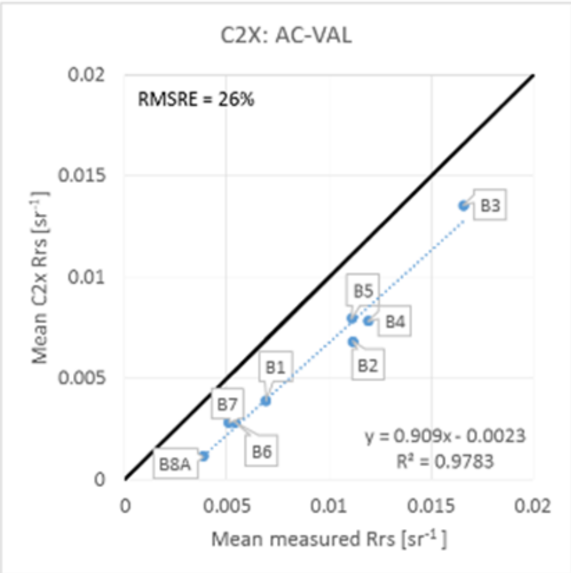

Figure 23 - C2X: Validation result of mean spectra.

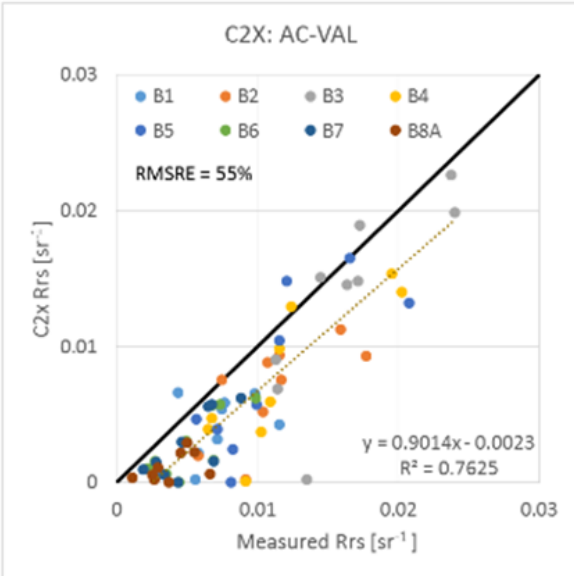

Figure 24 - C2X: Validation result of actual spectra.

C2RCC processor results

The validation results of the C2RCC processor for the mean and actual spectra are shown in Figure 25. The figure show that C2RCC performs worse than the C2X for the mean values and for the actual spectra. RMSRE 66% for C2RCC actual spectra whereas C2X has 55% RMSRE.

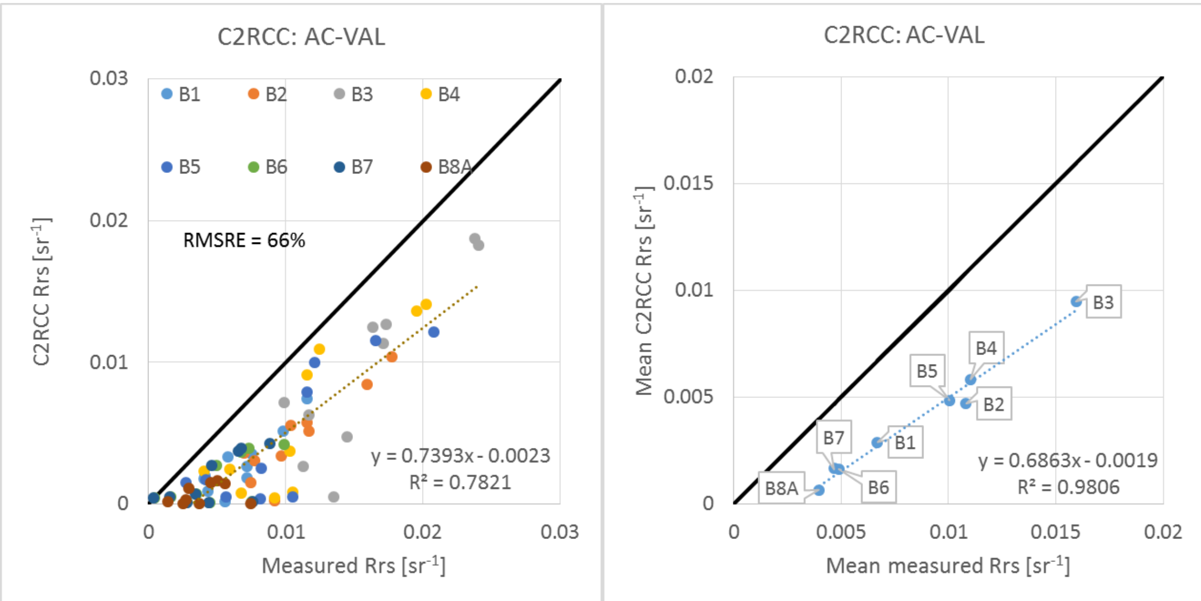

Figure 25 - C2RCC: Validation result of actual spectra (left) and mean spectra (right)

This project has received funding from the European Union's Horizon 2020 research and innovation programme under grant agreement No 776348

Comparison of methods

The mean values of the resulting spectra are plotted in Figure XX08. It is clear from Figure 26 that only C2X falls within the variability range of the *in situ* measurements. In addition, the C2X mean spectrum has an apparent absorption feature at B4 = 665 nm.

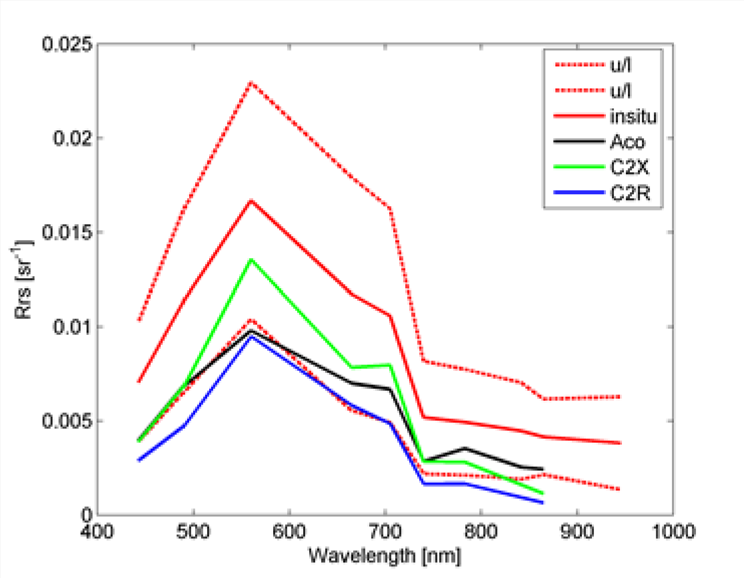

Figure 26 - Mean values of the resulting spectra. The dashed lines (u/l) are the upper and lower bounds of *in situ* spectra. Aco stands for ACOLITE.

Table 14 summarizes the statistical measure of the mean spectra. Table 15 shows the same measures used in Table 14 but for the actual values. Table 14, Table 15 and Figure 26 show that the best results were obtained from C2X.

Table 14 - Validation measures for the mean spectra.

	ACOLITE	C2X	C2RCC
Slope	0.54	0.9	0.69
Intercept [sr^{-1}]	6E-06	-0.0023	-0.0019
R^2	0.99	0.98	0.98
RMSE [%]	29	26	31

Table 15 - Validation measures of actual spectra.

	ACOLITE	C2X	C2RCC
Slope	0.46	0.90	0.74
Intercept [sr^{-1}]	0.0008	-0.0023	-0.0023
R^2	0.67	0.76	0.78
RMSE [%]	52	55	66

This project has received funding from the European Union's Horizon 2020 research and innovation programme under grant agreement No 776348

Summary of the results of the atmospheric correction of S2 MSI over water

For the atmospheric correction of S2 there are several processors available. We tested C2RCC, C2X and ACOLITE. The tests were performed using the NIOZ Jetty TRIOS spectra for validation. Since S2 has a lower overpass frequency than S3, the number of match-ups is limited. (7-10 matchups depending on the internal data flagging criteria in the processors). This number is rather low to perform a good validation but the differences were quite systematic.

Validation was performed on the mean of all available spectra and on the single observations. For the means C2X performs really well with R^2 and slope close to 1. For single observations the spread is larger but still the R^2 is around 0.8 for C2X with a slope around 0.9.

C2X was specifically trained on extreme case 2 waters as present in the Wadden Zee. This became evident from the validation results. ACOLITE severely underestimates the BOA spectrum. So C2X was selected for further processing. For validation of BOA reflectances, significantly more *in situ* measurements of reflectances are required, especially to demonstrate the robustness of a chosen AC over time and to evaluate possible improvements when the processors evolve. Such spectral data is also necessary to evaluate algorithms for water quality parameters calculations.

3.1.1.3 Validation with ASD - Intertidal Areas

France

Sentinel-2 MSI

Field radiometric validation measurements were performed on the 26 Sep 2018 and 01 Sep 2019 in Bourgneuf Bay's intertidal seagrass meadow, during concomitant Sentinel2 overpass and under clear sky. For these two dates, the matching Sentinel-2 data were downloaded from the European Space Agency (ESA) data portal (https://scihub.copernicus.eu). The performance of the ESA standard atmospheric correction (Sen2Cor processor algorithm, Main-Knorn et al., 2017) was evaluated using *in situ* reflectance measurements over three types of targets: bare sediment, dense seagrass cover, and mixed patch of various substrates (including different cover types such as bare sediment, seagrass and macroalgae). We followed different strategies to obtain the best possible matchups over those targets. For the validation over bare sediment, given the spatial homogeneity of the area, only one pixel coinciding with the geolocation of the field measurement was extracted from the S2 images. For the validation over dense seagrass cover, the average of *in situ* samples taken over cores with 100% of seagrass cover was compared against the average of several pixels identified in the field as homogeneously and fully covered by seagrass. The validation over the mixed area was performed in 2018 only: 3 pixels coinciding with the coordinates of 20 *in situ* samples were extracted and their average reflectance was calculated.

This project has received funding from the European Union's Horizon 2020 research and innovation programme under grant agreement No 776348

Considering all bands together (443-865 nm), a good performance was observed with squared correlation coefficient (R^2) of 0.97 and 0.98 in 2018 and 2019, respectively (Figure 27 and Table 16). The performance of the ESA's standard atmospheric correction was considered satisfactory for the study of intertidal seagrass meadows observed during low tide. The differences between *in situ* and satellite measurements may be due to differences between the instantaneous field-of view of the satellite (IFOV) and the area measured by the field radiometer, to the small-scale spatial variability within a pixel, to some variables inherent to field acquisition (e.g., time lapse between measurements of the target and the white reference), and/or to atmospheric correction uncertainties. The difference between the 2018 and 2019 matchups suggest that the atmospheric concentration of aerosols was higher on the 01 Sep 2019 than on the 26 Sep 2018, and that the reflectance retrieval in 2019 was subsequently underestimated.

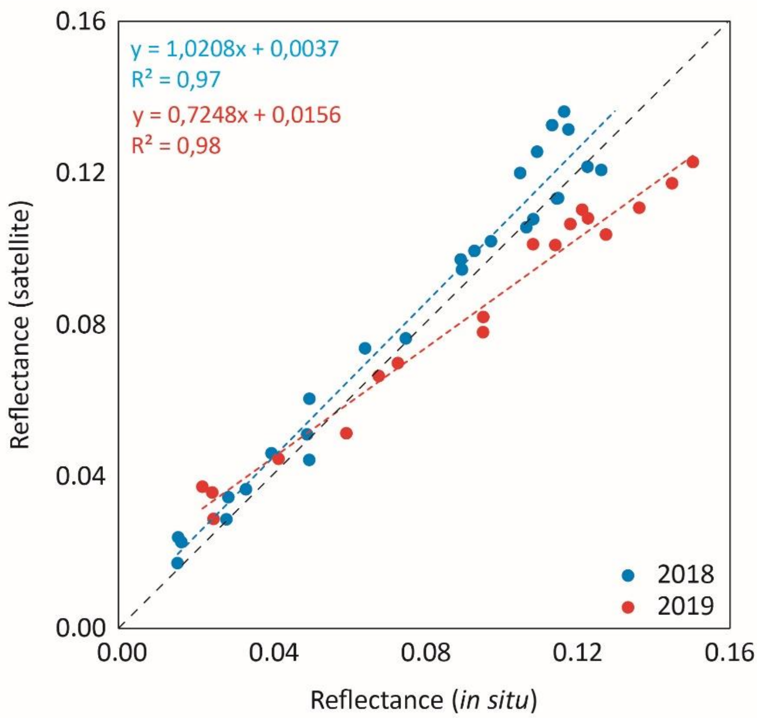

Figure 27 - Validation scatterplot for Reflectance in intertidal areas in Bourgneuf bay during 2018 and 2019, indicating R^2 and linear regression fit

This project has received funding from the European Union's Horizon 2020 research and innovation programme under grant agreement No 776348

Table 16 - Error metrics for Reflectance CoastObs product in Bourgneuf Bay over intertidal areas

Product	R^2	slope	RMSE_log	Bias_log	MAE_log	N
Bourgneuf Bay / 2018	0.97	1.02	0.063	0.038	0.045	27
Bourgneuf Bay / 2019	0.98	0.72	0.092	-0.019	0.073	18

3.1.1.4 Validation with TriOS RAMSES and ASD - Shallow Waters

France

Sentinel-2 MSI

Field radiometric validation measurements were performed on the 9 and 11 July 2019 in the shallow waters of the Glénan archipelago, during two Sentinel-2 overpasses and under clear sky. *In situ* radiometric measurements passed through processing routines to remove sky and sunglint contribution to the above-surface R_{rs}. Hyperspectral *in situ* samples were resampled to the Sentinel-2 bands using the spectral response function of Sentinel-2A. For these dates, the matching Sentinel-2 data were downloaded from the European Space Agency (ESA) data portal (https://scihub.copernicus.eu) as L1C of processing. As the atmospheric correction of Sentinel2 data in shallow waters is very challenging, the performance of the ESA standard correction was compared with three alternative corrections: Polymer (Steinmetz et al., 2011), the Case 2 Regional Coast Colour for Complex waters (C2RCC, Brockmann et al., 2016), and ACOLITE (Vanhellemont and Ruddick, 2018 and Vanhellemont, 2019). *In situ* measurements were performed over variety of bottom types (seagrass, bare sand, brown and red macroalgae, and complex mixtures of the above-mentioned bottom types) in spatially homogeneous areas and within ±1hour respect to Sentinel-2 acquisition to avoid differences in tide level. Among the three atmospheric correction routines tested, Polymer outputs showed the best results and are presented here. Atmospheric correction showed the best performance in the bands in the blue and green, where the remote sensing signal is higher (Figure 28 and Table 17). On the contrary, bands in the red and NIR showed the highest errors. In these bands, light absorption by water molecules is high and the signal to noise ratio (SNR) tends to decrease, which can be associated to higher uncertainties at these wavelengths. Also, aerosol scattering is higher in the red and NIR regions and the atmosphere results more challenging to correct.

This project has received funding from the European Union's Horizon 2020 research and innovation programme under grant agreement No 776348

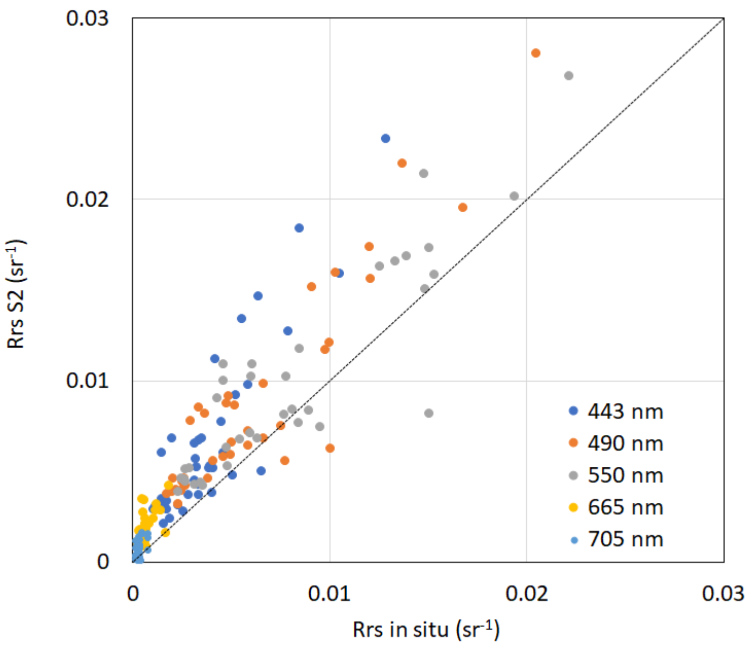

Figure 28 - Validation scatterplot for R_{rs} over shallow waters in the Glenan Archipelago during 2019, including bands 1 to 5 (443- 705 nm)

Table 17 - Error metrics for R_{rs} CoastObs product in the Glenan Archipelago over shallow waters, computed independently for bands 1 to 5 (443 to 705 nm)

Product	R^2	slope	RMSE_log	Bias_log	MAE_log	N
Band 1	0.79	1.67	0.27	0.21	0.23	38
Band 2	0.85	1.20	0.21	0.16	0.18	38
Band 3	0.82	0.97	0.18	0.12	0.14	38
Band 4	0.36	1.34	0.47	0.43	0.43	38
Band 5	0.19	1.22	0.45	0.31	0.38	38

This project has received funding from the European Union's Horizon 2020 research and innovation programme under grant agreement No 776348

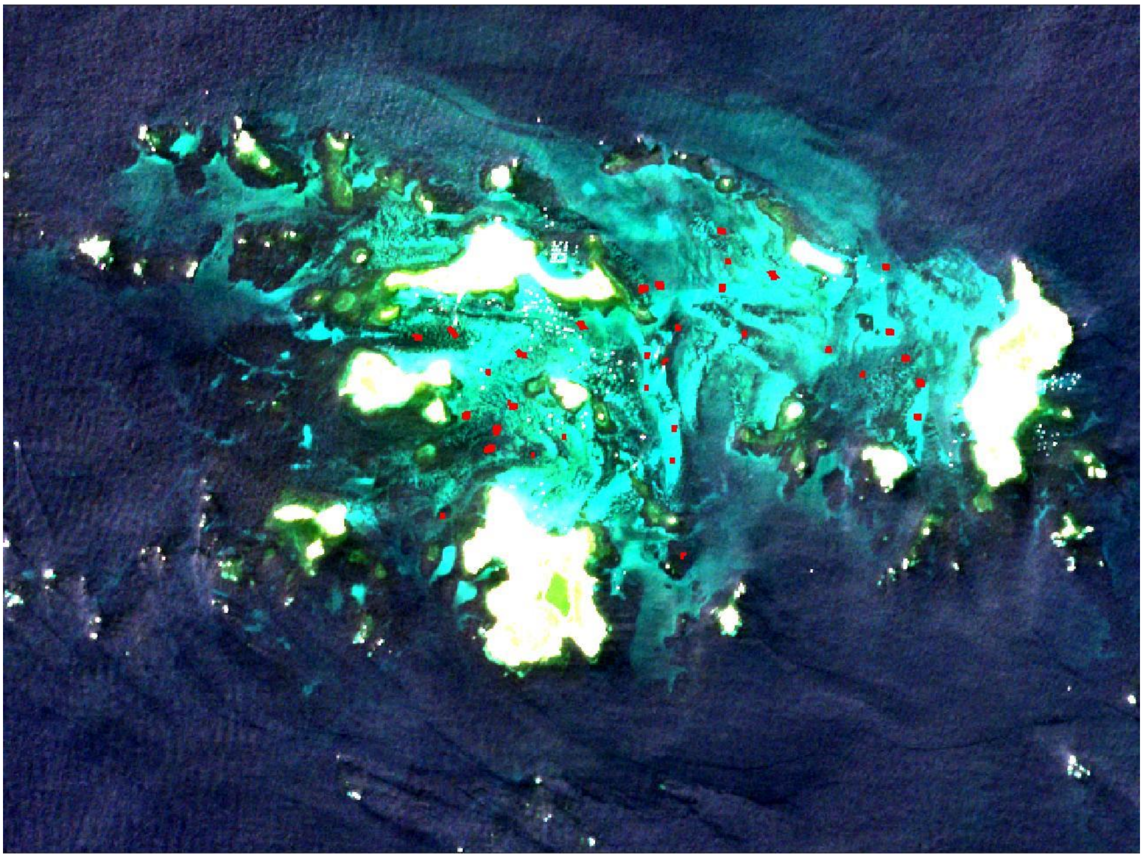

Figure 29 - Example map of stations for validation of R_{rs} over shallow waters

3.1.2 Chlorophyll-*a* (Chl-*a*)

Chlorophyll-*a* (Chl-*a*) products were developed for Sentinel-2 and -3, using the best-performing atmospheric corrections. These validation results are presented by region below, describing the algorithms tested where relevent. Overall, the NIR/Red 2-band ratio algorithm (Gitelson et al., 2011) and the Color Index algorithm (CI) (Hu et al., 2012) performed best in the Venice Lagoon and Adriatic Sea (Italy), the Gons et al. (2005) algorithm performed well in Wadden Sea (Netherlands), and the CI, the NDCI (Mishra and Mishra, 2012), and the Neural Network algorithms (Gonzalez Vilas et al., 2011) all achieved good performance for Ria de Vigo (Spain). More details about the algorithms and validation results are described below for each satellite sensor and region, with a summary of the best performing Chl-a algorithms presented in Table 18.

This project has received funding from the European Union's Horizon 2020 research and innovation programme under grant agreement No 776348

Table 18 - Best-performing Chl-a algorithms by region

Chl-a Algorithm performance					
Country	**Regions**	**Time**	**Satellite sensor**	**Atmospheric Correction**	**Best performing Chl-a algorithm**
Italy	Venice Lagoon and the Adriatic Sea	2018	S2 MSI	Polymer v4.8	NIR/Red 2-band ratio (Gitelson et al., 2011)
			S3 OLCI	C2RCC	CI (Hu et al., 2012)
Spain	Ria de Vigo	2018	S2 MSI	Polymer v4.8	CI (Hu et al., 2012)
			S3 OLCI	C2RCC	NDCI (Mishra & Mishra, 2012)
		2016-2018	S3 OLCI	Polymer v4.8	Neural Network (González Vilas, 2011)
Netherlands	Eemshaven	2017-2018	S2 MSI S3 OLCI	C2X augC2RCC	Semi-analytical (Gons et al., 2005)
	Oosterschelde	2018	S3 OLCI	augC2RCC	conc_chl product
	Wadden Sea	2018	S3 OLCI	augC2RCC	

3.1.2.1 Italy

Sentinel-2 MSI

A suite of empirical, semi-empirical and semi-analytical models for Chl-*a* retrieval from Sentinel-2 MSI were tested using the Venice 2018 dataset. Sentinel-2 data were atmospherically corrected with Polymer v4.8, as this model performed well (Section 3.1.1). These included a near infrared (NIR) to red 2-band ratio (BR) empirical model (Gitelson and Kondratyev, 1991; Dall'Olmo et al., 2003; Moses et al, 2009; Gitelson et al., 2011), the Polymer log_Chl product (Park and Ruddick, 2005; Steinmetz, 2011), a 3-band empirical model (Moses et al., 2009; Gilerson et al., 2010), the Normalised Difference Chlorophyll Index (NDCI; Mishra and Mishra, 2012), the NASA OC (Ocean Colour) 3-band algorithm (O'Reilly et al., 2000; OC3E), and the Colour Index (Hu et al., 2012).

Of these, the best performing algorithm for the Venice 2018 dataset was the NIR/Red 2-band ratio, which was tuned and implemented for Sentinel-2 as follows:

$$Chl - a\ (mg\ m^{-3}) = a\ \times [R_{rs}(705)/R_{rs}(665)] +\ b \qquad \text{Equation 5}$$

where a and b were tuned to the Venice 2018 dataset as 2.955 and 0.5215, respectively.

This project has received funding from the European Union's Horizon 2020 research and innovation programme under grant agreement No 776348

The validation scatterplots for all Chl-*a* algorithms tested are shown in Figure 30, and the error metrics are presented in Table 19. We note that Sentinel-2 Chl-*a* did not perform as well as the Sentinel-3 Chl-*a* product for this region, however this may simply be a result of the small sample size for the 2018 Venice dataset (n=12).

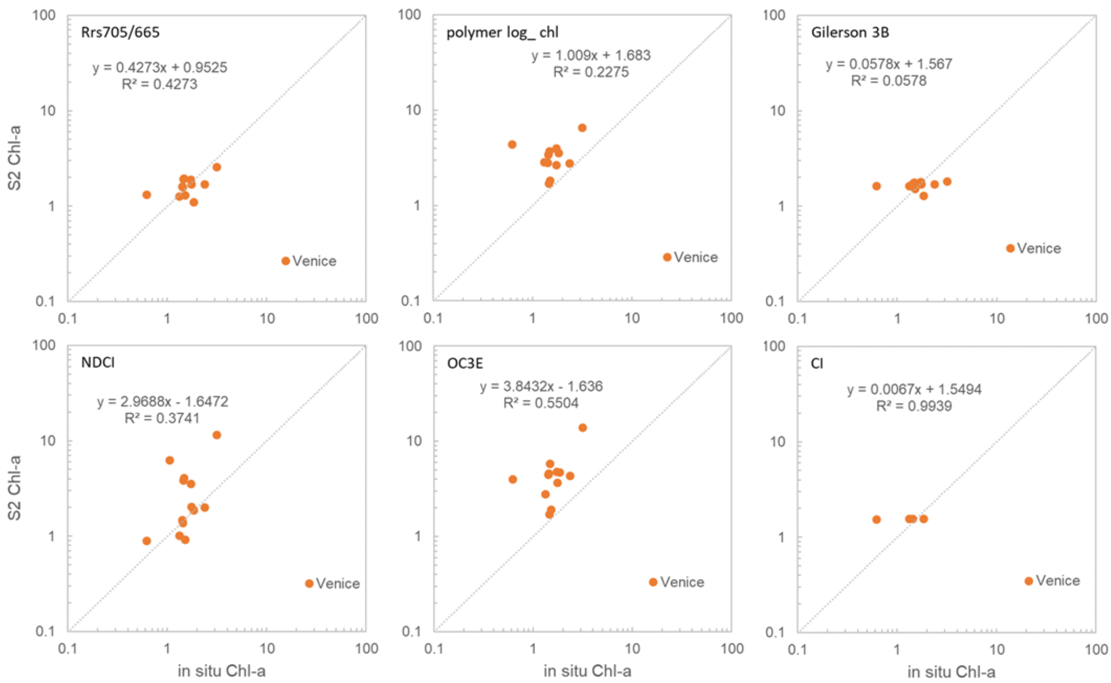

Figure 30 - Validation scatterplots for Venice 2018 Sentinel-2 Chl-*a* (unit: mg/m³), indicating R^2 and linear regression fits

Table 19 - Error metrics for CoastObs Sentinel-2 Chl-*a* product (unit: mg/m³), Venice 2018 dataset (n=12)

Algorithm	R^2	slope	$RMSE_{log}$	$Bias_{log}$	MAE_{log}	MAPE (%)
NIR/Red 2-band ratio	0.427	0.427	**0.138**	-0.017	**0.104**	**26.7%**
Polymer log_Chl	0.228	**1.009**	0.367	-0.306	0.306	131%
3-band empirical	0.058	0.058	0.161	-0.026	0.116	31.2%
NDCI	0.374	2.969	0.272	-0.134	0.201	72.1%

This project has received funding from the European Union's Horizon 2020 research and innovation programme under grant agreement No 776348

Algorithm	R^2	slope	$RMSE_{log}$	$Bias_{log}$	MAE_{log}	MAPE (%)
OC3E	0.550	3.843	0.468	-0.420	0.420	194.6%
CI	**0.994**	0.007	0.160	**0.000**	0.107	27.5%

Sentinel-3 OLCI

As with Sentinel-2, several Chl-*a* algorithms were tested with the Venice 2018 dataset for C2RCC atmospherically corrected Sentinel-3 data. These include the C2RCC conc_chl (Brockmann et al, 2016), a near infrared (NIR) to red 2-band ratio (BR) empirical model (Gitelson and Kondratyev, 1991; Dall'Olmo et al., 2003; Moses et al, 2009; Gitelson et al., 2011), a 3-band empirical model (Moses et al., 2009; Gilerson et al., 2010), the Normalised Difference Chlorophyll Index (NDCI; Mishra and Mishra, 2012), the NASA OC (Ocean Colour) 4-band algorithm (O'Reilly et al., 2000; OC4E) and the Sentinel-3 OC 4-band algorithm (Morel et al, 2007; OC4ME), and the Colour Index (Hu et al., 2012).

Of these, the best performing algorithm for the Venice 2018 dataset was the Colour Index (CI), which was tuned and implemented for Sentinel-3 as follows:

$$CI = R_{rs}(560) - \left[R_{rs}(443) + \frac{560-443}{665-443} \times \left(R_{rs}(665) - R_{rs}(443)\right)\right] \quad \text{Equation 6}$$

$$Chl - a\ (mg\ m^{-3}) = 0.7646 * exp(91.294 * CI) \quad \text{Equation 7}$$

Validation results are presented as scatterplots and a table of error metrics for each Chl-*a* model tested with the Venice 2018 dataset (Figure 31; Table 20). An example Chl-*a* product map is also shown for the Venice Lagoon, Italy (Figure 32). The Sentinel-3 Chl-*a* outperformed the Sentinel-2 Chl-*a* product, however this requires further validation to increase confidence due to the small sample size for 2018 (n=11).

This project has received funding from the European Union's Horizon 2020 research and innovation programme under grant agreement No 776348

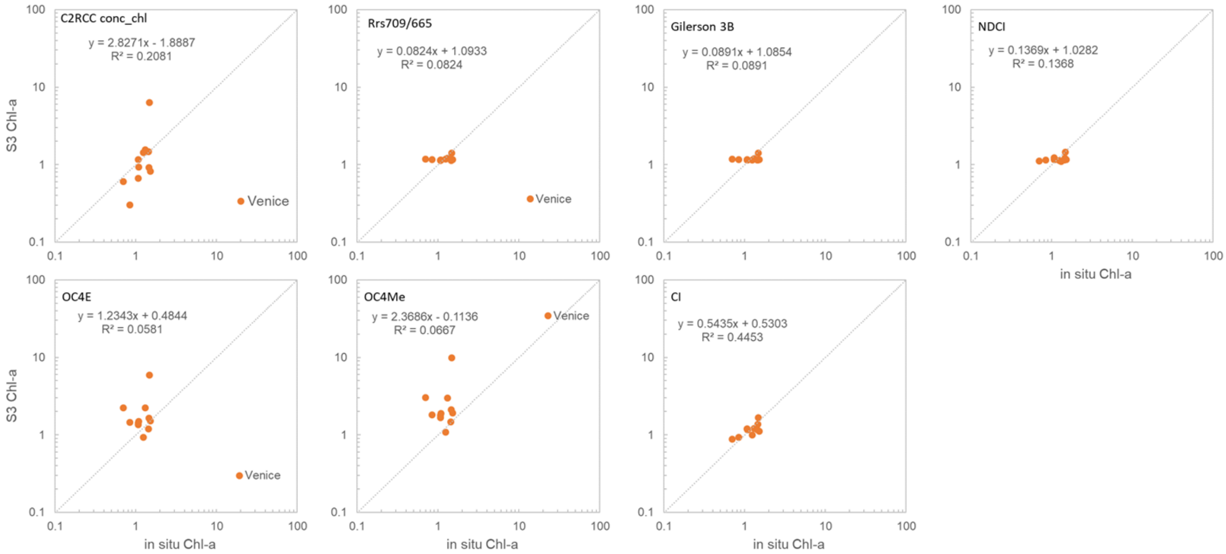

Figure 31 - Validation scatterplots for Venice 2018 Sentinel-3 Chl-*a* (unit: mg/m³), indicating R^2 and linear regression fits

Table 20 - Error metrics for CoastObs Sentinel-3 Chl-*a* product (unit: mg/m³), Venice 2018 dataset (n=11)

Algorithm	R^2	slope	$RMSE_{log}$	$Bias_{log}$	MAE_{log}	MAPE (%)
C2RCC conc_chl	0.208	2.83	0.263	0.033	0.187	53.9%
NIR/Red 2-band ratio	0.0824	0.0824	0.100	-0.011	0.076	19.0%
3-band empirical	0.0891	0.0891	0.100	-0.011	0.077	19.2%
NDCI	0.137	0.137	0.097	-0.010	0.080	19.5%
OC4E	0.0581	**1.23**	0.273	-0.168	0.204	75.9%
OC4Me	0.0667	2.37	0.375	-0.281	0.290	133%
CI	**0.445**	0.544	**0.072**	**0.000**	**0.064**	**14.5%**

This project has received funding from the European Union's Horizon 2020 research and innovation programme under grant agreement No 776348

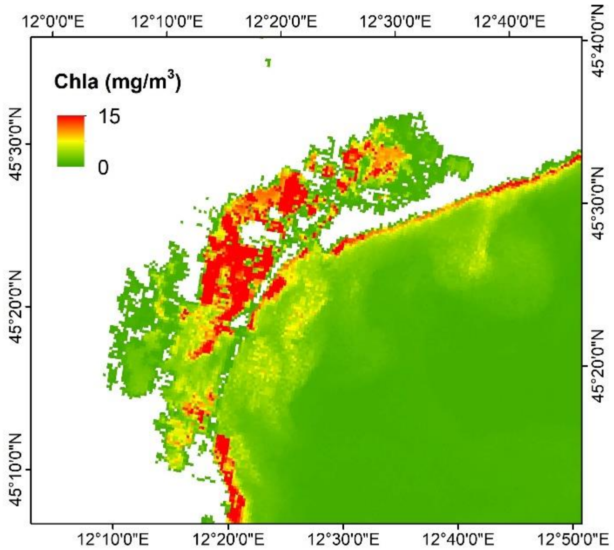

Figure 32 - Example map of Sentinel-3 Chl-*a* product (Colour Index) for Venice Lagoon, Italy on 26 June 2018.

3.1.2.2 Netherlands

Sentinel-2 MSI and Sentinel-3 OLCI - Eemshaven

Chl-*a* was derived from S3 and S2 R_{rs} using the Gons et al. (2005) algorithm applied to the atmospherically corrected flagged satellite data (augC2RCC and C2X, for S3 and S2, respectively). The model was applied with an adjustment to the Chl-*a* absorption coefficient, according Hommersom et al. (2009).

Validation with data obtained from Eemshaven site shows that after August 2017, the Chl-*a in situ* sensor is stagnated to values between 2.1 and 4.5 mg.m^{-3}, orange coloured data points (Figure 33).

This project has received funding from the European Union's Horizon 2020 research and innovation programme under grant agreement No 776348

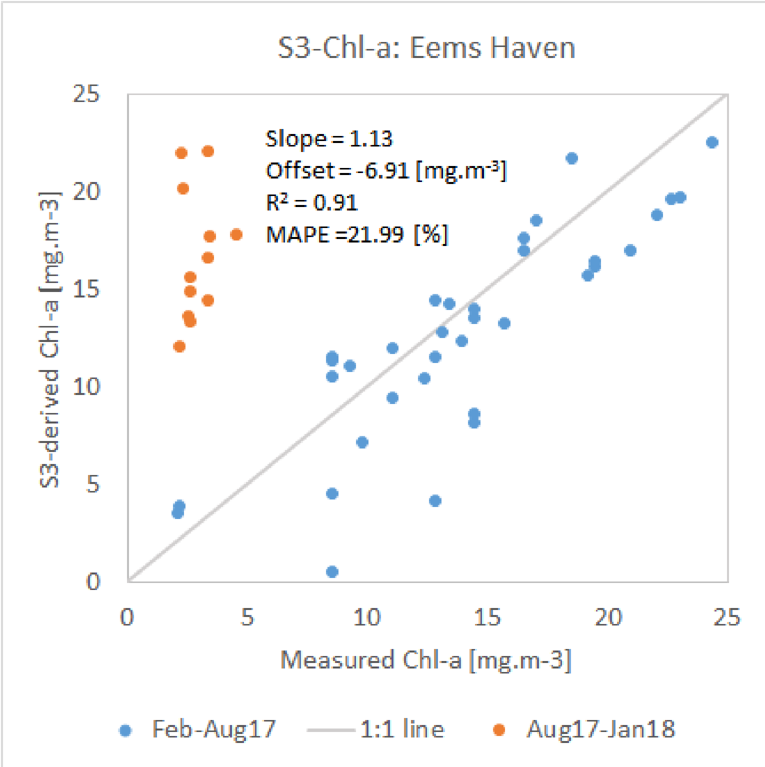

Figure 33 - Validation of S3 derived Chl-*a* concentrations using the Eemshaven data set.

The accuracy of S3-Chl-*a* product (without the orange data points, i.e. data after 25th Aug 2017) is relatively high with MAPE much less than the targeted accuracy by space agencies (of 30-35%), with high value of R^2 (0.96) and a slope that is 13% off unity. Similar to S3, S2 Chl-*a* retrievals are accurate with MAPE below 20%, high R^2 (0.87) and a slope (1.01) close to unity (Figure 34).

The summary of the validation results of S2 and S3 retrievals of Chl-*a* is shown in Table 21. From the Eemshaven data we excluded the data corresponding to dates from August 2017 to January 2018 because the field sensor exhibited erroneous measurements.

This project has received funding from the European Union's Horizon 2020 research and innovation programme under grant agreement No 776348

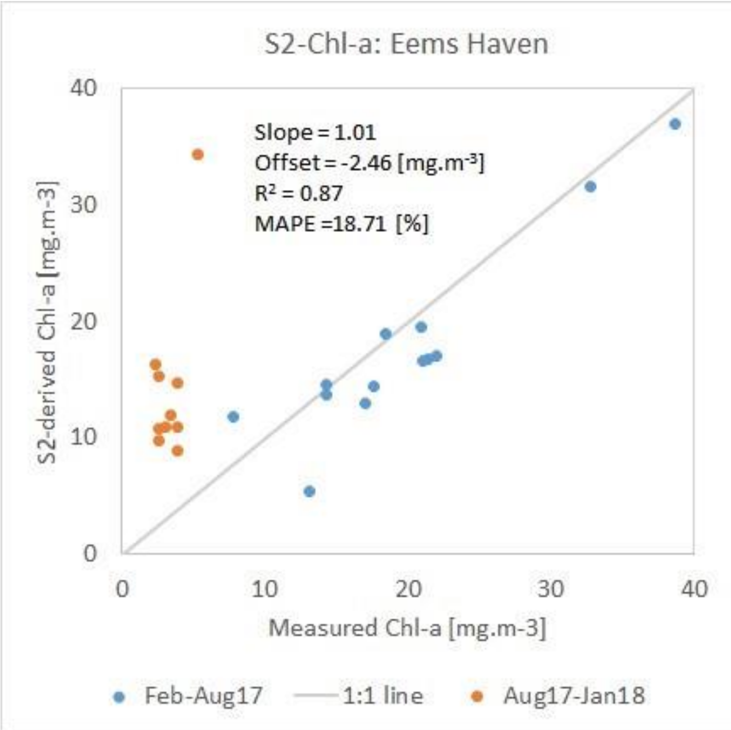

Figure 34 - Validation of S2 derived Chl-*a* concentrations using the Eemshaven data set.

Table 21- Accuracy of S2 and S3 retrievals of Chl-*a*

Product	R^2	slope	RMSE	MAPE (%)
Sentinel-3 Chl-a	0.96	1.02	2.92	16.81
Sentinel-2 Chl-a	0.87	1.01	4.01	18.71

Sentinel-3 OLCI - Oosterschelde and Wadden Sea

The S3 AugC2RCC 'conc_chl' product was evaluated for the Oosterschlede estuary and Wadden Sea 2018 dataset. Validation scatterplots for S3 Chl-*a* with HPLC analysed Chl-*a* data obtained during the 2018 CoastObs sampling campaigns are shown in Figure 35, with error metrics presented in Table 22 and an example Chl-*a* map in Figure 36.

This project has received funding from the European Union's Horizon 2020 research and innovation programme under grant agreement No 776348

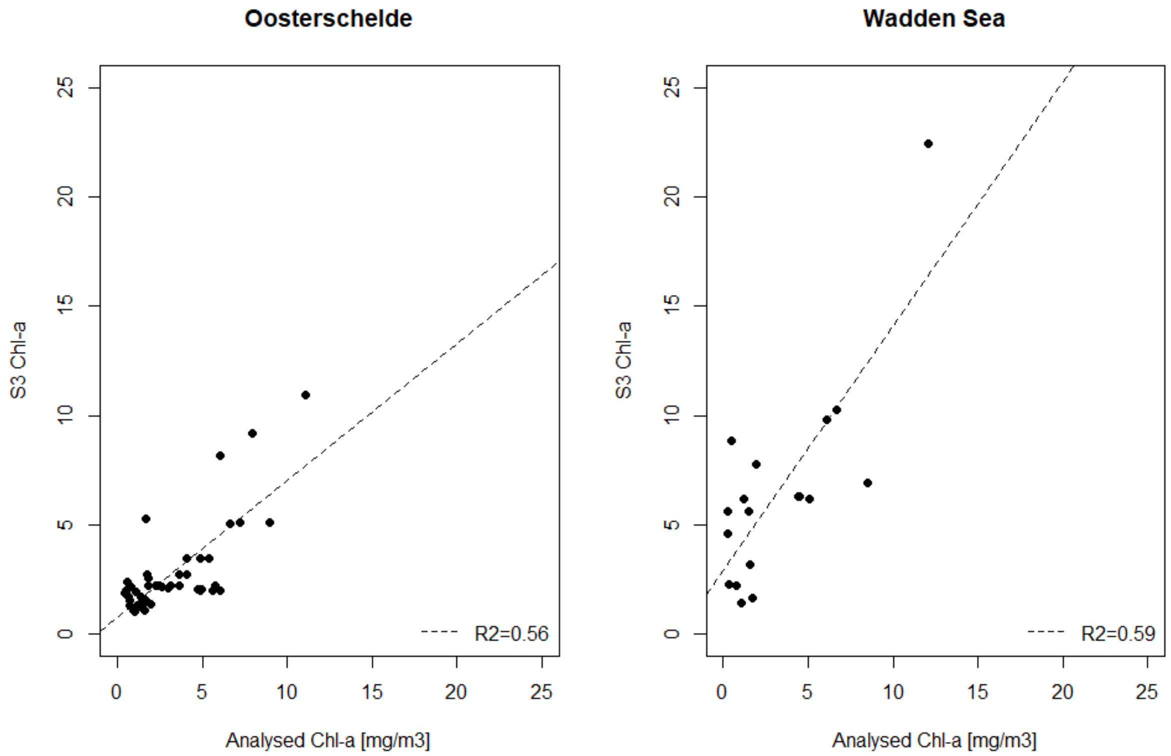

Figure 35 - Validation scatterplots for S3 Chl-*a* product for the Oosterschelde Estuary (n=47) and Wadden Sea (n=17), indicating R^2 and linear regression fit.

Table 22 - Error metrics for S3 standard Chl-*a* product for the Netherlands

Product	R^2	slope	$RMSE_{log}$	$Bias_{log}$	MAE_{log}	N
Oosterschelde	0.56	0.62	0.62	0.0029	0.48	47
Wadden Sea	0.59	1.12	1.49	-1.09	1.11	17

This project has received funding from the European Union's Horizon 2020 research and innovation programme under grant agreement No 776348

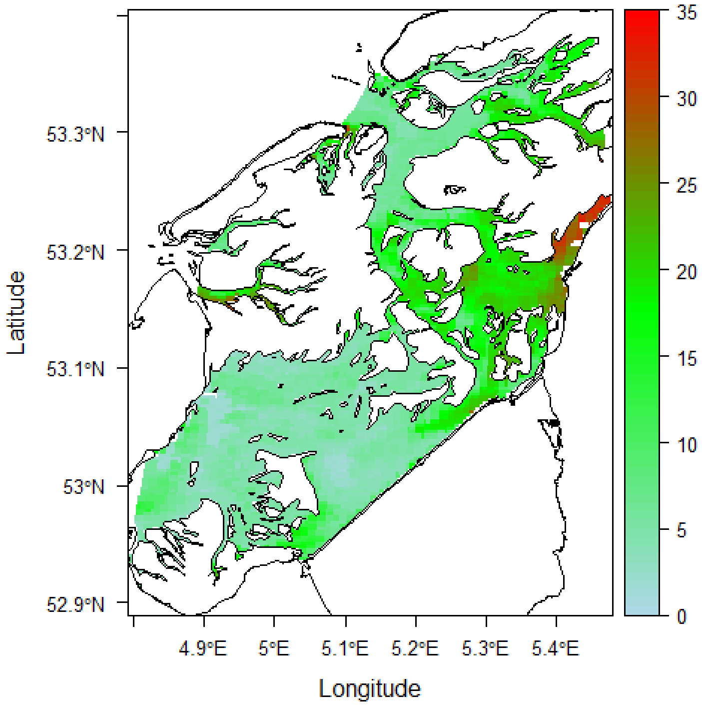

Figure 36 - Example map of S3 Chl-*a* product (unit: mg/m³) for the Wadden Sea study area on 03.05.2018. Intertidal areas are excluded.

3.1.2.3 Spain

Sentinel-2 MSI

The same suite of algorithms tested for Sentinel-2 using the Venice 2018 dataset were also implemented for the Vigo 2018 dataset (see 3.1.2.1). Sentinel-2 data were atmospherically corrected with Polymer v4.8.

Of these, the OC3E and CI algorithms showed comparable performance (Figure 37; Table 27). However, the lowest errors were for the CI algorithm, which was tuned and implemented as follows:

$$CI = R_{rs}(560) - \left[R_{rs}(443) + \frac{560-443}{665-443} \times \left(R_{rs}(665) - R_{rs}(443)\right)\right] \qquad \text{Equation 8}$$

$$Chl - a\ (mg\ m^{-3}) = 0.9477 * exp(358.66 * CI) \qquad \text{Equation 9}$$

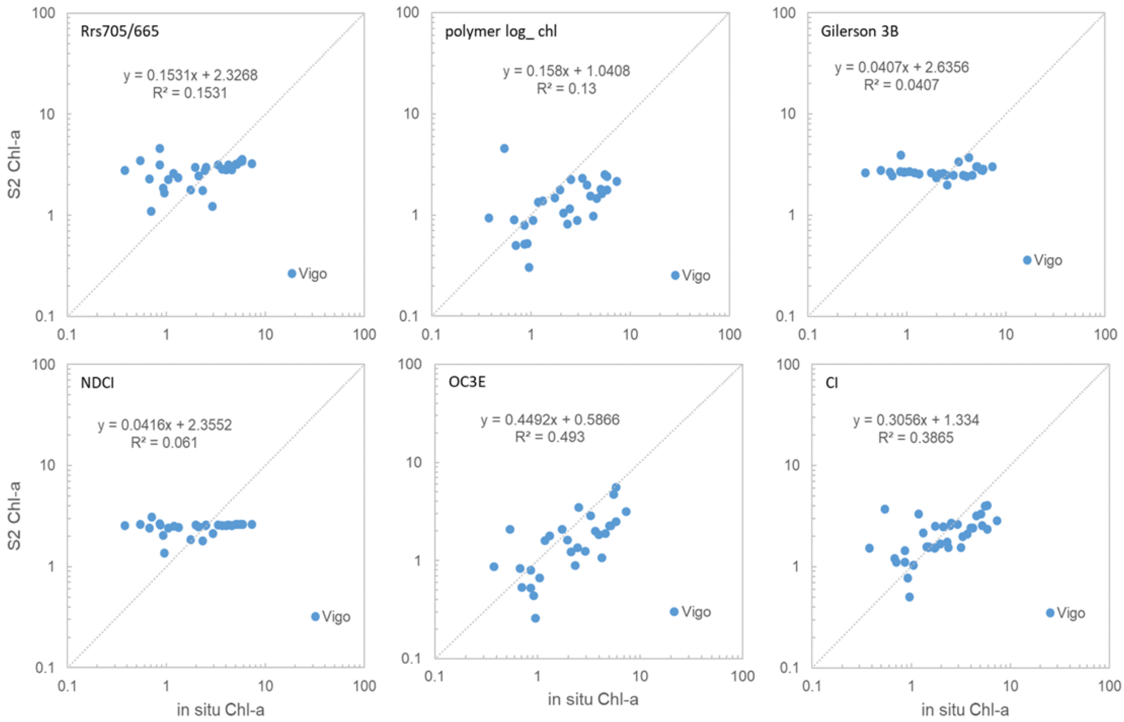

Figure 37 - Validation scatterplots for the Vigo 2018 Sentinel-2 Chl-*a* product (unit: mg/m³), indicating R² and linear regression fits

Table 23 - Error metrics for CoastObs Sentinel-2 Chl-*a* product (unit: mg/m³), Vigo 2018 dataset (n=29)

Algorithm	R^2	slope	$RMSE_{log}$	$Bias_{log}$	MAE_{log}	MAPE (%)
2-band ratio	0.153	0.153	0.357	-0.110	0.279	112%
Polymer log_Chl	0.130	0.158	0.382	0.209	0.315	72.0%
3-band empirical	0.041	0.041	0.375	-0.125	0.305	119%
NDCI	0.061	0.042	0.360	-0.078	0.296	107%
OC3E	**0.493**	**0.449**	0.304	0.150	0.256	**52.0%**
CI	0.387	0.306	**0.285**	**0.000**	**0.222**	69.9%

This project has received funding from the European Union's Horizon 2020 research and innovation programme under grant agreement No 776348

Sentinel-3 OLCI

The Chl-*a* models tested for the Spain coastal waters were derived either for use in the phytoplankton size class (Section 3.2.2) or the harmful algal bloom product (Section 3.2.4). The validation results for these are thus presented by their use in the relevant higher level product, however we note there are comparable results for all Sentinel-3 Chl-*a* products.

Chl-*a* for Phytoplankton Size Class Product

The same suite of algorithms tested for Sentinel-3 using the Venice 2018 dataset were also implemented for the Vigo 2018 dataset (see Section 3.1.2.1), using data atmospherically corrected with C2RCC.

Of these, the best performing algorithm was the Normalised Difference Chlorophyll Index (NDCI). This was tuned and implemented for Sentinel-3 as follows:

$$NDCI = \frac{R_{rs}(705)-R_{rs}(665)}{R_{rs}(705)+R_{rs}(665)} \qquad \text{Equation 10}$$

$$Chl-a\ (mg\ m^{-3}) = a + (b \times NDCI) + (c \times NDCI^2) \qquad \text{Equation 11}$$

where a, b and c were tuned to -17.308,-183.68, -361.9, respectively, using the Vigo 2018 dataset.

Sentinel-3 Chl-*a* validation results for the Vigo 2018 dataset are shown in Figure 38 and Table 24, with an example Chl-*a* product map in Figure 39.

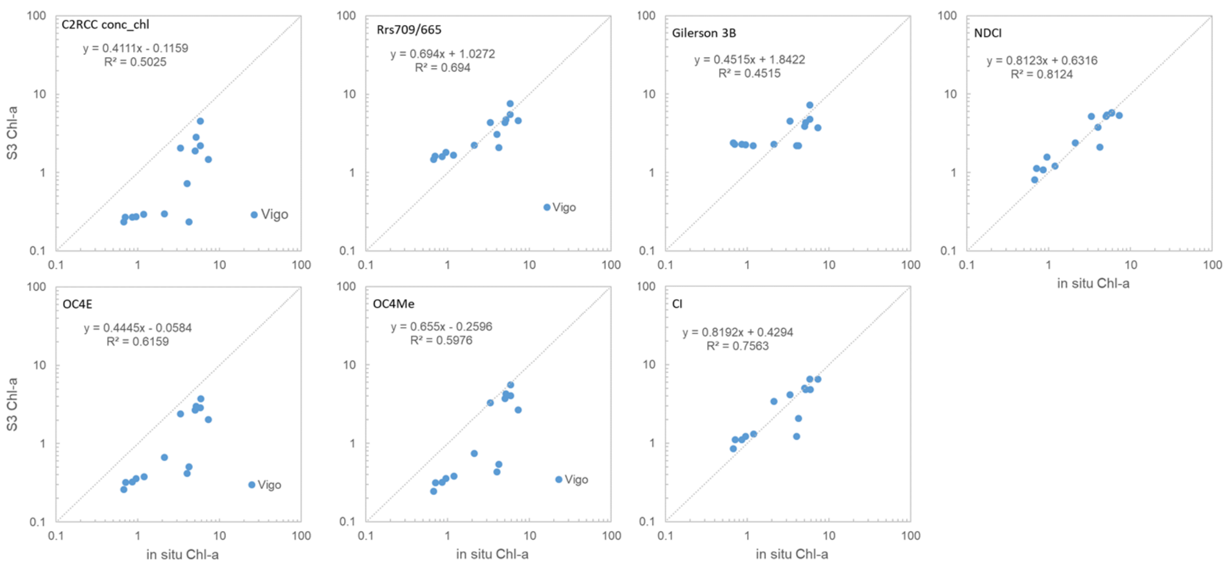

Figure 38 - Validation scatterplots for Vigo 2018 Sentinel-3 Chl-*a* (unit: mg/m³), indicating R^2 and linear regression fit

This project has received funding from the European Union's Horizon 2020 research and innovation programme under grant agreement No 776348

Table 24 - Error metrics for CoastObs Sentinel-3 Chl-*a* product (unit: mg/m³), Vigo 2018 dataset (n=14)

Algorithm	R^2	slope	$RMSE_{log}$	$Bias_{log}$	MAE_{log}	MAPE (%)
C2RCC conc_chl	0.208	2.827	0.600	0.531	0.531	65.0%
2-band ratio	0.694	0.694	0.209	-0.069	0.172	48.5%
3-band empirical	0.452	0.452	0.301	-0.097	0.251	82.5%
NDCI	**0.812**	**0.812**	**0.136**	**-0.034**	**0.100**	**24.7%**
OC4E	0.616	0.445	0.499	0.439	0.439	58.9%
OC4Me	0.598	0.655	0.466	0.372	0.372	49.2%
CI	0.756	0.819	0.189	0.000	0.138	29.7%

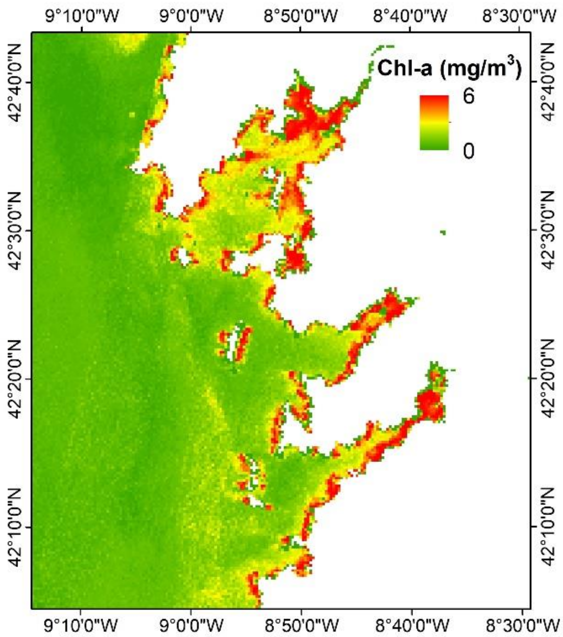

Figure 39 - Example map of Sentinel-3 Chl-*a* product (NDCI) for Galician Rias, Spain on 08 July 2018.

This project has received funding from the European Union's Horizon 2020 research and innovation programme under grant agreement No 776348

Chl-*a* for Harmful Algal Bloom Product

A regional Chl-*a* algorithm based on Sentinel-3 images was developed for the Galician area following the methodological approach proposed by Gonzalez Vilas *et al*. (2011) for MERIS images. Data and methods for this product were explained in the Harmful Algae Bloom Species Product Documentation (D 3.6).

This method uses a fuzzy C-Mean clustering algorithm to define the application scope, and then applies a neural network (NN) algorithm to estimate the Chl-*a* concentrations. As explained in D 3.6, a different NN algorithm was developed for each one of the two clusters identified in the study area: NNRB-Cl#1 and NNRB-Cl#2.

Algorithms were developed using a match-ups dataset derived from 35 Sentinel-3 images between April 2016 and November 2018 and *in situ* Chl-*a* concentrations from the INTECMAR monitoring program (see D 3.6). Moreover, an independent match-ups dataset was built using *in situ* Chl-*a* concentrations from the dedicated CoastObs campaigns (May-June 2018; June 2019) and from the INTECMAR monitoring program between December 2018 and April 2019.

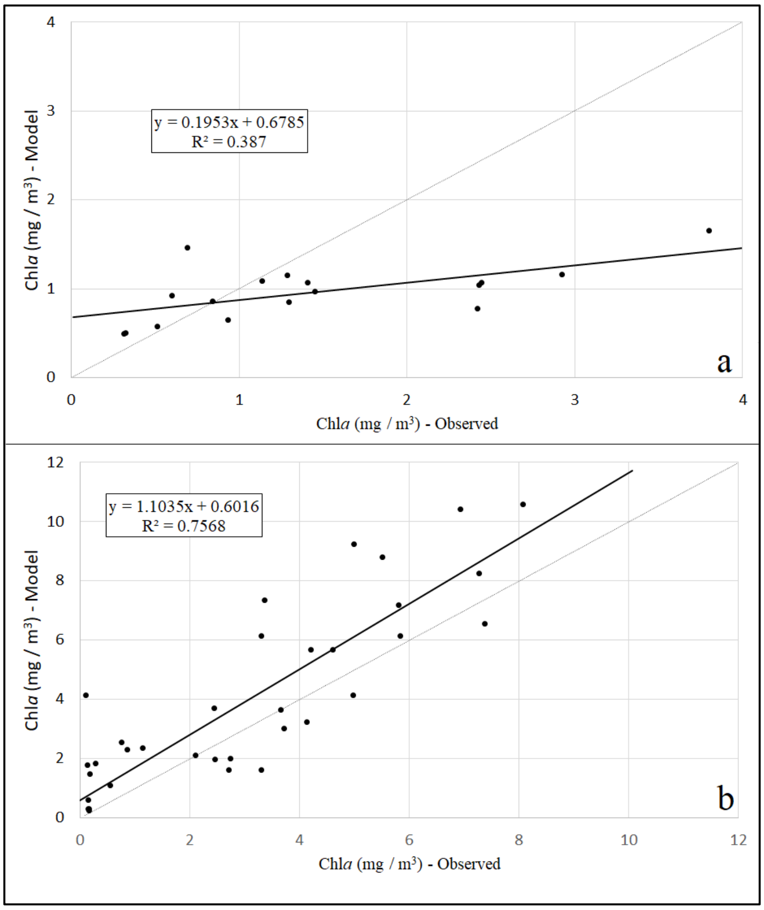

Figure 40 - Validation scatterplots obtained from the independent test dataset. a) NNRB-Cl#1 b) NNRB-Cl#2

This project has received funding from the European Union's Horizon 2020 research and innovation programme under grant agreement No 776348

Figure 40 shows the relationships between the modelled and observed Chl-*a* concentrations using only data from the independent test set for both algorithms. Table 25 summarized the error metrics computed using both the dataset used for the development of the algorithms and for the independent test dataset. The development dataset include data from the training and validation sets (see D 3.6).

Table 25 - Error metrics for NNRB-Cl#1 and NNRB-Cl#2, computed from the datasets used for the developent of the algorithms and from the independent test set.

Product	N	R^2	slope	RMSE	Bias	MAE
NNRB-Cl#1 – Dev.	116	0.81	0.96	0.23	0.06	0.18
NNRB-Cl#1 – Test	30	0.39	0.20	0.96	-0.49	0.68
NNRB-Cl#2– Dev.	193	0.89	0.94	0.87	0.10	0.49
NNRB-Cl#2– Test	37	0.76	1.10	1.80	0.89	1.36

As expected, results from the test datasets are worse than the obtained ones from the development datasets. In fact, NNRB-Cl#1 results are clearly worse, evidencing that this algorithm is not robust enough for producing reliable results, although a linear trend is observed (Figure 40).

As compared to NNRB-Cl#1, NNRB-Cl#2 shows a better fitting with a lower difference between the R^2 values computed from the development and test datasets. It also shows a clear positive deviation from the expected concentrations (Figure 40) in the test dataset (bias = 0.89), which however it is not observed in the development dataset (bias = 0.10).

Despite of the better fitting observed in NNRB-Cl#2, error metrics (i.e. RMSE and MAE) shows lower values in NNRB-Cl#1. This could be explained by the lower Chl-*a* range observed in Cluster#1, with more than 90% of the values lower than 4 mg m^{-3}. However, Cluster#2 shows a greater range and NNRB-Cl#2 results are more affected by Chl-*a* peaks (concentrations up to 10 mg m^{-3}).

Figure 41 shows a Chl-*a* map obtained from a Sentinel-3 image on 19 June 2018 using the NNRB-Cl#2 algorithm.

This project has received funding from the European Union's Horizon 2020 research and innovation programme under grant agreement No 776348

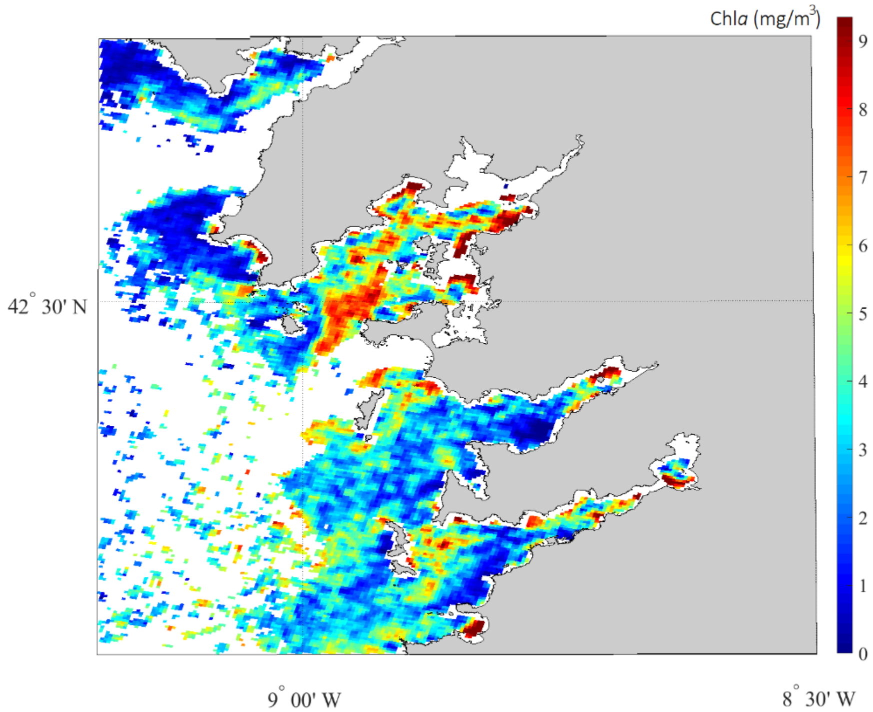

Figure 41 - Chl-*a* map from NNRB-Cl#2 for 19 June 2018

3.1.3 Total Suspended Matter (TSM) and Turbidity

Total suspended matter (TSM) products (also referred to as suspended particulat matter, SPM) were developed for Sentinel-2 and -3, using the best-performing atmospheric correction. These validation results are presented by region below, describing the algorithms tested, where relevent. The Nechad et al. (2010) algorithm was chosen and tuned to regional datasets for TSM estimation in most of the studied regions (e.g. Italy, Netherlands, and Spain) and indicated generally good performance for each region. In particular, the band-switching algorithm for turbid esturies by Novoa et al. (2017) was chosen in Loire estuary (France) where the TSM values reached ~2000 g/m^3. The Dogliotti et al. (2015) algorithm was chosen and tuned to the Venice Lagoon (Italy) dataset to estimate water turbidity. More details about the algorithms used and validation results are described below.

This project has received funding from the European Union's Horizon 2020 research and innovation programme under grant agreement No 776348

Table 26 - Best-performing TSM and turbidity algorithms by region

TSM and Turbidity algorithm performance					
Country	**Regions**	**Time**	**Satellite sensor**	**Atmospheric Correction**	**Best performing algorithm**
France	Loire Estuary	2016	S2 MSI	ACOLITE	band-switching algorithm (Novoa et al., 2017; Gernez et al., 2017)
Italy	Venice Lagoon	Jan-May 2019	S2 MSI	ACOLITE	Turbidity – (Dogliotti et al., 2015)
			S2 MSI and L8	ACOLITE	TSM – (Nechad et al., 2010)
Spain	Ria de Vigo	2018	S3 OLCI	C2RCC	Nechad et al., 2010
Netherlands	Eemshaven	2017-2018	S2 MSI	C2X	Nechad et al., 2010
			S3 OLCI	augC2RCC	Nechad et al., 2010

3.1.3.1 France

In the Loire estuary (north of Bourgneuf Bay), the concentration of total suspended matter (TSM) was computed using a band-switching algorithm developed for turbid nearshore waters (Novoa et al., 2017) and specifically calibrated for Sentinel-2 (Gernez et al., 2017). High-frequency automated *in situ* turbidity measurements from the SYVEL monitoring network[1] were used to validate Sentinel-2 derived TSM data for 2016, as described in detail in D3.8 (see also Figure 42 below, and Table 27).

[1] http://www.loire-estuaire.org/dif/do/init

This project has received funding from the European Union's Horizon 2020 research and innovation programme under grant agreement No 776348

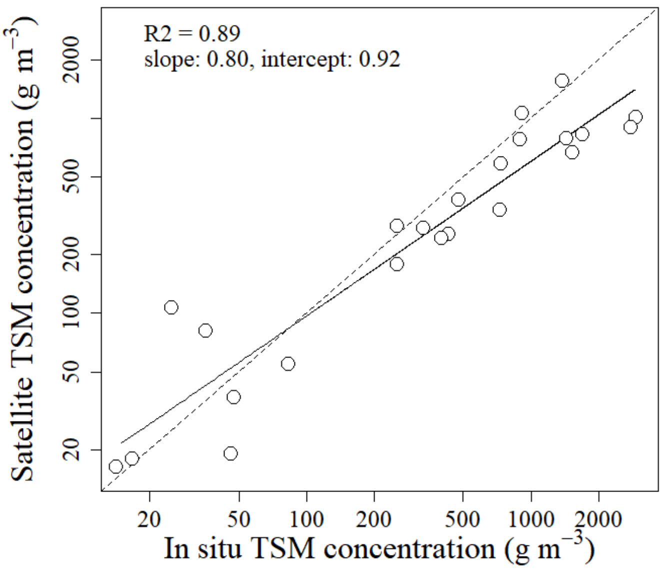

Figure 42 - Validation scatterplot for TSM CoastObs product, indicating R^2 and linear regression fit.

Table 27 - Error metrics for TSM CoastObs product

TSM	R^2	slope	RMSE_log	Bias_log	MAE_log	N
Loire estuary	0.89	0.80	0.14	-0.26	0.51	23

3.1.3.2 Italy

Intensive and expeditive fieldworks were undertaken in the LV to gather data for the purpose of validating CoastObs standard products, including water reflectance and water-quality parameters (turbidity and SPM). Here SPM (suspended particulate matter) has the same meaning with TSM (total suspended matter).

Starting from January 2019 to May 2019, 14 campaigns were carried out, synchronous with the passage of Landsat 8 (L8) and Sentinel-2 (S2) satellites. The measurement stations were located in the area of the Lido tidal mouth and in the central sector of the lagoon. In the area of Lido inlet, the 6-8 stations were distributed along the channel network from lagoonal waters to the littoral zone, following the tidal current. The stations were visited in different tidal and meteorological conditions, which influenced the natural variability of suspended sediment load and circulation. Thus, a subsequent wide range of water transparency was measured in a few kilometres (Secchi depths ranged from 1 to 5 meters) and suspended inorganic sediment was the main factor in determining the optical water quality.

This project has received funding from the European Union's Horizon 2020 research and innovation programme under grant agreement No 776348

A total of 120 stations were visited with a maximum time difference of 1 h from the satellite overpasses, because of the short-term variability of water physical and chemical properties and turbidity in the study area. At each station, above water remote sensing reflectances were measured with the WISP-3 spectroradiometer (Water Insight), CTD profiles were performed with Ocean Seven 316Plus multi-parameter probe (Idronaut) equipped with optical backscattering sensor for the measurement of turbidity at 880 nm (Seapoint) and water transparency was assessed with Secchi Disk. Discrete surface water samples were also collected and subsequently filtered in the laboratory, to estimate the concentration of suspended particulate matter (SPM) with the determination of the organic and inorganic components.

The list of campaigns carried out has been summarized in Table 5. Figure 43 shows the map and the coordinates of the stations investigated.

a)

b)

c)

	Lat	Long
ST1	45.42670	12.37400
ST2	45.43170	12.37880
ST3	45.42670	12.42320
ST4	45.41830	12.44630
ST5	45.43585	12.39185
ST6	45.43120	12.40854
ST7	45.44516	12.41955
ST8	45.40795	12.45942

Figure 43 - a) Study area with location of fieldwork activities carried out from January to May 2019 (red dots: measurement stations on 20th March 2019 in the central sector of the LV; yellow dots: revisited stations at the Lido inlet; b) Zoom on the revisited stations at the Lido inlet; c) Coordinates of the revisited stations at the Lido inlet.

Turbidity

The ACOLITE-derived water leaving reflectance ($\rho_w(\lambda)$) were converted in turbidity (T, expressed in formazin nephelometric unit [FNU]), as follows (Dogliotti et al., 2015):

$$Turbidity\ [FNU] = \frac{A_T^{\lambda}\rho_W(\lambda)}{1-\ \rho_W(\lambda)/C^{\lambda}} \qquad \text{Equation 12}$$

This project has received funding from the European Union's Horizon 2020 research and innovation programme under grant agreement No 776348

where ρ_w refers to Sentinel-2 spectral band 4 (red) or band 8 (near infrared) and to Landsat 8 spectral band 4 (red) or band 5 (near infrared), and A_T and C were two wavelength-dependent calibration coefficients taken from Nechad et al. (2009) and recalibrated to Landsat and Sentinel-2 spectral ranges. The parameter C was calibrated using "standard" inherent optical properties (IOPs) as described in Nechad et al. (2010), while the A_T coefficient was obtained by a non-linear least-square regression analysis using *in situ* measurements of T and rw in various European and South American coastal and estuarine environments (Dogliotti et al., 2015).The algorithm is reliable over a wide range of turbidity values (1-1500 FNU), avoiding saturation issues by adopting a band-switching scheme between red and near infrared ranges (Dogliotti et al., 2015). In the case of Venice Lagoon, we had better performance with the Red band and we decided not to apply the band-switching scheme. For the case of Po river plume, the band-switching scheme was adopted because of the higher turbidity values, as demonstrated in Brando et al. (2015) and Braga et al. (2017).

In situ collected turbidity data that we considered the mean value of the upper 1-m profile data by cast were used to assess the accuracy of T and SPM products derived from L8 and S2 imagery.

A total of 105 match-ups (78 with S2 and 27 with L8, 20 of those with both S2 and L8) between satellite and *in situ* data collection were available by considering a maximum time difference of 1 h. Figure 44 shows the scatter plots of the L8 and S2 derived estimates of turbidity versus *in situ* measurements: the correlations were statistically significant with a coefficient of correlation r of 0.975 and 0.984, a coefficient of determination R^2 of 0.9518 and 0.9698, and the same RMSE of 2.48, for the S2 and L8 derived turbidity, respectively. See Table 28 for the complete statistics of fitting. An example of turbidity maps derived from near-simultaneous overpasses of Sentinel-2 (overpass time 10:13 UTC) and Landsat 8 (overpass time 09:58 UTC) on 24/01/2019 is shown on Figure 45.

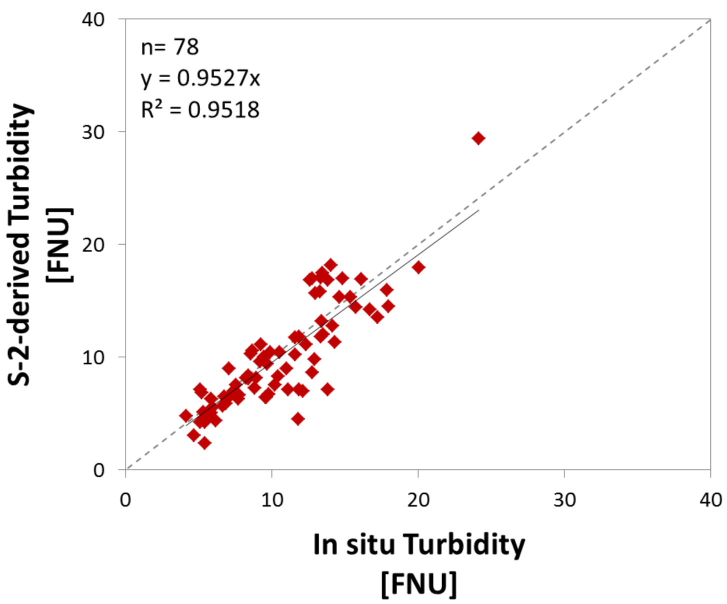

a)

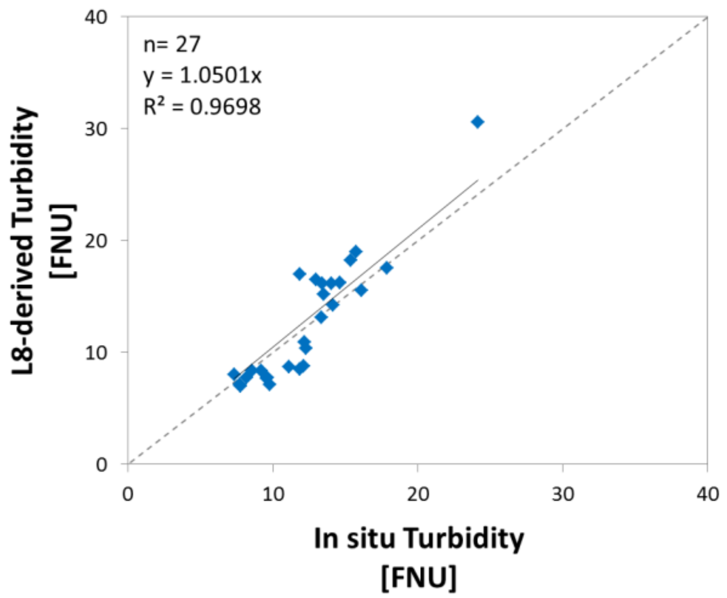

b)

Figure 44 - Validation scatterplot(s) for Turbidity CoastObs product, indicating R^2 and linear regression fit. a) Sentinel-2; b) Landsat 8. In both plots, the number of samples (n) and the 1:1 line is plotted as dotted lines.

This project has received funding from the European Union's Horizon 2020 research and innovation programme under grant agreement No 776348

Table 28 - Error metrics for Turbidity CoastObs products

Product	R^2	slope	RMSE	Bias	MAE	N
LV/turbidity S2	0.9518	0.9527	2.48 FNU	-0.59	1.90 FNU	78
LV/turbidity L8	0.9698	1.050	2.48 FNU	0.276	1.95 FNU	27

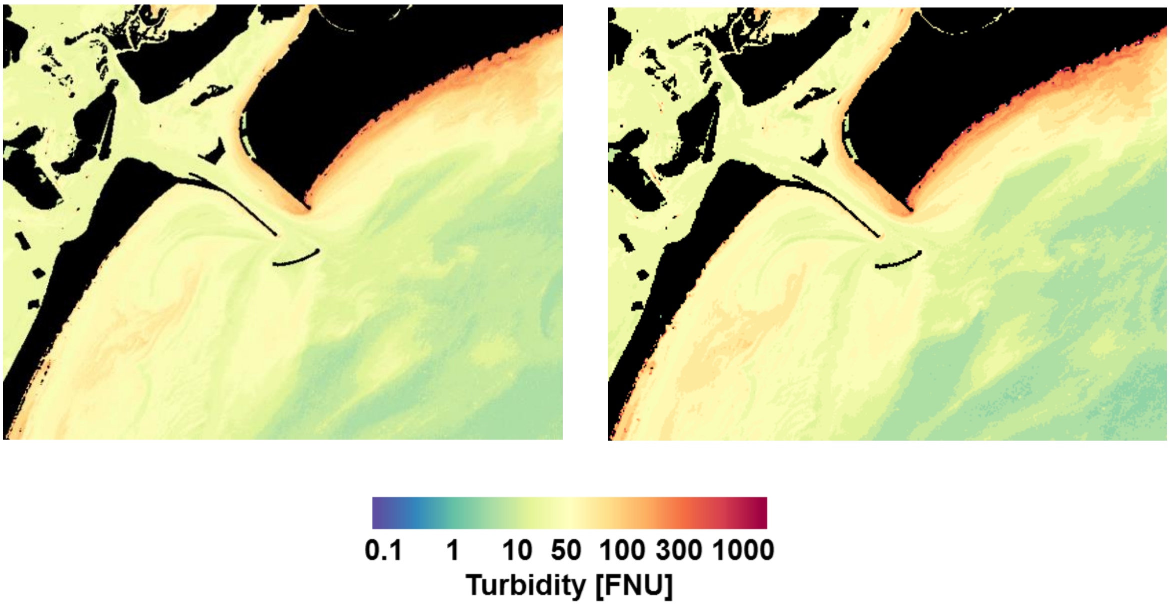

Figure 45 - Example maps of Turbidity CoastObs product for 24.01.2019. a) Sentinel-2 (overpass time 10:13 UTC); b) Landsat 8 (overpass time 09:58 UTC).

The intercomparison of turbidity products for near-simultaneous overpasses of L8 and S2 with all the available matchups (3 field campaigns, n=20) is also shown in Figure 46. The scatterplot reveals a quite good product consistency under different atmospheric/aquatic conditions (very turbid water on 24 January; turbid water on 25 February and clear water on 22 March 2019). Turbidity (Dogliotti et al., 2015) derived from L8 and S2 were, on average, in good agreements, i.e., ΔT = 1.56 FNU, with S2 producing lower values. In the Lagoon of Venice, the constellation of Landsat-8 and Sentinel-2A/B data enables a 2-3 day revisit time, so the aquatic science and end-user community can benefit from high-quality and consistent products for operational purposes.

This project has received funding from the European Union's Horizon 2020 research and innovation programme under grant agreement No 776348

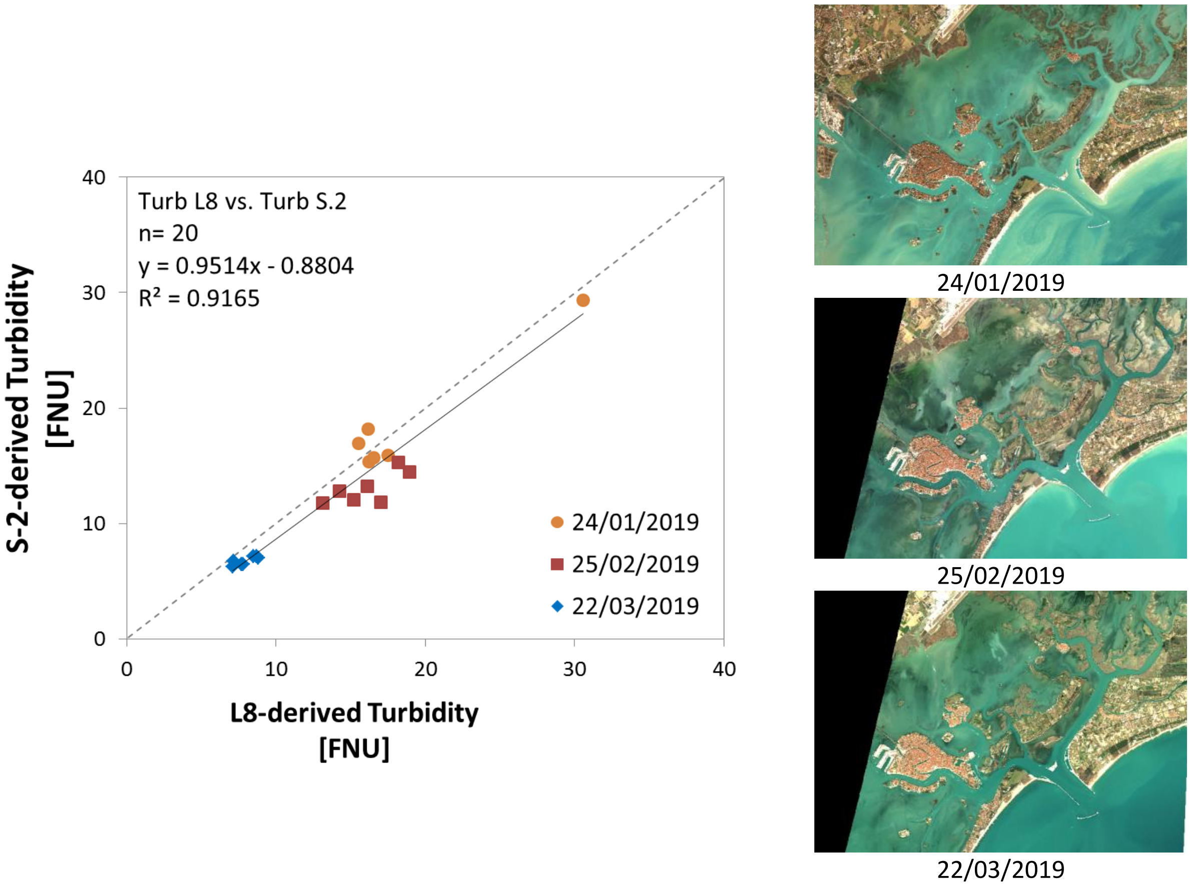

Figure 46 - The intercomparison of Turbidity products for near-simultaneous overpasses of L8 and S2 with the available matchups (3 field campaigns). On the left, the S2 pseudo true-color images, corresponding to the match-ups.

SPM

For the retrieval of SPM concentration, the ACOLITE-derived water leaving reflectance ($\rho_w(\lambda)$) were converted according to Nechad et al. (2010):

$$SPM\ [mg/L] = \frac{A^{\lambda}\rho_W(\lambda)}{1-\rho_W(\lambda)/C^{\lambda}} + B^{\lambda} \qquad \text{Equation 13}$$

where ρ_w refers to Sentinel-2 spectral band 4 (red) and to Landsat 8 spectral band 4 (red), and A, B and C are three wavelength-dependent calibration coefficients.

In situ collected SPM concentrations that are the result of the gravimetric analysis were used to assess the accuracy of T and SPM products derived from L8 and S2 imagery.

This project has received funding from the European Union's Horizon 2020 research and innovation programme under grant agreement No 776348

Similarily, a total of 105 match-ups (78 with S2 and 27 with L8, 20 of those with both S2 and L8) between satellite and *in situ* data collection were available by considering a maximum time difference of 1 h.

Figure 47 shows the scatter plots of the L8 and S2 derived estimates of SPM concentration versus *in situ* measurements: the correlations were statistically discrete with a coefficient of correlation r of 0.694 and 0.842, a coefficient of determination R^2 of 0.4826 and 0.7102, and a RMSE of 7.5 and 9.4, for the S2 and L8 derived SPM, respectively. See Table 29 for the complete statistics of fitting. Both L8 and S2 derived SPM products overestimate *in situ* SPM concentration. An example of the SPM map in the Lagoon of Venice is shown on Figure 48. Further improvements may involve parametrization of a robust region-specific relation between T and SPM concentration, as the optical properties of particulate matter vary seasonally, within and between regions, due to the variability in bulk particle composition. As reported on Figure 49, a weak correlation was also found between *in situ* turbidity and SPM concentration: this could be due to sampling and/or filtration issues.

This project has received funding from the European Union's Horizon 2020 research and innovation programme under grant agreement No 776348

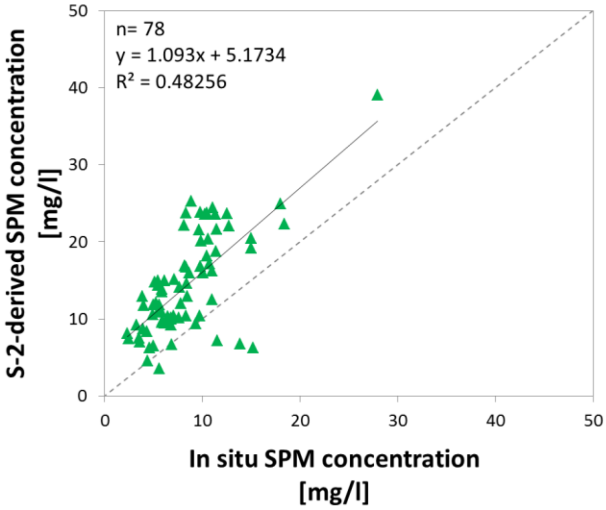

a)

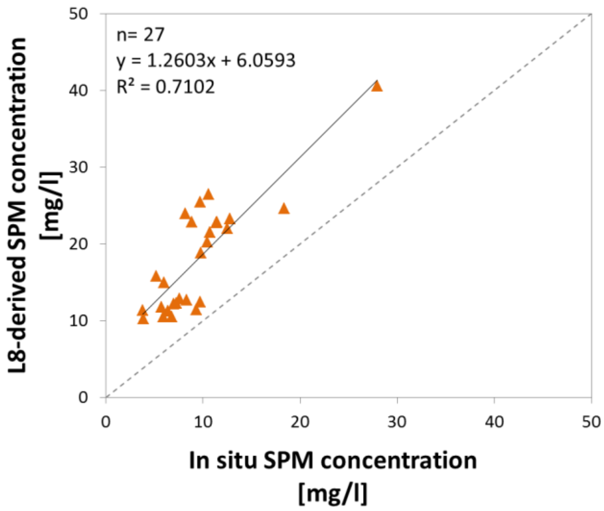

b)

Figure 47 - Validation scatterplot(s) for SPM CoastObs product, indicating R^2 and linear regression fit. a) Sentinel-2; b) Landsat 8. In both plots, the number of samples (n) and the 1:1 line is plotted as dotted lines.

Table 29 - Error metrics for SPM CoastObs products

Product	R^2	slope	RMSE	Bias	MAE	N
LV/SPM S2	0.4826	1.093	7.5 mg/l	5.9	6.5 mg/l	78
LV/SPM L8	0.7102	1.2603	9.4 mg/l	8.5	8.5 mg/l	27

This project has received funding from the European Union's Horizon 2020 research and innovation programme under grant agreement No 776348

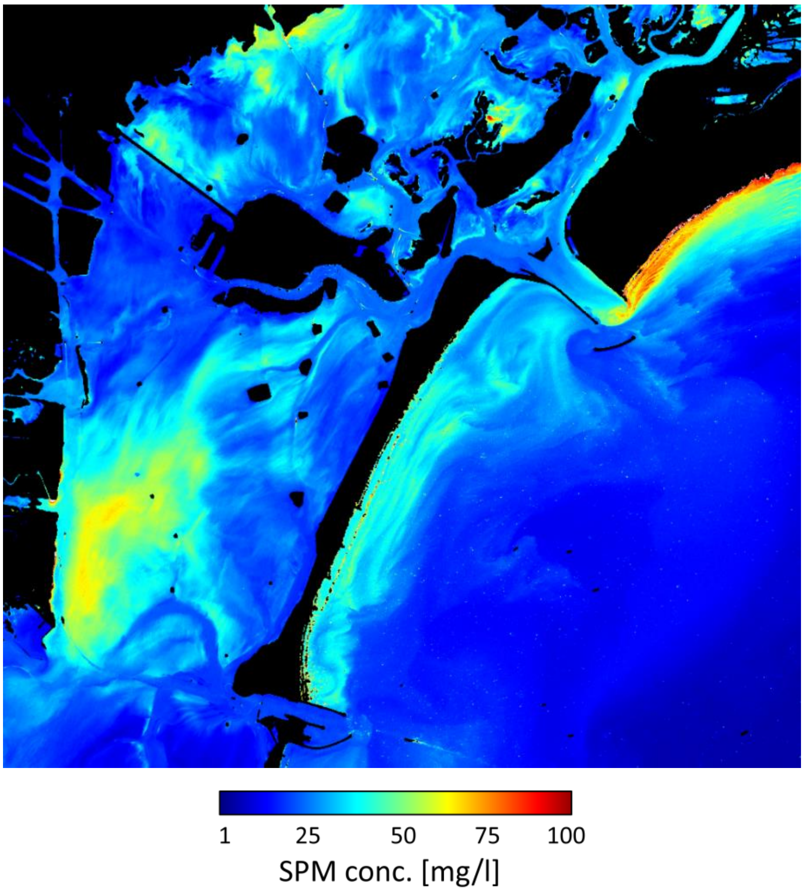

Figure 48 - Example map of SPM CoastObs product for S2 acquired on 20.03.2019

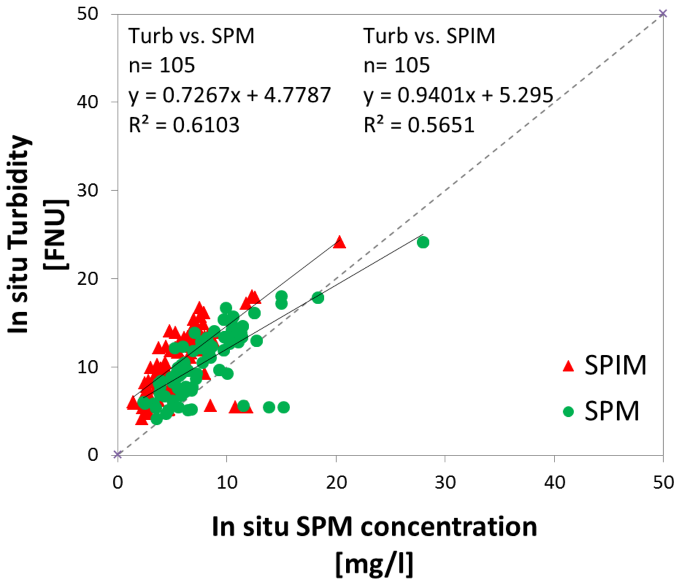

Figure 49 -The intercomparison of *in situ* Turbidity and SPM/SPIM concentration.

This project has received funding from the European Union's Horizon 2020 research and innovation programme under grant agreement No 776348

3.1.3.3 Netherlands

For Sentinel-3 data, SPM was derived using the Nechad et al. (2010) algorithm applied to the atmospherically corrected flagged satellite data. In addition, data from the automated measurement station at Eemshaven (Lat 53.47439 Lon 6.82173) owned by RWS were provided for a list of satellite matchup times. For each matchup, data at a 1-minute time interval were provided for a time window of 24 hours around the actual satellite overpass time. 71 dates were used as matchups for the period between 07/06/2016 to 18/01/2018. The observations closest in time to satellite overpasses were used to compare with the satellite results (Figure 50). We note that here SPM (suspended particulate matter) has the same meaning and unit with TSM (total suspended matter).

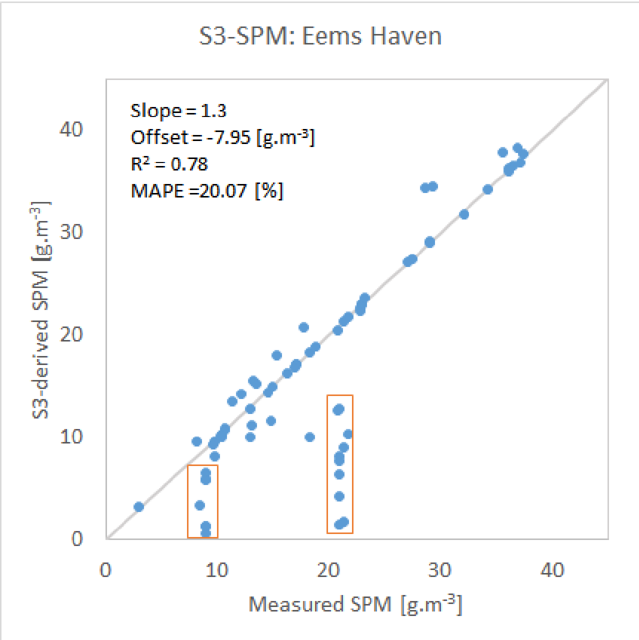

Figure 50 - Validation of S3-SPM products using the Eemshaven data set. Outliers are highlighted in red boxes but not excluded for the Goodness of Fit (GoF) parameter calculations

For Sentinel-2 data, Nechad et al. (2010) was applied to S2 imagery to derive SPM. The results of the validation are shown in Figure 51. For Eemshaven, the S2 derived SPM product are of high quality, except for one outlier highlighted in a red box. Removing this outlier results in the following Goodness of fit (Gof): slope = 1.09, offset = -1.35 [g.m^{-3}], R^2 = 0.97 and MAPE = 5.02[%].

This project has received funding from the European Union's Horizon 2020 research and innovation programme under grant agreement No 776348

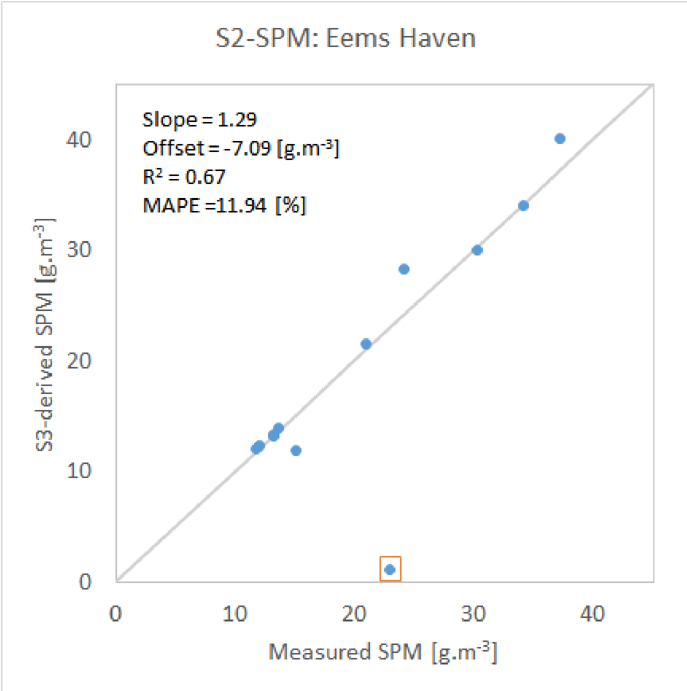

Figure 51 - Validation of S2 derived SPM concentrations using the Eemshaven data set. GoF parameters calculated without excluding the outlier in the red box.

A summary of the SPM validation results of S2 and S3 retrievals are shown in Table 30.

The importance of simultaneous sampling is illustrated nicely in Figure 51, where we see many SPM results very close to the 1:1 line with two small clusters where the measured values are almost the same and the satellite values are variable. We hypothesise that this is due to a malfunction of the *in situ* instrument.

Table 30 - Overall accuracy of S2 and S3 retrievals of SPM for the Netherlands

Product	R^2	slope	RMSE	MAPE (%)
S3	0.72	1.26	6.14	21.24
S2	0.33	2.72	16.86	45.05

This project has received funding from the European Union's Horizon 2020 research and innovation programme under grant agreement No 776348

3.1.3.4 Spain

Both simple empirical algorithms (Toming et al., 2017) and the analytical algorithm (Nechad et al., 2010; Novoa et al., 2017) were tested for TSM estimation in Ria de Vigo using the 2018 dataset. The tuned Nechad method for turbid waters worked best for Vigo S3 dataset (atmospherically corrected with C2RCC). The TSM aglorithm in Vigo can be expressed as follows:

$$TSM = 9418.39 * \frac{R_{rs}(665)}{1 - R_{rs}(665)/17.28} + 1.41 \quad \text{Equation 14}$$

Figure 52 presents the scatterplot of S3 modelled TSM versus *in situ* measured TSM at Vigo, and Table 31 indicates the error metrics. It shows that the Nechad analytical method generally performs well in Ria de Vigo where the water is relatively turbid and the average TSM concentration is about 6.7 mg/L. Note that further validation result will be added after the 2019 *in situ* measured TSM data in Vigo is available.

An example TSM map for the Ria de Vigo region is shown for 8th July in Figure 53, demonstrating the spatial pattern of the suspended particle distribution in this area.

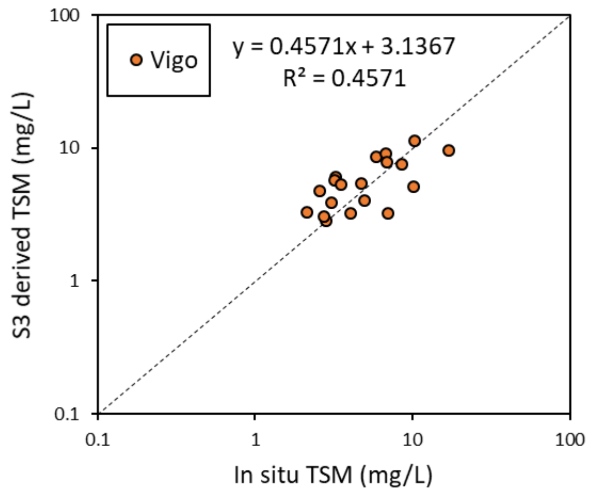

Figure 52 - Validation scatterplot(s) for TSM CoastObs product in Ria de Vigo, respectively, indicating R^2 and linear regression fit for the Vigo 2018 dataset

Table 31 - Error metrics for TSM CoastObs product in Ria de Vigo

Product	R^2	slope	$RMSE_{log}$	$Bias_{log}$	MAE_{log}	MAPE	N
Vigo TSM	0.46	0.46	0.18	0.03	0.03	37.1%	19

This project has received funding from the European Union's Horizon 2020 research and innovation programme under grant agreement No 776348

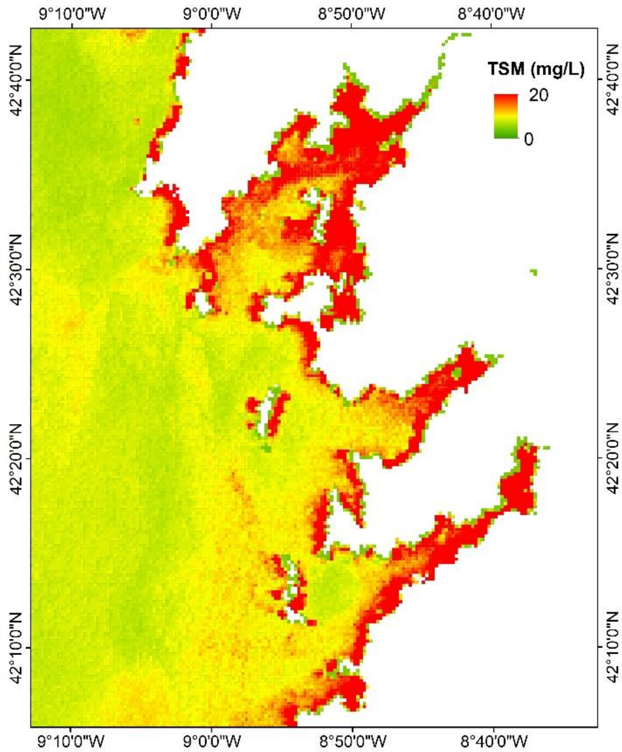

Figure 53 - Example map of TSM products for the Galician coastal waters, Spain (8 July 2018)

3.1.4 Sea surface temperature (SST)

3.1.4.1 Italy and Spain

Sea Surface Temperature (SST) data were acquired for use in the satellite primary production product (see Section 3.2.3). In the m2VGPM, P^B_{opt} (maximum C fixation rate) is modelled as a function of temperature. *In situ* temperatures were measured during the Venice and Vigo 2019 campaigns by either manual thermometer readings or using the temperature sensor on a C6 submersible fluorometer (Turner Designs).

Satellite SST data were downloaded on 27/9/2019 from the GHRSST dataset (https://www.ghrsst.org/ghrsst-data-services/products/). SST data were provided as a L4 gap-free gridded product, which is generated by combining complementary satellite and *in situ* observations within Optimal Interpolation systems. The advantage of the L4 dataset is increased temporal coverage, however the spatial resolution is coarse (1 km). GHRSST L4 data were converted from Kelvin to °C using the following conversion:

$$SST\ (K) - 273.15 = SST\ (°C) \qquad \text{Equation 15}$$

This project has received funding from the European Union's Horizon 2020 research and innovation programme under grant agreement No 776348

While there was a large amount of scatter in the relationship between satellite and *in situ* SST (Figure 54), the R^2 value for both datasets combined was high (0.962). However, we note this is driven by two distint clusters of data, therefore further validation over a broader range of temperatures would improve the validation for this parameter. Indeed, for the Netherlands dataset, the GHRSST data performed well over a wider range of temperatures (~5-20 °C; See Section 3.1.4.2). Error metrics for Vigo, Venice and the combined dataset are presented in Table 32.

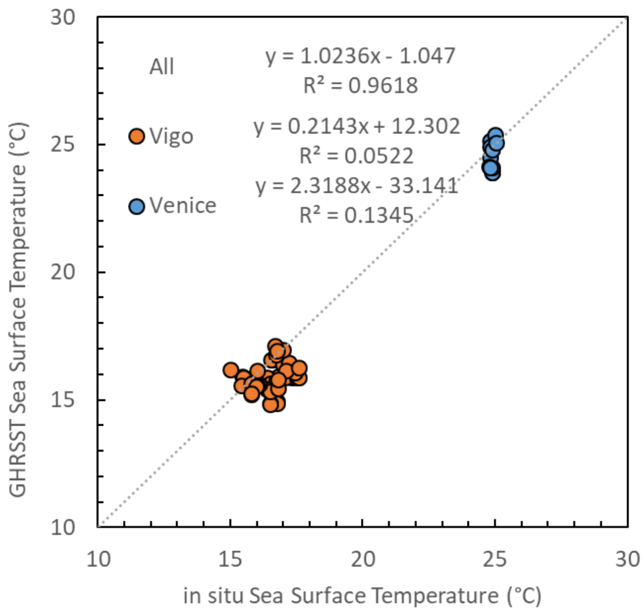

Figure 54 - Validation scatterplot for the Sea Surface Temperature (SST) product, indicating R² and linear regression fit

Table 32 - Error metrics for SST CoastObs product

Region	R^2	slope	$RMSE_{log}$	$Bias_{log}$	MAE_{log}	MAPE (%)	N
Venice Lagoon and Adriatic Sea, Italy	0.135	2.32	0.0105	0.00587	0.00866	1.97%	11
Ria de Vigo, Spain	0.052	0.214	0.0275	0.0186	0.0227	5.06%	39
All	0.962	1.02	0.0248	0.0158	0.0196	4.38%	50

This project has received funding from the European Union's Horizon 2020 research and innovation programme under grant agreement No 776348

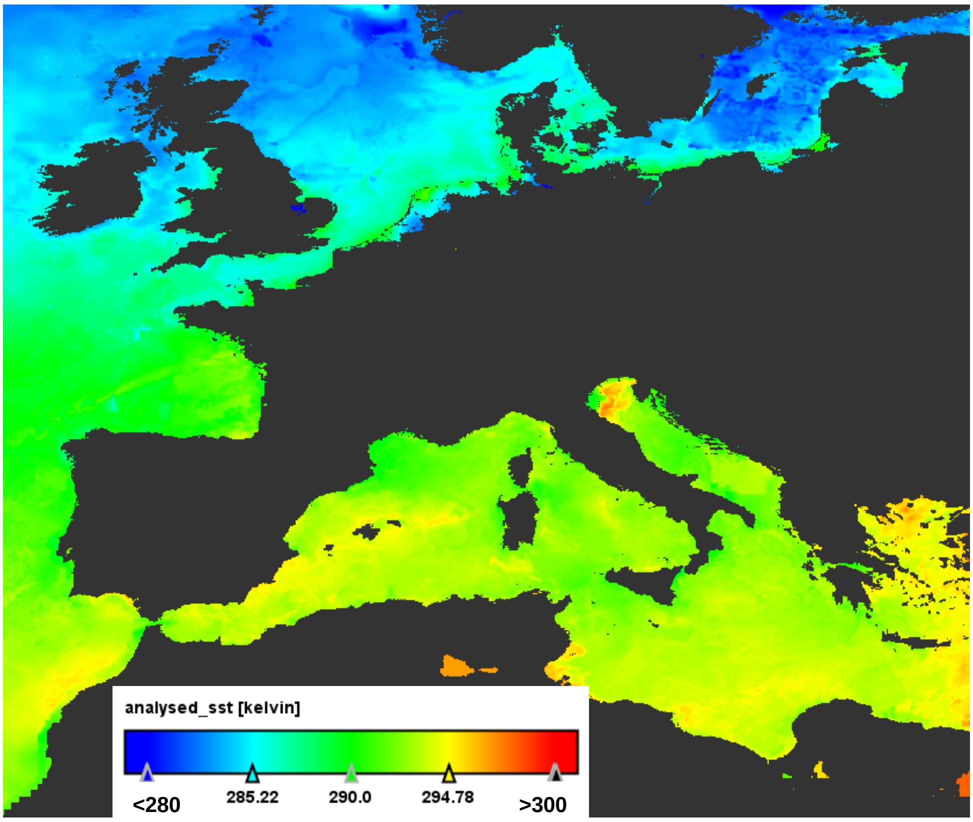

Figure 55 - Example map of GHRSST product for 03.06.2019 (SST, Kelvin)

3.1.4.2 Netherlands

GHRSST

For SST matchups, data were extracted at the location of the *in situ* station (Figure 56), except where those were very close to the shore, then the satellite data were retrieved from a point a short distance offshore. In such a way, 807 matchups were produced. The correlation between the *in situ* and satellite data is illustrated in Figure 57, the corresponding statistics are given in Table 33. Overall, the data correspond well, with a good correlation, low error and only very few outliers.

This project has received funding from the European Union's Horizon 2020 research and innovation programme under grant agreement No 776348

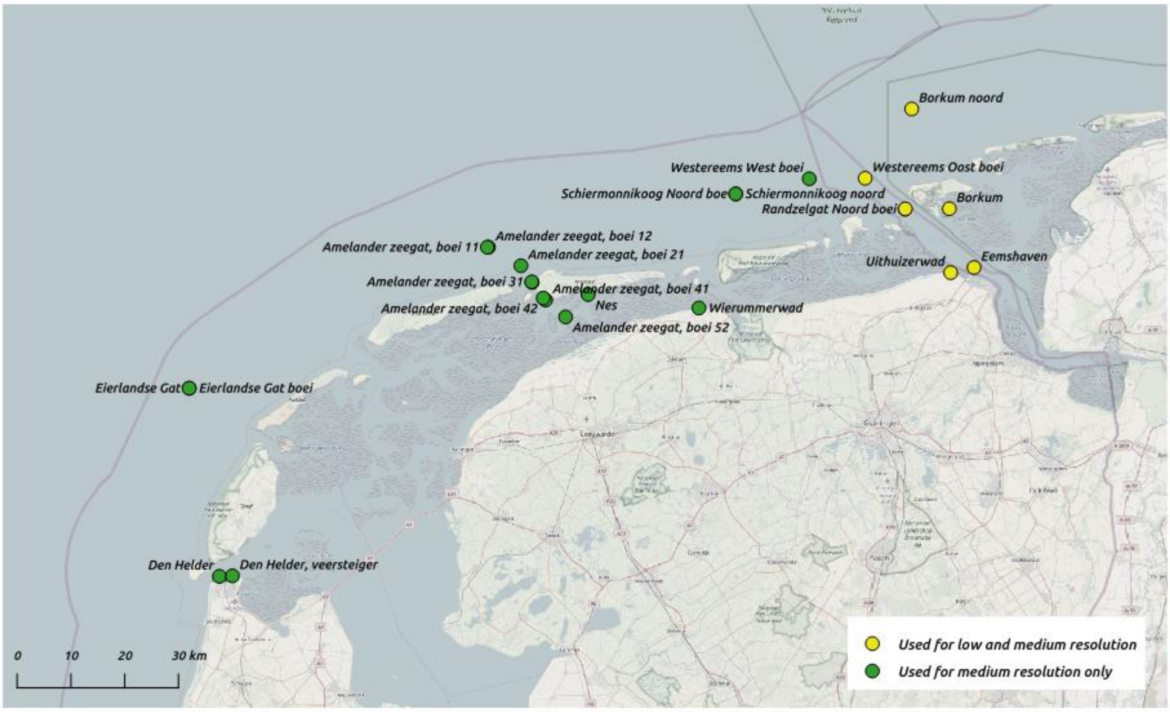

Figure 56 - Location of SST *in situ* stations in the Wadden Sea, Netherlands

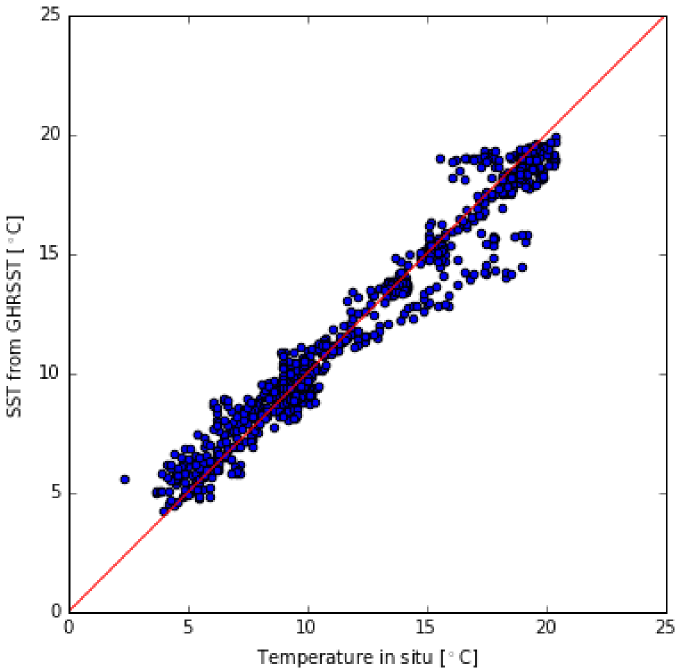

Figure 57 - Scatterplot *in situ* (daily median) versus GHRSST 1km data for SST for the 7 stations in the study area (2017)

Table 33 - Statistics for SST retrieval for GHRSST data in the Netherlands

Region	Satellite Dataset	R^2	slope	RMSE	N
Wadden Sea, Netherlands	GHRSST	0.96	0.91	1.01	807

Landsat 8

For matchups, data were extracted at the location of the *in situ* station, except where those were very close to the shore, then the satellite data were retrieved from a point a short distance offshore. The satellite-derived value was compared to the median of the 2-hour interval into which it fell. If there was no data for that interval, the closest time interval was used if it was of the same day. In such a way, 60 matchups were produced. The correlation between the *in situ* and EO data is illustrated in Figure 58, the corresponding statistics are given in Table 34. Overall, the data correspond well, with a good correlation, low error and only very few outliers. The correlation between medium resolution EO-based and *in situ* SST is quite good.

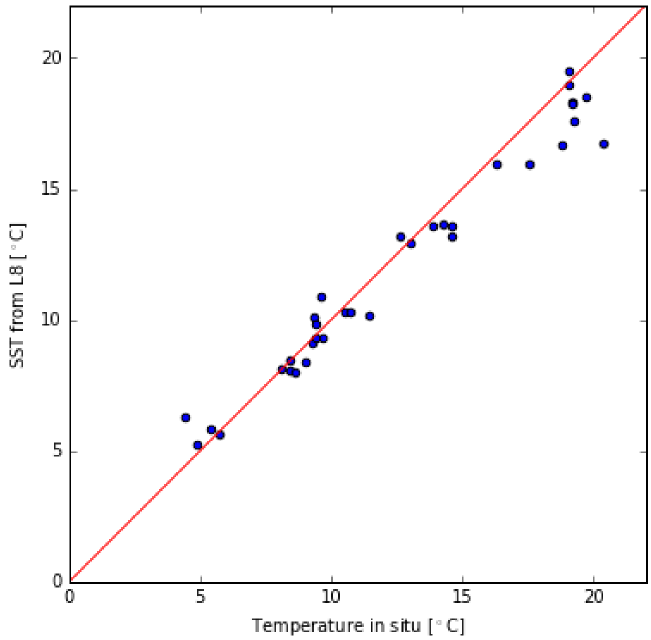

Figure 58 - Scatterplot *in situ* (2-hour median) versus Landsat8 data for SST for the 24 stations in the Wadden Sea (2017)

This project has received funding from the European Union's Horizon 2020 research and innovation programme under grant agreement No 776348

Table 34 - Statistics for SST retrieval for medium resolution data in the Netherlands

Region	Satellite Dataset	R^2	slope	RMSE	N
Wadden Sea, Netherlands	Landsat 8 SST	0.97	0.86	1.07	60

3.1.5 Euphotic Depth (Z_{eu})

3.1.5.1 Italy and Spain

Euphotic depth (Z_{eu}; m) is defined as the depth where photosynthetic available radiation (PAR) is 1% of its surface value (Kirk, 1994). This parameter is required for the CoastObs Primary Productivity model, and has been developed for use in the Italy and Spain regions for this purpose (see Section 3.2.3).

In situ PAR was measured using a Li-Cor spherical underwater quantum sensor (LI-193; 400-700 nm), and the PAR diffuse attenuation coefficient (K_d(PAR)) was calculated as a function of depth (z), PAR at depth z (PAR(z)), and PAR just below the surface (PAR(0^-)) as follows:

$$K_d(PAR) = \frac{-\ln\left(\frac{PAR(z)}{PAR(0^-)}\right)}{z} \qquad \text{Equation 16}$$

Thus, the natural logarithm of the measured downwelling irradiance was plotted against depth, and an estimate of Kd(PAR) was acquired as the resulting slope. Data where above water illumination conditions were variable were not used. *In situ* K_d(PAR) data were converted to euphotic depth using a conversion of 4.6/K_d(PAR) (Pierson et al., 2008).

Satellite Z_{eu} was derived from C2RCC atmospherically corrected Sentinel-3 data, where the algorithm was tuned using the Italy and Spain datasets from 2019 (Figure 59). The resulting algorithm for Z_{eu} from C2RCC S3 data is as follows:

$$Z_{eu}\ (\mathrm{m}) = 24.406 * exp\left(-0.564 * \left(\frac{Rrs(560)}{Rrs(490)}\right)\right) \qquad \text{Equation 17}$$

Validation errors for the Z_{eu} product from same-day matchups are presented in Table 35.

This project has received funding from the European Union's Horizon 2020 research and innovation programme under grant agreement No 776348

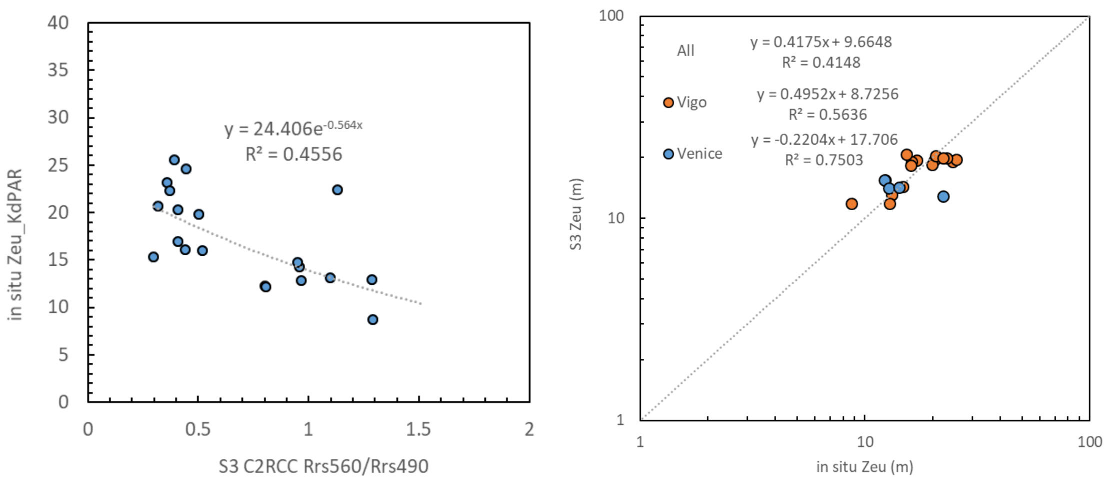

Figure 59 - Calibration scatterplot to tune Zeu as a functin oof R_{rs} (560)/ R_{rs} (490) (left) and validation scatterplot(s) for Euphotic Depth (Z_{eu}; m), indicating R^2 and linear regression fit (right).

Table 35 - Error metrics for Z_{eu} CoastObs product

Region	R^2	slope	$RMSE_{log}$	$Bias_{log}$	MAE_{log}	MAPE%	n
Venice Lagoon and Adriatic Sea, Italy	0.750	-0.220	0.127	-0.00189	0.0980	21.4%	5
Ria de Vigo, Spain	0.564	0.495	0.0739	0.000618	0.0602	14.1%	15
All	0.415	0.418	0.0900	-9.26 E-06	0.0697	16.0%	20

3.1.6 Daily irradiance (E_0)

3.1.6.1 Italy and Spain

Daily irradiance, E_0 (µmol m^{-2} s^{-1}), data were required for input for the Primary Productivity product (see Section 3.2.3). PAR(0$^+$) was measured *in situ* during the 2019 Italy and Spain campaigns using an above water quantum scalar Li-Cor sensor. The daily PAR curve was modelled using the incident() function in R (phytotools package), which models E_0 as a function of date, latitude, longitude, elevation, time zone, and mean daily PAR from all stations measured on each day. Daily E_0 was then calculated as the integral of the modelled daily daily PAR (mol m^{-2}).

Satellite E_0 data were acquired from the EUMETSAT data centre (https://archive.eumetsat.int/usc/) on 03/10/2019. These data are products derived from

This project has received funding from the European Union's Horizon 2020 research and innovation programme under grant agreement No 776348

SEVIRI onboard the geostationary satellite Meteosat (9/10/11), which is rather low spatial (5 km), but high temporal resolution (daily). Daily shortwave solar irradiance (SSI) that reaches the Earth's surface is calculcated from the 0.6 µm visible channel, where the daily value is integration of all the hourly values in the UT day. The product is provided on a 0.05° regular grid and expressed in W/m^2. The Meteosat SSI product was tuned to the 2019 E_0 daily modelled *in situ* dataset, as follows:

$$E_0 \text{ (mol m}^{-2}\text{)} = 0.2853 \times SSI^{1.06} \qquad \text{Equation 18}$$

The calibration and validation scatterplots for E_0 are presented in Figure 60, with error metrics shown in Table 36. Overall, there is a good correlation between the tuned E_0 product and *in situ* daily irradiance. However, we note as there are several stations collected on the same date, there are the same values for *in situ* E_0 for several stations; this results in the vertical lines on the validation plot. When only a single station for each date is compared, the coefficient of determination is slightly improved (R^2 = 0.6614).

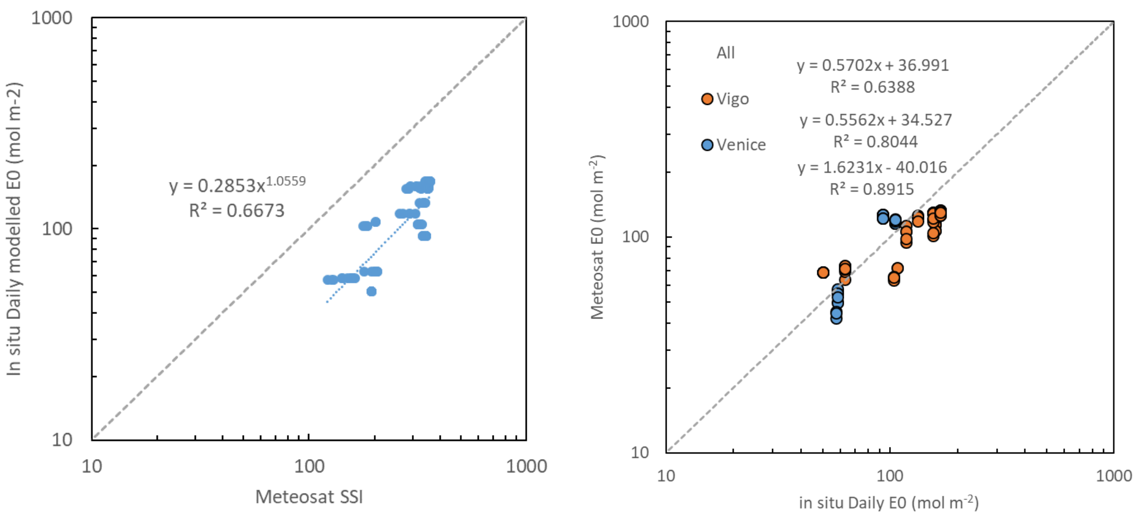

Figure 60 - Calibration scatterplot to tune Meteosat SSI as a function of *in situ* daily modelled irradiance, Eo, (left) and validation scatterplot for Eo, indicating R² and linear regression fit (right).

This project has received funding from the European Union's Horizon 2020 research and innovation programme under grant agreement No 776348

Table 36 – Error metrics for the daily PAR, E_o, CoastObs product

Region	R^2	slope	$RMSE_{log}$	$Bias_{log}$	MAE_{log}	MAPE (%)	N
Venice Lagoon and Adriatic Sea, Italy	0.892	1.62	0.0918	-0.0325	0.0800	19.7%	26
Ria de Vigo, Spain	0.804	0.556	0.115	0.0575	0.103	21.9%	58
All	0.639	0.570	0.109	0.0304	0.0961	21.2%	83

3.2 Innovative and Supplementary Products

3.2.1 Seagrass and Macro-Algae (SMA)

The data and method for this product was presented in the Seagrass and Macro-Algae Product Documentation (D3.3).

3.2.1.1 Inter-tidal seagrass

From *in situ* radiometric measurements collected in 2018 over a gradient from 0 to 100% of seagrass coverage, the normalized differential vegetation index (NDVI) was estimated. These measurements allowed us to calibrate a model to further estimate seagrass percent cover from S2 images (Figure 61). Such model was validated with independent datasets collected in 2019 over seagrass meadows dominated by Z. noltei in Bourgneuf Bay and Marenne Oleron, France.

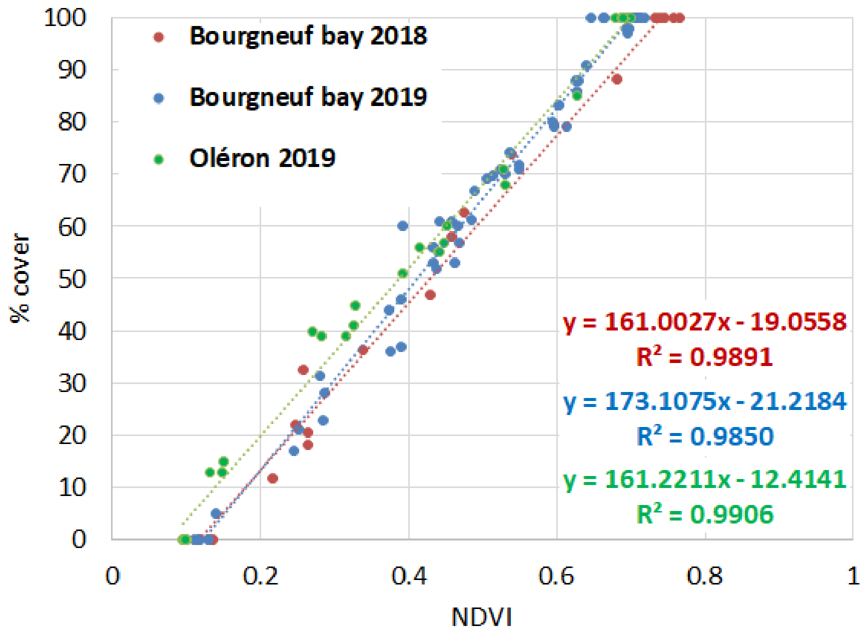

Figure 61 - Algorithm validation for seagrass percent cover as a function of NDVI. Red dots correspond to Bourgneuf bay dataset collected in 2018; blue dots correspond to Bourgneuf bay dataset collected in 2019; and green dots correspond to Marenne Oléron dataset collected in 2019.

Based on the analysis of the seasonal variability of the seagrass NDVI, the S2 image of the 14 September 2018 was found to best correspond to the seagrass annual maximum. The seagrass percent cover (SPC) was then estimated for this date using the NDVI – SPC relationship obtained in 2018 (see previous Figure). *In situ* SPC measurements were also available the same day, allowing us to validate SPC satellite retrieval (Figure 62). The matchup between *in situ* and S2-derived seagrass percent cover showed satisfactory results (Table 37). A limited dispersion was observed for low (< 20%) and high (> 80%) percent cover, likely due to the spatial homogeneity of patches of sparse and dense seagrass cover, respectively, at the scale of one S2 pixel. The patches of intermediate SPC were observed as being more spatially heterogeneous, thus explaining the higher variability in the matchups results. The validation stations used in this effort are showed in Figure 72 and an example of the seagrass percent cover produced in Bourgneuf Bay in 2018 is displayed in Figure 73.

This project has received funding from the European Union's Horizon 2020 research and innovation programme under grant agreement No 776348

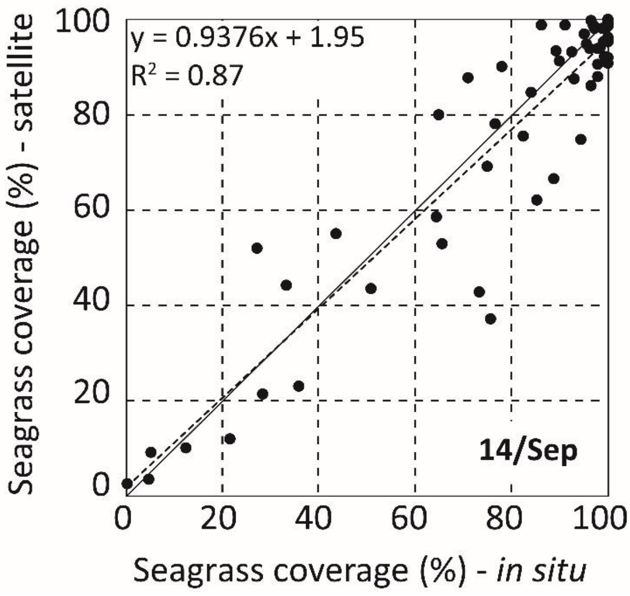

Figure 62 - Validation of seagrass percent cover product. It is shown R^2 and linear regression fit.

Table 37 - Error metrics for seagrass percent cover CoastObs product in intertidal areas

Product	R^2	slope	RMSE	Bias	MAE	N
Bourgneuf Bay	0.87	0.94	5.73	-1.51	2.73	56

This project has received funding from the European Union's Horizon 2020 research and innovation programme under grant agreement No 776348

Figure 63 - Spatial distribution of stations used to validate seagrass percent cover CoastObs product in 2018 over intertidal areas

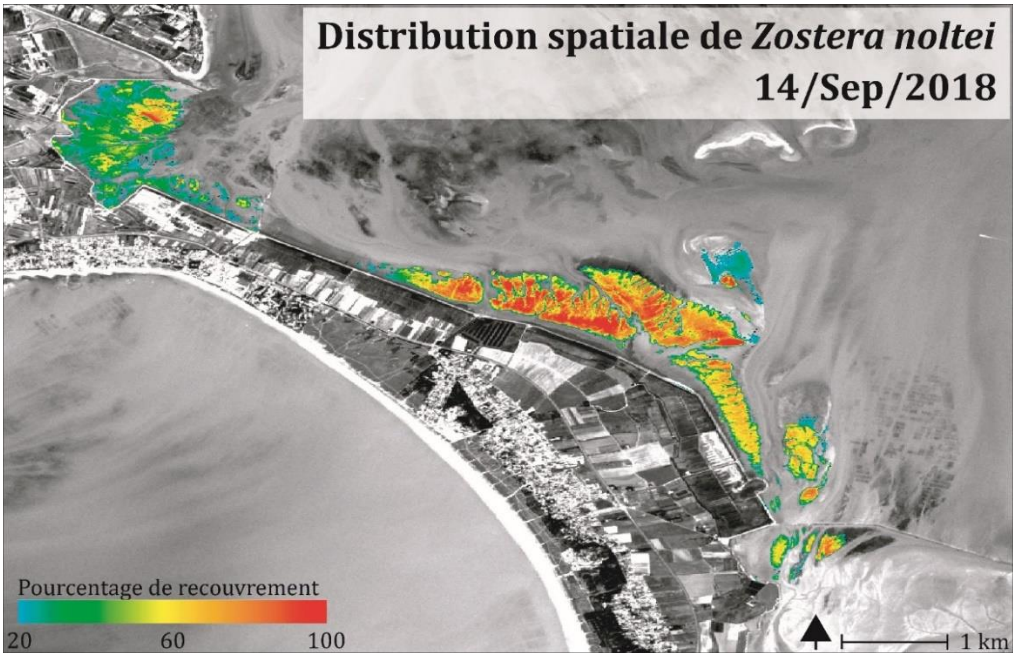

Figure 64 - Example map seagrass percent cover CoastObs product over intertidal areas in 2018

This project has received funding from the European Union's Horizon 2020 research and innovation programme under grant agreement No 776348

3.2.1.2 Sub-tidal seagrass

In situ radiometric measurements were collected in 38 stations on the 9 and 11 July 2019 in the Glénan Archipelago. In each station, radiometric information was collected along one transect, simultaneously with information about bottom coverage. At the end of the transect, bottom depth was measured. Those *in situ* measurements (both in hyperspectral resolution and degraded to the Sentinel2 bands) were used to evaluate the performance of the Shallow Water Semi-Analytical Model (SWAM, Wettle and Brando, 2006) algorithm (More details about SWAM can be found in the Deliverable D3.3 „Seagrass and Macro-Algae Product”). Because *in situ* radiometric samples were not submitted to uncertainties introduced by atmospheric effects, they allowed us to analyze ideal situations:

- from hyperspectral *in situ* measurements it was possible to evaluate limitations in the SWAM algorithm itself and caused by spectral proximity between macroalgae and seagrass reflectance curves, and
- from Sentinel2 simulated bands it was possible to evaluate the impact of lost in spectral resolution.

SWAM was also run in a Sentinel2 image acquired on the 06/Jul/2019 and previously corrected with POLYMER from atmospheric effects. This processing provided a more realistic situation, whose outputs were associated additionally to uncertainties introduced by the atmospheric correction and degradation to the spatial resolution in the Sentinel2 pixels. *In situ* environmental information of the bottom depth and substrate percent cover was collected over 210 stations in a dedicated campaign for validation, between 8 and 11 of July 2019 in the Glénan Archipelago and used to evaluate bottom percent cover products.

From SWAM outputs, we excluded all the stations where a substrate detectability index (SDI) lower than 5 was retrieved. Stations/pixels with SDI<5 did not include sufficient contribution from the bottom to the radiometric signal at surface, and this situation corresponded to sites comprising either substrate very dark and/or too deep. In general, for all SWAM products, when there were contrasted those derived from hyperspectral against from S2 simulated bands, it could be observed a similar performance between them indicating that the lost in spectral resolution was not the main factor driving uncertainties. Considering first bottom depth estimated from SWAM, it can be seen that the model was able to retrieve depths in the same range than *in situ* values, however with some dispersion of data (Figure 65 and Table 38). Depths retrieved from hyperspectral data showed a slope near 1, while reducing spectral resolution of inputs resulted in some underestimation in SWAM outputs.

This project has received funding from the European Union’s Horizon 2020 research and innovation programme under grant agreement No 776348

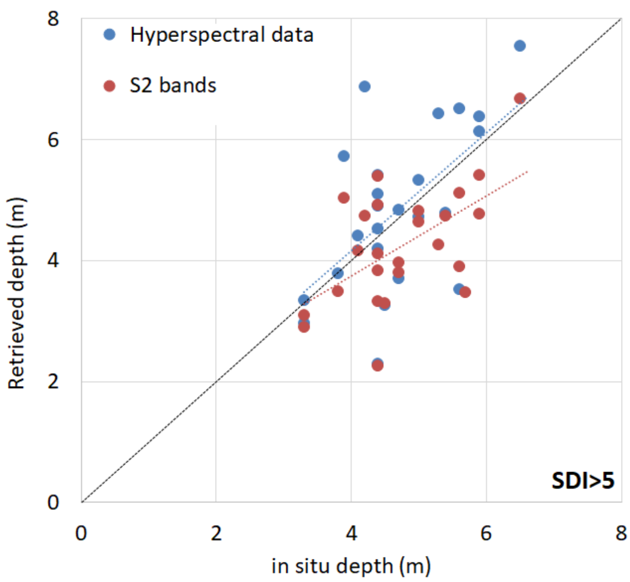

Figure 65 - Validation scatterplot for depth CoastObs product derived from *in situ* radiometric data, as hyperspectral data (blue dots) and simulated S2 bands

Table 38 – Error metrics for depth CoastObs product

Table 18						
Product	R^2	slope	RMSE	Bias	MAE	N
Depth derived from hyperspectral *in situ* radiometric data	0.35	0.97	1.10	0.15	0.80	24
Depth derived from S2 simulated *in situ* radiometric data	0.32	0.66	0.89	-0.44	0.72	24

This was the first attempt to validate SWAM outputs in subtidal seagrass meadows. Note that SWAM was developed originally to be run in coral reef environments, where spectral differences between coral and macroalgae classes are usually sufficient for their separability. Our results suggested that the spectral similarity among different vegetation types (e.g., seagrass, red algae, brown algae and green algae) immerse in the optically complex waters of the Glénan archipelago made differentiation between macroalgae and seagrass very difficult. This confusion between classes can explain high errors associated to SPC and MPC, even derived from *in situ* radiometric samples (Table 39 and Table 40). We decided to merge both classes (seagrass and macroalgae) into a class called Vegetation Percent Cover (VPC). For this new class, uncertainties were significatively decreased (Table 41) showing that a confusion between seagrass and macroalgae classes existed. In general, the model tended to overestimate vegetation percent cover while underestimating sand cover (Figure 66a and d and Figure 67a and d).

Besides model parameterizations themselves that can contribute to uncertainties in SWAM outputs and spectral closure of seagrass and macroalgae, we identified additional sources that can be pointed as responsible for uncertainties found here:

- even with careful pos-processing of *in situ* above-water radiometric measurements, they can still contain some surface and sky contamination. The processing of *in situ* samples over shallow waters is in the state-of-the-art and needs improvements by the ocean color community.
- In the analysis of underwater bottom pictures, we systematically found drifting algae and detached seagrass leaves. This moving vegetation is associated with high hydrodynamics in the area and with strong impacts of navigation activities during summer and is not possible to quantify and predict, i.e., our radiometric measurements and bottom characterization can correspond to slightly different scenarios as that vegetation is not fixed to the bottom and constant along the time of measurements.
- Sand substrate usually contain some associated microphytobenthos, not possible to quantify from underwater pictures. Pigments associated to those microalgae affect sand reflectance spectrum and could be also responsible for overestimation in vegetation proportions. New runs of SWAM will be performed using other reference spectrum for sand that can include also some maerl and microphytobenthos.

The 210 validation stations used in this effort in the Glénan Archipelago are displayed in Figure 38 and examples of the SPC, MPC and VPC products can be seen in Figure 69 to Figure 71. In a qualitative analysis of the spatial distribution of the SWAM products we could observe that SWAM outputs were spatially dependent. There are some portions of the image where SWAM was successfully able to retrieve the real bottom composition, mainly where substrates were dominated by one of the three classes (either seagrass, sand or macroalgae). These situations probably coincided with a shorter optical path length, either due to a shallower bottom and/or more stable conditions of the water column (*i.e.,* lower resuspension of the bottom and lower turbidity). Generally, uncertainties were higher when substrate presented mixed and patchy composition in deeper areas of the archipelago.

This project has received funding from the European Union's Horizon 2020 research and innovation programme under grant agreement No 776348

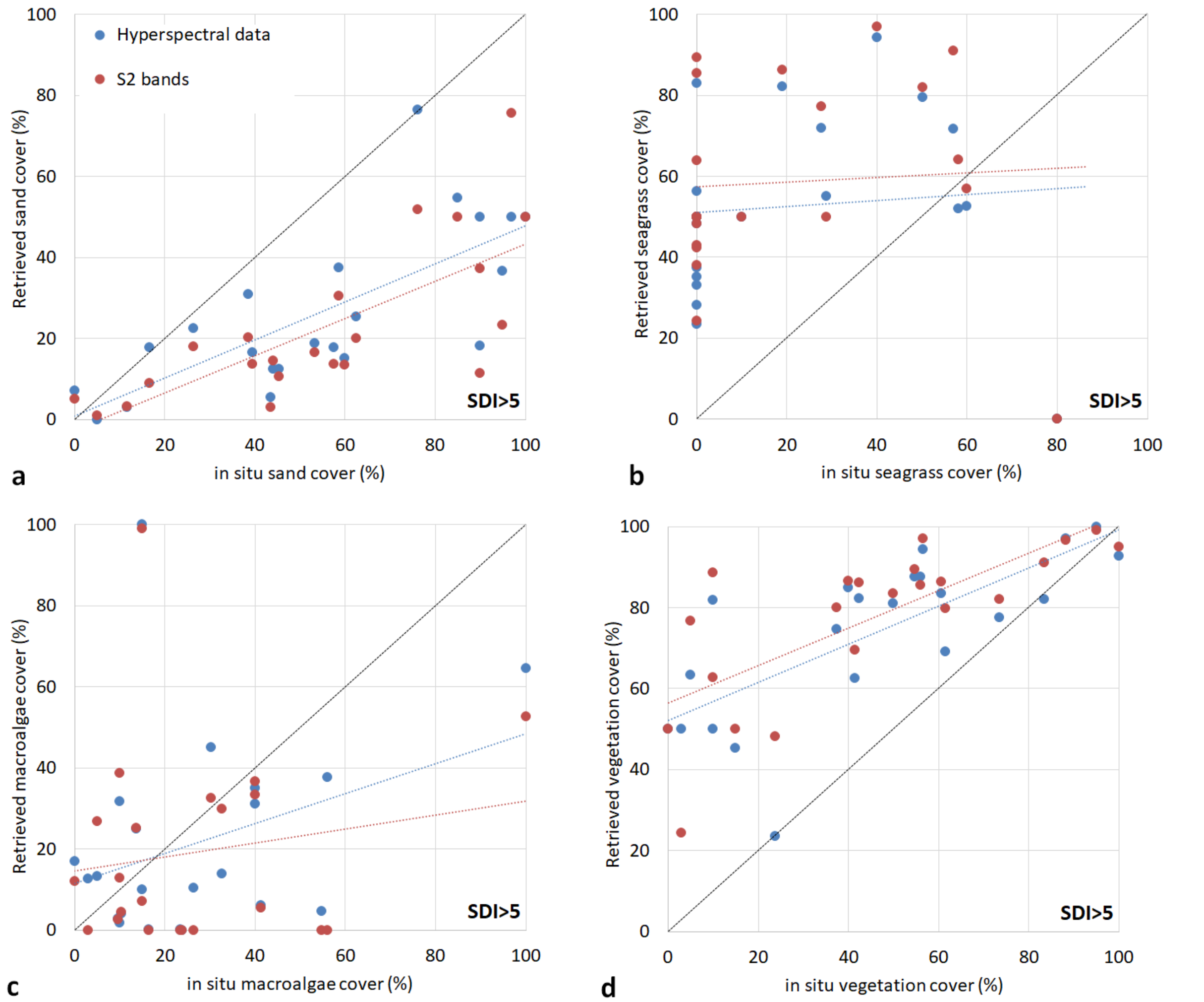

Figure 66 - Validation scatterplot for CoastObs product derived from *in situ* radiometric data in shallow waters, as hyperspectral data (blue dots) and simulated S2 bands: (a) sand percent cover, (b) seagrass percent cover (SPC), (c) macroalgae percent cover (MPC), and (d) vegetation percent cover (VPC).

This project has received funding from the European Union's Horizon 2020 research and innovation programme under grant agreement No 776348

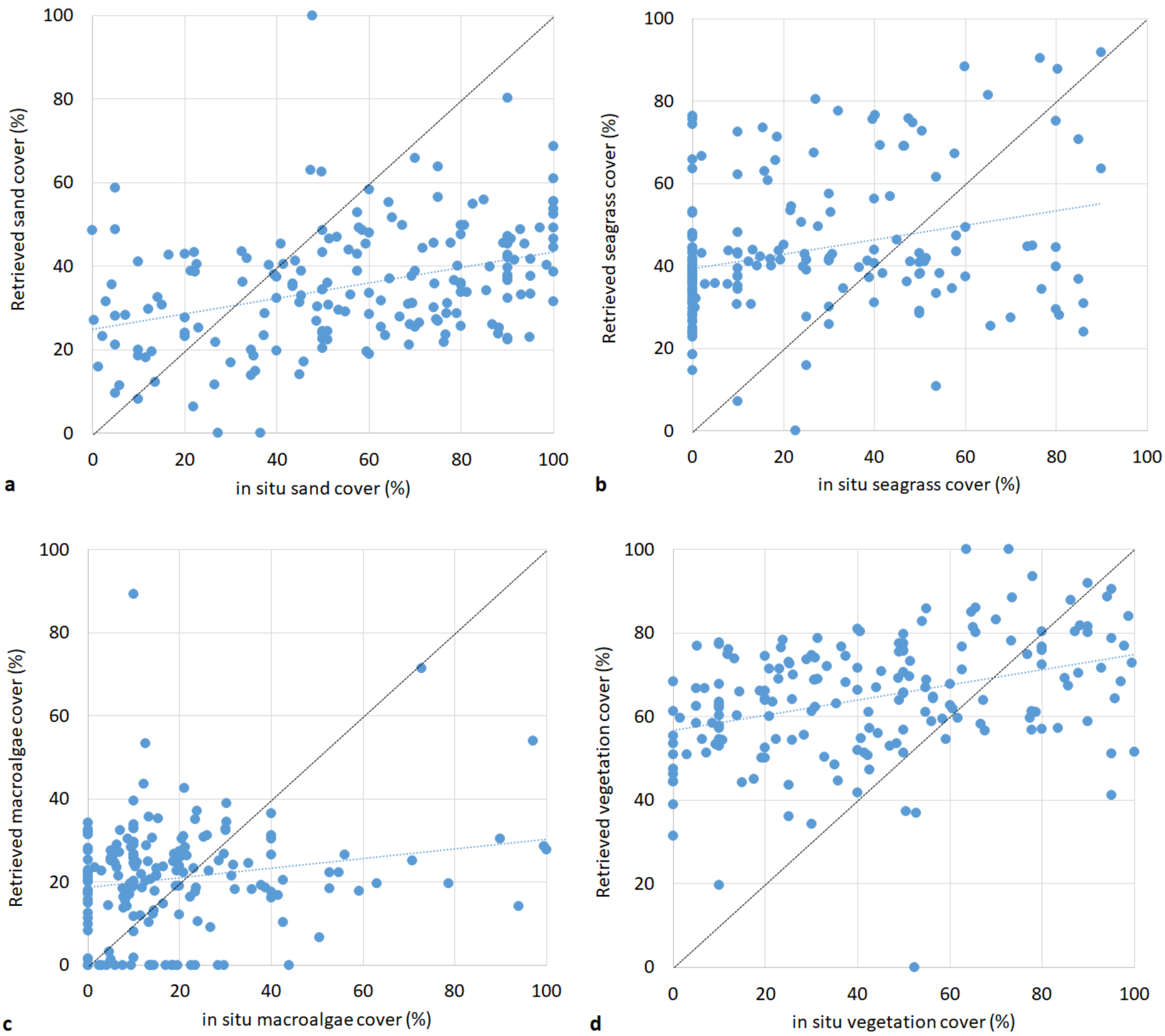

Figure 67 - Validation scatterplot for CoastObs product derived from Sentinel2 acquired on the 6/7/2019 in shallow waters: (a) sand percent cover, (b) seagrass percent cover (SPC), (c) macroalgae percent cover (MPC), and (d) vegetation percent cover (VPC).

This project has received funding from the European Union's Horizon 2020 research and innovation programme under grant agreement No 776348

Table 39 – Error metrics for seagrass percent cover (SPC) CoastObs product

Table 19						
Product	R^2	slope	RMSE	Bias	MAE	N
SPC derived from hyperspectral *in situ* radiometric data	0.01	0.07	46.9	32.89	41.38	22
SPC derived from S2 simulated *in situ* radiometric data	0.004	0.07	52.68	39.02	46.57	22
SPC derived from a S2 image	0.08	0.18	33.36	19.27	29.23	182

Table 40 - Error metrics for macroalgae percent cover (MPC) CoastObs product

Table 20						
Product	R^2	slope	RMSE	Bias	MAE	N
MPC derived from hyperspectral *in situ* radiometric data	0.37	0.12	27.70	-5.00	20.26	22
MPC derived from S2 simulated *in situ* radiometric data	0.03	0.17	31.33	-7.17	21.98	22
MPC derived from a S2 image	0.03	0.12	22.09	1.85	16.63	182

Table 41 - Error metrics for vegetation percent cover (VPC) CoastObs product

Table 21						
Product	R^2	slope	RMSE	Bias	MAE	N
VPC derived from hyperspectral *in situ* radiometric data	0.54	0.47	35.49	32.90	28.68	22
VPC derived from S2 simulated *in situ* radiometric data	0.54	0.46	38.82	31.85	32.31	22
VPC derived from a S2 image	0.14	0.18	34.52	20.81	29.01	182

This project has received funding from the European Union's Horizon 2020 research and innovation programme under grant agreement No 776348

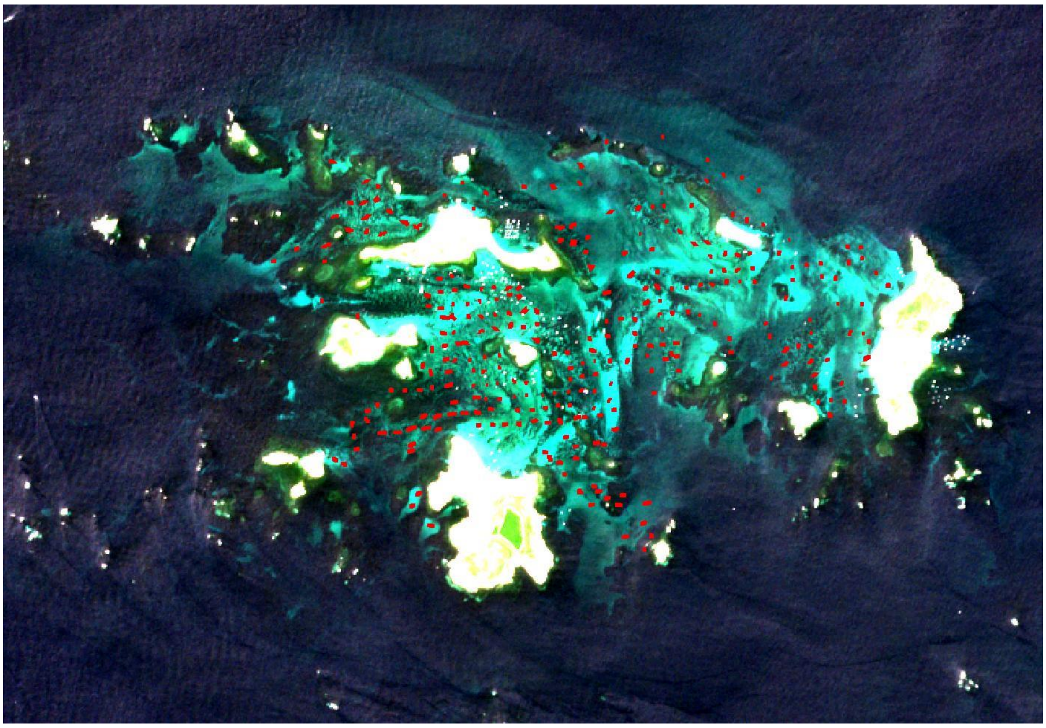

Figure 68 - Validation stations sampled in the Glénan Archipelago during July/2019

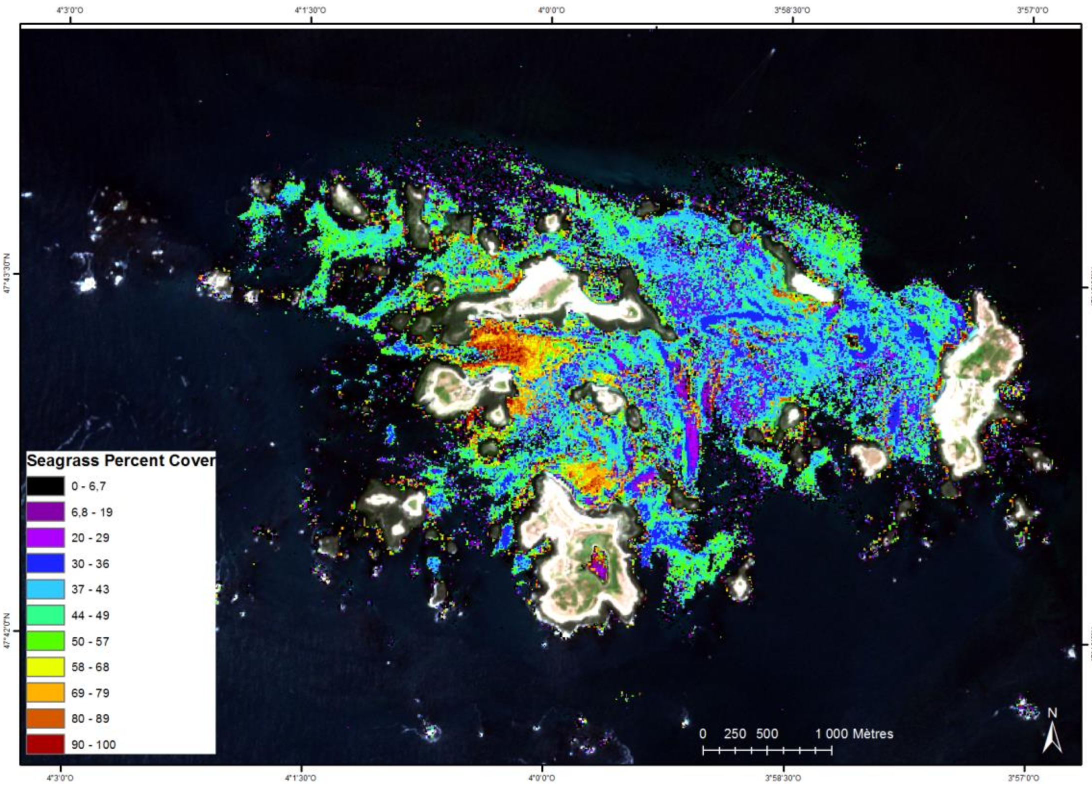

Figure 69 - Example map of seagrass percent cover CoastObs product for 06.07.2019

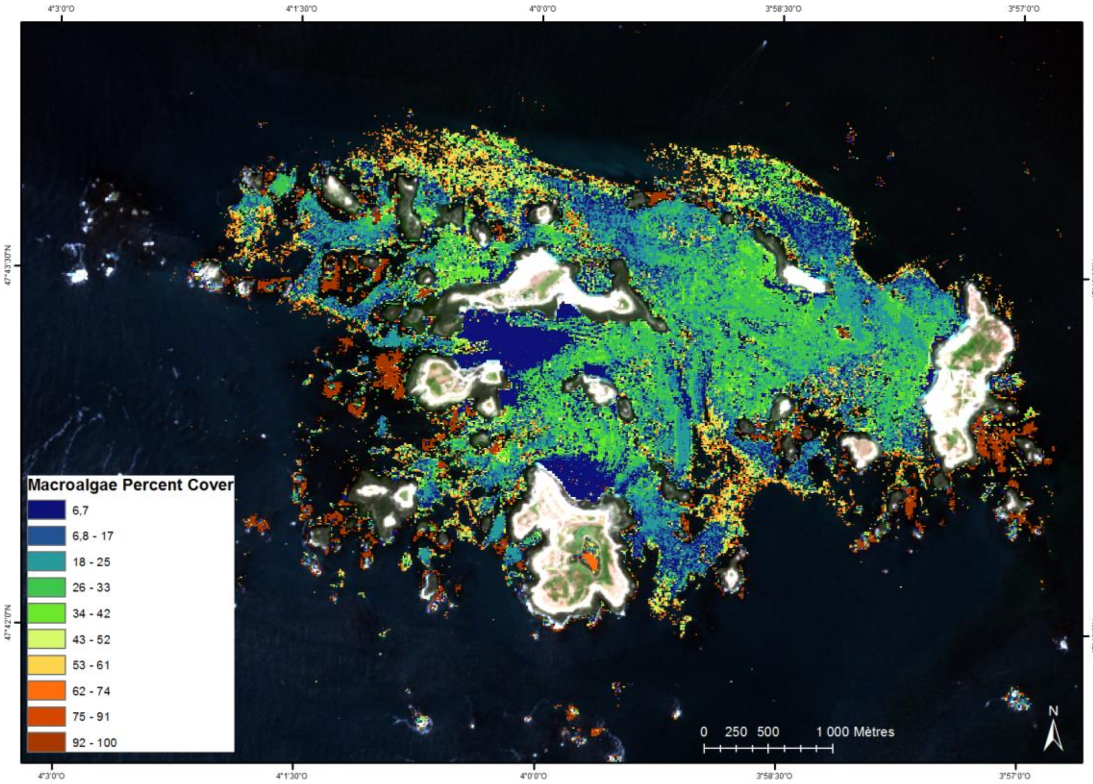

Figure 70 - Example map of macroalgae percent cover CoastObs product for 06.07.2019

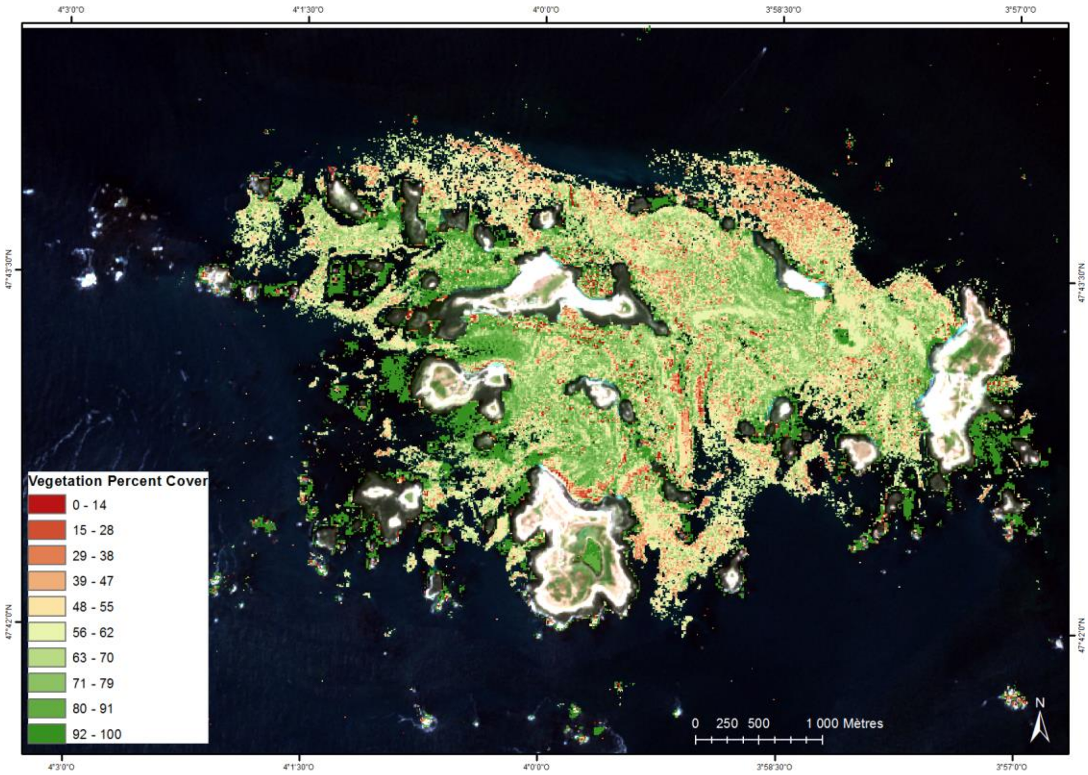

Figure 71 - Example map of vegetation percent cover CoastObs product for 06.07.2019

This project has received funding from the European Union's Horizon 2020 research and innovation programme under grant agreement No 776348

3.2.2 Phytoplankton Size Classes (PSC)

The validation results for two models for phytoplankton size class (PSC) are presented here. The first is an abundance-based approach, and this method is described in detail in the Phytoplankton Size Classes Product Documentation (**D 3.4**). The second is the absorption approach, and the datasets used, method and validation results are presented in full here.

3.2.2.1 Abundance approach

The Sentinel-3 model for Chl-*a* outperformas Sentinel-2 Chl-*a*, therefore the validation results for a PSC model for Sentinel-3 only is presented here. Furthermore, the best-performing Chl-*a* model for each region (Vigo and Venice; see Section 3.1.2) is carried forward for the abundance-based PSC model.

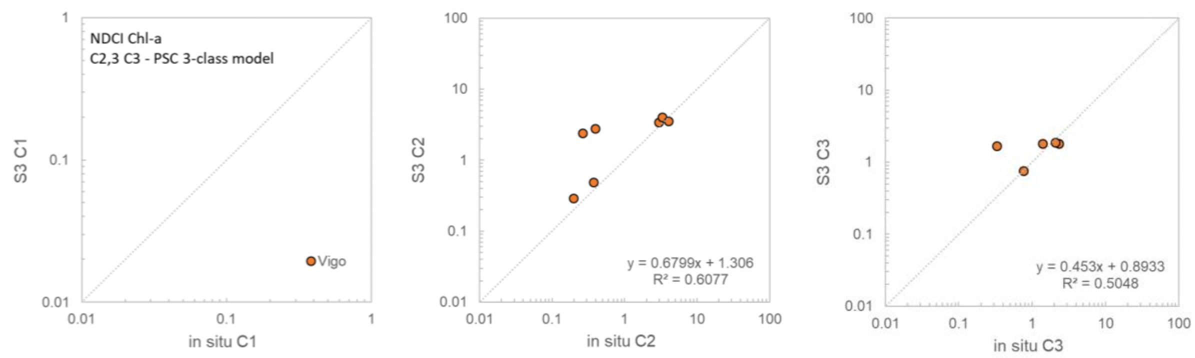

Figure 72 - Validation scatterplot(s) for the Abundance-based PSC CoastObs product, indicating R^2 and linear regression fit for the Vigo 2018 dataset for C1 (picophytoplankton), C2 (nanophytoplankton) and C3 (microphytoplankton) Chl-*a* (note there were no picoplankton present in 2018).

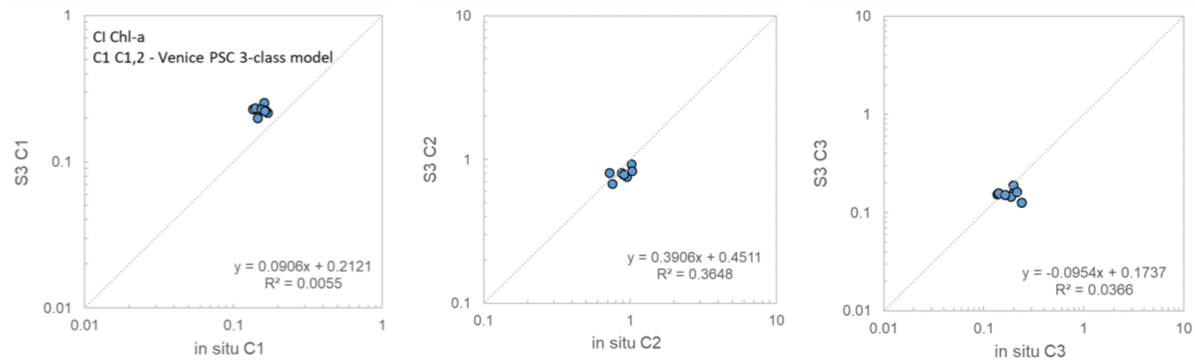

Figure 73 - Validation scatterplot(s) for the Abundance-based PSC CoastObs product, indicating R^2 and linear regression fit for the Venice 2018 dataset for C1 (picophytoplankton), C2 (nanophytoplankton) and C3 (microphytoplankton) Chl-*a*

This project has received funding from the European Union's Horizon 2020 research and innovation programme under grant agreement No 776348

The validation error metrics for the abundance-based PSC model are presented in Table 42. We note that further validation is required to increase confidence in this product, and the fractionated Chl-*a* samples from the Venice and Vigo 2019 campaigns will be used for this purpose once the HPLC laboratory analysis is complete (oustanding at the time of writing).

Overall, the abundance-based PSC model performs poorly for the pico-phytoplankton size class in both regions. In Vigo, this is likely due to the absence or extremely low abundance of pico-phytoplankton in the community, therefore there are at present no data to validate this product. However, we can expect that if the model works well for the two larger size classes, it will likely be reasonable for the pico-phytoplankton abundance. In contrast, the Venice model performs reasonably for the nano-phytoplankton size class, however poorly for the pico- and micro-phytoplankton size classes. This is likely simply due to the small validation dataset at this stage and low variability within the Venice 2018 dataset. Again, validation with 2019 data should help to improve this issue.

Table 42 – Error metrics for Abundance-based PSC CoastObs product

Region	Product	R^2	slope	$RMSE_{log}$	$Bias_{log}$	MAE_{log}	MAPE %	N
Ria de Vigo, Spain	Pico-phytoplankton (C1)*	NA	NA	NA	NA	NA	NA	0
	Nano-phytoplankton (C2)	0.608	0.680	0.494	-0.313	0.329	222	7
	Micro-phytoplankton (C3)	0.505	0.453	0.327	-0.134	0.197	96.0	5
Venice Lagoon and Adriatic Sea, Italy	Pico-phytoplankton (C1)	0.0055	0.0906	0.106	-0.0944	0.0944	25.1	8
	Nano-phytoplankton (C2)	0.365	0.391	0.0617	0.0447	0.0578	12.5	8
	Micro-phytoplankton (C3)	0.0366	-0.0954	0.0965	-0.0172	0.0769	18.3	8

* Note there were no pico-phytoplankton present in *in situ* samples for the Vigo 2018 dataset, therefore validation results cannot be presented at this time.

An example 3-class PSC map for the Vigo region is shown for 8th July in Figure 74, demonstrating the relative abundance of each size class (%).

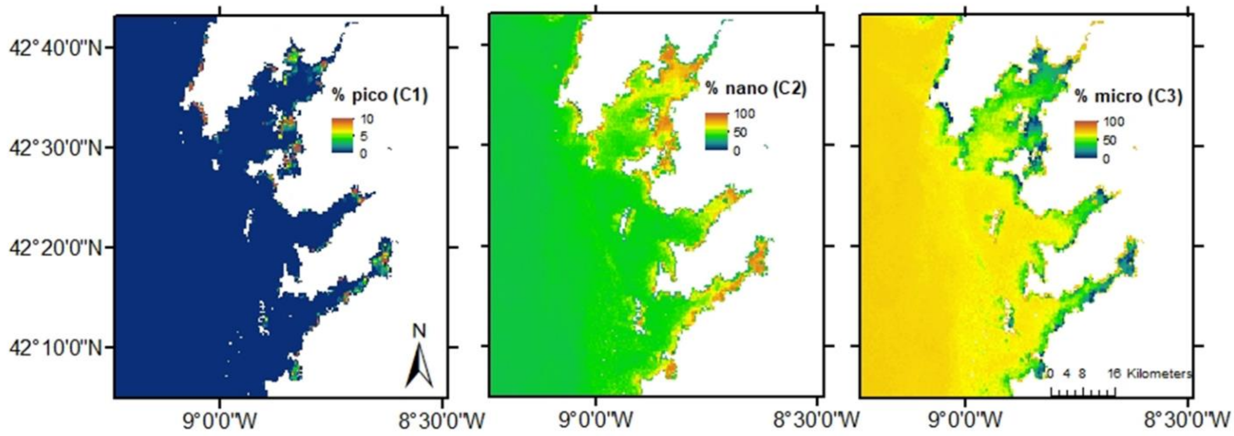

Figure 74 - Example map of Abundance-based 3-class PSC products for the Galician coastal waters, Spain (8 July 2018)

3.2.2.2 Absorption approach

3.2.2.2.1 Absorption-based PSC model

To determine the PSC with phytoplankton absorption, an analytical model (Roy et al., 2013) that computes the exponent of phytoplankton size spectrum from a_{ph} at the red peak (676 nm) was applied to retrieve the fractionated Chl-*a* in the three size class of phytoplankton. Here phytoplankton cells are treated as homogeneous spheres. For a ray of light passing through the center of the spherical cell, the dimensionless optical thickness ρ_c can be expressed as a function of the cell diameter *D* (in m) and the absorption coefficient of the cell material a_{cm}:

$$\rho_c = D \times a_{cm} \qquad \text{Equation 19}$$

Then, the dimensionless absorption efficiency Q_a of a cell defined as the ratio of the light absorbed by the cell to the light incident on it, can be expressed as a function of optical thickness ρ:

$$Q_a(\rho_c) = 1 + 2\frac{\exp(-\rho_c)}{\rho_c} + 2\frac{\exp(-\rho_c)-1}{\rho_c^2} \qquad \text{Equation 20}$$

and the Chlorophll-specific absorption coefficient of phytoplankton cells with diameter D, a^*_{chl} (λ, D), in suspension in water can be written as:

$$a^*_{chl}(\lambda, D) = \frac{3a^*_{ci}Q_a(\rho_c)}{2\rho_c} \qquad \text{Equation 21}$$

Here a^*_{ci} (in m^2/(mg Chl-*a*)) is the specific absorption coefficient of Chl-*a* inside a cell. Because Chl-*a* is known to be responsible for most of the phytoplankton absorption at the red peak around 676 nm, it is assumed that the contribution to total phytoplankton absorption from substances other than Chl-*a* is negligible at this wavelength (Roy et al., 2011). In other words, a^*_{ci} (676) $=a^*_{cm}$(676). In laboratory cultures, the magnitude of a^*_{ci} at 676 nm has been measured in the range of [0.025, 0.028] m^2/(mg Chl-*a*) (Roy et al., 2011). Considering the specific absorption coefficient of Chl-*a* (a^*_{ci}) should be maximum when it is unpackaged, usually the maximum of the reported values, say 0.028 m^2/(mg Chl-*a*), would be chosen in the implementation. And $a_{cm}\,(676) = a_{ci}\,(676) = \mathrm{a}^*_{ci} * c_i$, where the intercellular concentration of Chl-*a* c_i (in mg Chl-*a* /m^3) can be expressed as a function of cell size *D*:

$$\mathrm{c}_i = \mathrm{c}_0 \times \mathrm{D}^{-\mathrm{m}} \quad \text{Equation 22}$$

Hence, ρ_c(676) can be given by:

$$\rho_c(676) = \mathrm{a}^*_{ci}(676) \times c_0 \times D^{1-m} \quad \text{Equation 23}$$

where the parameters $c_0 = 3.9*10^6$ (mg Chl-*a* /$m^{2.94}$), m = 0.06 (dimensionless) estimated by Roy et al. (2011) based on the numerical relationship between the cell volume and the concentration of Chl-*a* per cell.

And assuming the size distribution of phytoplankton follows the power law, the differential number concentration N of phytoplankton cells per unit volume of seawater with a particle diameter of D can be given by:

$$\mathrm{N(D)} = kD^{-\xi} \quad \text{Equation 24}$$

Where ξ is the exponent of the phytoplankton size spectrum, *k* is a constant. Hence, the total number (N) of cells per unit volume of seawater within a given diameter range can be calculated by integrating the above equation in the diameter range [D_{min}, D_{max}]:

$$\mathrm{N} = \int_{D_{min}}^{D_{max}} [(kD^{-\xi})]\, dD = k\,\frac{D_{max}^{1-\xi} - D_{min}^{1-\xi}}{1-\xi} \quad \text{Equation 25}$$

The total volume (V) of particles within the same diameter range can be calculated as follows:

$$\mathrm{V} = \int_{D_{min}}^{D_{max}} [(\frac{\pi}{6} D^3)(kD^{-\xi})]\, dD = (\frac{\pi}{6} k)\,\frac{D_{max}^{4-\xi} - D_{min}^{4-\xi}}{4-\xi} \quad \text{Equation 26}$$

Hence, the concentration of Chl-*a*, B (mg/m3), of the population within the diameter range [D_{min}, D_{max}] can be expressed as follows:

$$\mathrm{B} = \int_{D_{min}}^{D_{max}} [(\frac{\pi}{6} D^3)(\mathrm{c}_0 \mathrm{D}^{-\mathrm{m}})(kD^{-\xi})]\, dD = (\frac{\pi}{6} k c_0)\,\frac{D_{max}^{4-\xi-m} - D_{min}^{4-\xi-m}}{4-\xi-m} \quad \text{Equation 27}$$

The absorption coefficient of phytoplankton (assuming Chl-*a* is the only absorbing pigment) at 676 nm, a_{chl}(676), is the product of the concentration of Chl-*a*, B mg/m^3, and the Chl-*a* specific absorption a^*_{chl} (λ) (in m^2/mg):

$$a_{chl}(\lambda) = a^*_{chl}(\lambda) \times B \quad \text{Equation 28}$$

This project has received funding from the European Union's Horizon 2020 research and innovation programme under grant agreement No 776348

Then the total absorption by Chl-*a* at 676 nm due to the phytoplankton cells in the diameter range [D_{min}, D_{max}] can be derived as follows:

$$a_{chl}(676) = \int_{D_{min}}^{D_{max}} [\left(\frac{\pi}{6} D^3\right) (\mathrm{c_0 D^{-m}})\left(kD^{-\xi}\right) \times a^*_{chl}(676, D)]\, dD \quad \text{Equation 29}$$

Thus, $a^*_{chl}(676)$ can be derived as follows:

$$a^*_{chl}(676) = \frac{a_{chl}(676)}{B} = \frac{4-\xi-m}{D_{max}^{4-\xi-m} - D_{min}^{4-\xi-m}} \int_{D_{min}}^{D_{max}} [\left(D^{3-\xi-m}\right) \times a^*_{chl}(676, D)]\, dD \quad \text{Equation 30}$$

where $a^*_{chl}(676, D)$ can be calculated using Qa calculated.

On the other hand, $a^*_{chl}(676)$ can be derived from the absorption coefficient of phytoplankton $a_{chl}(\lambda)$ and the derived concentration of Chl-*a* B using Eq. (11), hence ξ can be calculated with a given $a^*_{chl}(676)$.

Once the exponent of the phytoplankton size spectrum ξ is derived, it can be used to calculate the fractions of Chl-*a* in any given diameter range. For instance, the ranges of cell diameters for picoplankton, nanoplankton, microplankton are given by [D_0, D_1], [D_1, D_2], [D_2, D_3], then the Chl-*a* fractions of the three size classes can be derived as follows:

$$F_p = \frac{Pico\ Chla}{Total\ Chla} = \frac{D_1^{4-\xi-m} - D_0^{4-\xi-m}}{D_3^{4-\xi-m} - D_0^{4-\xi-m}}$$

$$F_n = \frac{Nano\ Chla}{Total\ Chla} = \frac{D_2^{4-\xi-m} - D_1^{4-\xi-m}}{D_3^{4-\xi-m} - D_0^{4-\xi-m}}$$

$$F_m = \frac{Micro\ Chla}{Total\ Chla} = \frac{D_3^{4-\xi-m} - D_2^{4-\xi-m}}{D_3^{4-\xi-m} - D_0^{4-\xi-m}} \quad \text{Equation 31}$$

3.2.2.2.2 Retreiving a_{ph} from remote-sensing reflectance

Whereas the absorption-based PSC model need to be applied to satellite data, one critical step before the implimentation is to obtain a_{ph} from satellite data. a_{ph} can be derived from R_{rs} using different IOP inversion algorithms (IOCCG, 2006).

The Quasi-Analytical Algorithm version 6 (QAAv6) (Lee, 2014; Lee et al., 2002) was first tested for a_{ph} derivation for datasets collected at Venice lagoon and Ria de Vigo in 2018. The *in situ* R_{rs} measured by TriOS was fed into QAAv6 to assess the algorithm performance at 443 and 676 nm. Results showed the QAAv6 algorithm performs generally well in retrieving a_{ph} for both Venice lagoon and Ria de Vigo with MAPE less than or around 30%. However, the performance of the QAAv6 algorithm was poor when apply it to S3-derived R_{rs} for the derivation of a_{ph}. That's probably because the QAA algorithm highly relies on R_{rs} at blue bands (i.e 412, 443 nm), but the atmospheric correction methods always bring large uncertainties for bands at this region.

This project has received funding from the European Union's Horizon 2020 research and innovation programme under grant agreement No 776348

Then an alternative IOP inversion algorithm suggested by Gons et al. (2005, 2008) was tested and optimized to fit the datasets in Venice and Vigo. This algorithm starts with an approximation of remote-sensing reflectance as follows:

$$R_{rs}(0,\lambda) = \frac{C\times b_b(\lambda)}{a(\lambda)+b_b(\lambda)} \quad \text{Equation 32}$$

where C is the scaling factor depending on incident light. The ratio of R_{rs} at near-infrared band (i.e. 709 nm) to the red band (i.e. 676 nm) has been proved to be useful for retrieval of Chl-*a* and a_{ph} in relatively turbid and eutrophic waters. The reflectance ratio R for 709 nm and 676 nm can be expressed as follows:

$$R = \frac{b_b(709)}{b_b(676)} \times \frac{a(676)+b_b(676)}{a(709)+b_b(709)} \quad \text{Equation 33}$$

Absorption can be partitioned among phytoplankton (a_{ph}), water (a_w), detrital and gelbstoff (a_{dg}). Two simplifications are then made (i) for λ = 676 nm, absorption other than by Chl-*a* and water is negligible; (ii) for λ = 709 nm, absorption other than by water is negligible. Hence, $a_{ph}(676)$ can be written as follows:

$$a_{ph}(676) = \frac{b_b(676)}{b_b(709)} \times R \times \left(a_w(709) + b_b(709)\right) - b_b(676) - a_w(676) \quad \text{Equation 34}$$

Here Gons et al. (2005, 2008) takes b_b as wavelength independent and it can be estimated using the band centered at 754 nm:

$$b_b = \frac{1.61\, R_{rs}(754)}{0.082-0.6R_{rs}(754)} \quad \text{Equation 35}$$

So Eq. (17) can be further simplified:

$$a_{ph}(676) = R \times (a_w(709) + b_b) - b_b - a_w(676) \quad \text{Equation 36}$$

However, with these simplifications, the derived $a_{ph}(676)$ can often be negative for less eutrophic and turbid waters. That's because (i) the red Chl-*a* absorption peak may be overwhelmed by water absorption when the contribution of Chl-*a* is not significant; (ii) the b_b is not wavelength independent for less turbid waters. Therefore, an empirical scale factor *f* is put into the equation to compensate the spectral shape of b_b and amplify the Chl-*a* signal, so that $a_{ph}(676)$ can be derived using the Gons modification algorithm (we term it as Gons-m hereafter):

$$a_{ph}(676) = f \times R \times (a_w(709) + b_b) - b_b - a_w(676) \quad \text{Equation 37}$$

Here the dimensionless scale factor *f* = 1.3, which is derived by fitting into the S3 datasets in Venice and Vigo. More work will be done in the future to justify this scale factor.

3.2.2.2.3 Performance of CoastObs absorption-based PSC model

The Gons-m algorithm was applied to the S3 R_{rs} datasets (produced by C2RCC processor) at Venice and Vigo for the derivation of a_{ph}. Lab measured a_{ph} from Venice and Vigo collected in 2018 was determined by the spectrophotometric method with IS-mode (IOCCG, 2018) and was then used for validation. Figure 75 presents the scatterplots of the satellite modelled a_{ph} versus lab measured a_{ph} and indicates the improved performance for the derivation of $a_{ph}(443)$ and $a_{ph}(674)$ using the Gons-m algorithm (MAPE < 40%, R^2 = 0.38-0.50). Note that the $a_{ph}(443)$ were calculated from Gons-m derived $a_{ph}(674)$ using the empirical model (Lee et al., 1998) tuned by the Venice and Vigo *in situ* datasets respectively.

For the PSC fraction model, the above-mentioned $a_{ph}(674)$ was input. The other model input parameter, total Chl-*a* concentration, was derived using the optimized CI and NDCI models for Venice and Vigo respectively. The model derived Chl-*a* fractions in the three phytoplankton size class are shown in Figure 76 - Validation scatterplots of CoastObs absorption-based PSC products in Ria de Vigo and Venice Lagoon. (a) Pico-phytoplankton Chl-a, (b) Nano-phytoplankton Chl-a, (c) Micro-phytoplankton Chl-a.Figure 76. Table 43 presents the error metrics for absorption-based PSC CoastObs product. It indicates good agreements between the model derived and *in situ* measured values, particularly for nano-phytoplankton and pico-phytoplankton (MAPE < 41%). The overestimation of micro-phytoplankton Chl-*a* in Venice is probably because the lack of micro-phytoplankton in the studied area, but this analytical PSC model assumes the size distribution of phytoplankton follows the power law in the range of 0.2-50 µm. Further observations and studies are expected to improve the phytoplankton size distribution model. We note that the fractionated Chl-*a* and a_{ph} samples collected in 2019 will be further used to validate the models used here when the HPLC analysis results are available.

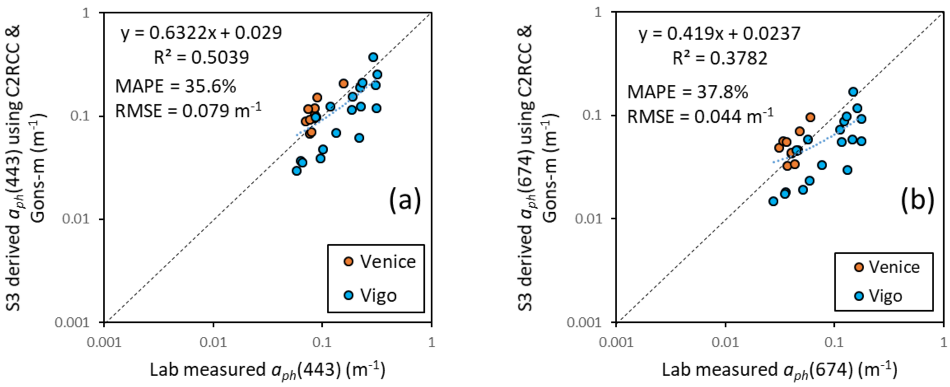

Figure 75 - Validation scatterplots of S3 derived a_{ph} using C2RCC & Gons-m algorithm, indicating the R^2 and linear fit for the Venice and Vigo 2018 datasets. (a) $a_{ph}(443)$, (b) $a_{ph}(674)$.

This project has received funding from the European Union's Horizon 2020 research and innovation programme under grant agreement No 776348

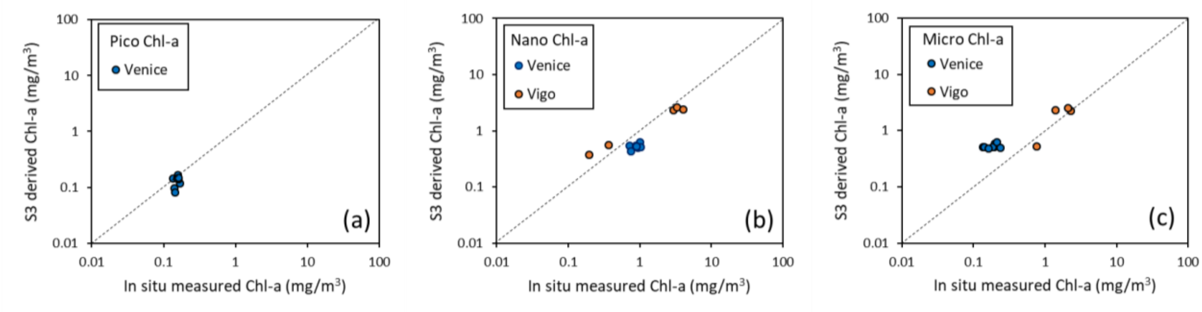

Figure 76 - Validation scatterplots of CoastObs absorption-based PSC products in Ria de Vigo and Venice Lagoon. (a) Pico-phytoplankton Chl-*a*, (b) Nano-phytoplankton Chl-*a*, (c) Micro-phytoplankton Chl-*a*.

Table 43 - Error metrics for absorption-based PSC CoastObs product

Region	Product	R^2	slope	$RMSE_{log}$	$Bias_{log}$	MAE_{log}	MAPE %	N
Ria de Vigo, Spain	Pico-phytoplankton Chl-*a* *	NA	NA	NA	NA	NA	NA	0
	Nano-phytoplankton Chl-*a*	0.95	0.61	0.186	0.005	0.173	32.6	5
	Micro-phytoplankton Chl-*a*	0.70	1.11	0.142	0.033	0.118	29.8	4
Venice Lagoon and Adriatic Sea, Italy	Pico-phytoplankton Chl-*a*	0.14	0.87	0.127	-0.087	0.095	18.3	8
	Nano-phytoplankton Chl-*a*	0.25	0.24	0.234	-0.229	0.229	40.6	8
	Micro-phytoplankton Chl-*a*	0.13	0.47	0.470	0.464	0.464	195.5	8

* Note there were no pico-phytoplankton present in *in situ* samples for the Vigo 2018 dataset, therefore validation results cannot be presented at this time.

This project has received funding from the European Union's Horizon 2020 research and innovation programme under grant agreement No 776348

3.2.3 Primary Production (PP)

The data and method for this product was presented in the Primary Productivity Product Documentation (D 3.5), however additional data and methods are presented with regard to fast repetition rate fluorometry method for for *in situ* PP measurements made in 2019.

3.2.3.1 In situ data and methods

Primary productivity data were validated using *in situ* data measured by the fast repeitition rate fluorometry (FRRf) method in the Venice and Vigo regions in summer 2019. Photosystem II (PSII) variable chlorophyll fluorescence parameters were measured using an Act2 laboratory system (Chelsea Technologies Ltd.), which illuminates samples in a series of steps to measure a fluorescence light curve (FLC). The excitation wavelengths of the Act2 light emitting diodes (LEDs) were 450, 530 and 624 nm (white). The Act2 instrument was used with a saturation phase comprising 100 flashlets an a 2µs pitch, with sample temperature maintained by a chiller to the *in situ* measured temperature. An aliquot of the sample was first run in automatic mode (Auto-FLC on), then a second aliquot was run in manual mode (Auto-FLC off) using the maximum energy (E) derived from automatic mode. IN this way, we ensured maximum fluorescence was reached. The minimum (F_0) and maximum (F_m) fluorescence were estimated by the Act2Run software (Chelsea Technologies Ltd) using the equations from in Kolber et al. (1998), while secondary analysis of FRRf and FLC data was based on the absorption method described by Oxborough et al. (2012).

Using the PSII electron flux calculated on a volume basis (JVPSII; mol e- m^{-3} day^{-1}) derived from the absorption algorithm, the FRRF-based carbon (C) fixation rates (PC_{FRRf}; mg C m^{-3} h^{-1}) were calculated as follows:

$$PC_{FRRf}(mg\ C\ m^{-3}h^{-1}) = JV_{PSII}/24 \times \varphi_{E:C} \times MW_C \times 1000 \qquad \text{Equation 38}$$

where $\varphi_{E:C}$ is the electron requirement for carbon fixation (mol e- mol C^{-1}), MW_c is the molecular weight of carbon (12.0107 g mol^{-1}), 24 is the conversion from days to hours, and 1000 is the conversion from grams to milligrams carbon. This method to derive carbon fixation rates was also employed in the coastal waters of the western English Channel (Keys et al., 2018) and Australia (Robinson et al. 2014). Chl-*a* specific carbon fixation rates were then calculated by dividing PC by the measured Chl-*a* concentration at each station (analysis by higher performance liquid chromatography; HPLC).

The value implemented for $\varphi_{E:C}$ was 20 mol e- mol C^{-1} for both the Venice and Vigo datasets, slightly higher than the mean for a range of datasets found in Lawrenz et al. (2013; 10.3 mol e- mol C^{-1}). There is ongoing research into the variability of $\varphi_{E:C}$, as it can vary as a function of the prevailing phytoplankton taxa present (Suggett et al. 2009; Robinson et al. 2014) or environmental conditions, including temperature, photosynthetically available radiation and nutrient availability (Lawrenz et al. 2013; Hughes et al, 2018; Zhu et al., 2019). As we were unable to measure this parameter during the CoastObs field campaigns, we have made the best use of literature in order to define this parameter and calculate PP from the Act2 FRRf data. Recent studies indicate higher $\varphi_{E:C}$ is correlated with higher mean daily PAR (E_0) (Zhu et al., 2019) and warmer, more nutrient-rich waters (Lawrenz et al., 2013). As the Vigo and Venice 2019 datasets were collected in coastal regions during the summer period, it is expected these conditions would be linked to a higher $\varphi_{E:C}$. Furthermore, higher $\varphi_{E:C}$ values have been found where more large phytoplankton cells are present (>10 µm Chl-*a*), and lower $\varphi_{E:C}$ values where pico-phytoplankton biomass is high (Hughes et al., 2018). Although we do not yet have cell size data available for Vigo and Venice 2019, in 2018 nano- + micro-phytoplankton comprised 81-100% of the samples and there were a higher proportion of micro-phytoplankton present in Vigo than Venice (37% versus 15%, respectively). Again, this suggests a higher $\varphi_{E:C}$ parameter should be used for the Venice and Vigo 2019 dataset, with perhaps a greater electron requirement for carbon fixation in Vigo than Venice. This is certainly an area for future research and further investigation into the natural variability of $\varphi_{E:C}$ is required. However, at this stage, we have employed a parameterisation of $\varphi_{E:C}$ to the best of our knowledge given the data and research available.

The maximum photosynthetic rates (P_{max}; mg C (mg Chl-*a*)$^{-1}$ h^{-1}), light utilisation efficiency (α; mg C (mg Chl-*a*)$^{-1}$ h^{-1}) and the light saturation point of photosynthesis (E_k; µmol photons m^{-2} s^{-1}) can be derived by fitting the Photosynthesis-Irradiance (P-E) curves to the Act2 data (PC_{FRRf} and E) for each station. In the case of the hyperbolic tangent model of Platt, Gallegos and Harrison (1980), the photosynthetic rate at saturation (P_s; mg C (mg Chl-*a*)$^{-1}$ h^{-1}) is determined rather than P_{max}, however if there is no inhibition these two parameters coincide. Additionally, the Platt et al (1980) model parameterises β, which characterises the photoinhibition effect, as opposed to deriving E_k. In addition to the benefit that it characterises photoinhibition, the Platt et al (1980) model has previously been applied to coastal waters in other studies (e.g. Robinson et al. 2014; Silsbe and Kromkamp, 2012). Thus, the Platt et al. (1980) model was implemented for the Act 2 data, as follows:

$$PC_{FRRf}\ (E) = P_s\ \times (1 - \exp(-\alpha \times E/P_s))\ \times \exp(-\beta \times E/P_s) \qquad \text{Equation 39}$$

K_d(PAR) and the mean daily sea surface PAR (E_0) were measured at each station, as detailed in Sections 3.1.5 and 0, respectively. Assuming *in situ* Chl-*a* concentrations were uniform throughout the water column, the phytoprod() function in R (phytotools package) was used to model the depth integrated primary productivity (PP_{eu}; mg C m^{-2} day^{-1}) as a function of K_d(PAR), E_0, Chl-*a* and max depth. If the maximum depth was less than the euphotic depth, the maximum depth was used for integration.

3.2.3.2 Performance of in situ m2VGPM

The m2VGPM model is a modified version of the Vertically Generalized Production Model (Behrenfeld and Falkowski, 1997), and is described in detail in the Primary Productivity product documentation (D3.5). The model is as follows:

$$PP_{eu} = 0.66125 * (P^{B}_{opt}) * (E_0/(E_0+4.1)) * Z_{eu} * \text{Chl-}a_s * D_{irr} \qquad \text{Equation 40}$$

The parameters for the *in situ* m2VGPM were defined as follows:

- P^B_{opt} = maximum C fixation rate (mg C mg Chl-*a* $^{-1}$ h^{-1}), modelled as a function of temperature (T) according to the General Lakes 3rd order polynomial function (INFORM project):

$$P^B_{opt} = 0.00137T^3 - 0.048T^2 + 0.6044T + 0.159 \qquad \text{Equation 41}$$

- E_0 = *in situ* daily sea surface photosynthetically available radiation (PAR; E m^{-2}), modelled from surface rates (E m^{-2} s^{-1}) using the incident() function in R
- Z_{eu} = euphotic depth (m) calculated from *in situ* K_d(PAR) profiles (Kirk, 1994)
- Chl-a_s = surface Chlorophyll-*a* concentration measured by HPLC
- D_{irr} = daily photoperiod, calculated as a function of latitude and day of year using geosphere package in R.

In order to first test the results of the *in situ* model, the m2VGPM PP_{eu} values were compared to the PP_{eu} data measured *in situ* by the Act2, with the scatterplots are shown in Figure 77.

This project has received funding from the European Union's Horizon 2020 research and innovation programme under grant agreement No 776348

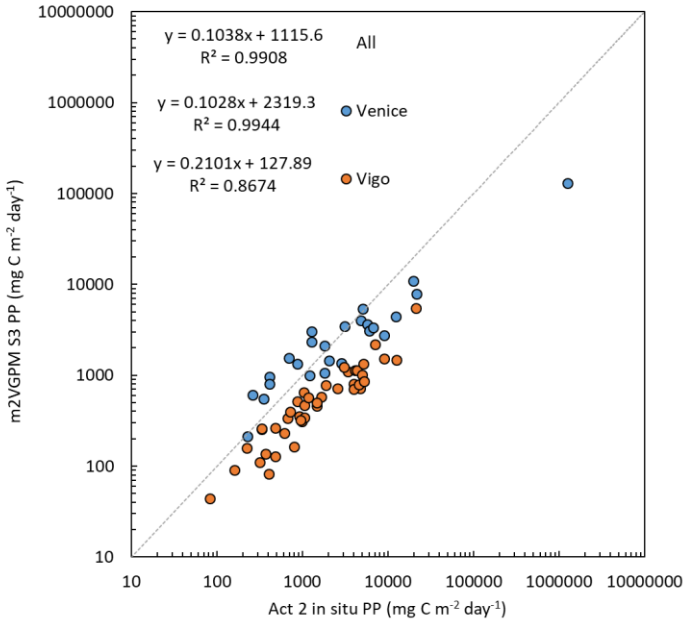

Figure 77 - Validation scatterplot for *in situ* m2VGPM depth integrated Primary Productivity (PP_{eu}) as a function of Act2 Primary Productivity, indicating R^2 and linear regression fit

Table 44 - Error metrics for *in situ* m2VGPM PP_{eu}

Region	Product	R^2	slope	$RMSE_{log}$	$Bias_{log}$	MAE_{log}	MAPE %	N
Ria de Vigo, Spain	Primary Productivity, PP_{eu} (mg C m^{-2} day^{-1})	0.867	0.210	0.338	0.0718	0.274	59.1%	42
Venice Lagoon, Italy	Primary Productivity, PP_{eu} (mg C m^{-2} day^{-1})	0.994	0.103	0.523	0.482	0.482	63.4%	25
All data	Primary Productivity, PP_{eu} (mg C m^{-2} day^{-1})	0.991	0.104	0.463	0.329	0.405	61.8%	67

It is clear that the the electron uptake requirement ($\varphi_{E:C}$) has a large influence on the conversion of Act2 FRRf data to carbon-fixation rates, and that this requires further research to better characterise this parameter and improve use of FRRf for *in situ* PP measurements. However, the high coefficient of determination (R^2) between Act2 and m2VGPM PP_{eu} indicates a good correlation between *in situ* and modelled data. Therefore we have confidence in using the m2VGPM for satellite data to derive PP_{eu}.

This project has received funding from the European Union's Horizon 2020 research and innovation programme under grant agreement No 776348

3.2.3.3 Satellite data and methods

The satellite derived data for use in testing the m2VGPM are as follows:

Sentinel-3 OLCI data

Level 1 full resolution (L1 FR) Sentinel-3 OLCI data were atmospherically corrected with the C2RCC processor. Cloud, land and coastline pixels were removed using the Idepix flags. Matchups with *in situ* PP_{eu} data were extracted +/-1 day of the satellite overpass for the 2019 dataset.

Chlorophyll-a (Chl-*a*)

The best performing Sentinel-3 OLCI Chl-*a* algorithm for the 2019 Vigo and Venice data was implemented in the satellite PP model (Normalised Difference Chlorophyll Index, NDCI; Mishra & Mishra, 2012). For 2018 Chl-*a* validation results see Section 3.1.2. We note that a different tuning was required for the 2019 dataset, which is due to the change in L1 processing impelemented by ESA in between the 2018 and 2019 datasets (https://sentinels.copernicus.eu/web/sentinel/technical-guides/sentinel-3-olci/processing-baseline). A new radiometric gain model was implemented on 10-Apr-2019, therefore a new tuning of the Chl-a was required as the 2018 model performed poorly (data not shown). The NDCI Chl-a validation results for 2019 are shown below for same-day matchups (Figure 78 and Table 45).

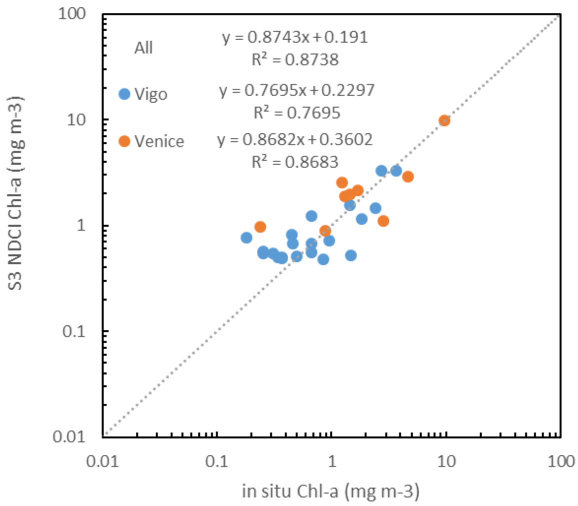

Figure 78 - Validation scatterplot for S3 NDCI Chl-a product tuned with the Vigo and Venice 2019 dataset, indicating R^2 and linear regression fit

This project has received funding from the European Union's Horizon 2020 research and innovation programme under grant agreement No 776348

Table 45 - Error metrics for 2019 NDCI Chl-a product

Region	R^2	slope	$RMSE_{log}$	$Bias_{log}$	MAE_{log}	MAPE %	N
Ria de Vigo, Spain	0.770	0.770	0.300	0.00278	0.239	64.4%	21
Venice Lagoon, Italy	0.868	0.868	0.286	-0.0777	0.215	69.0%	9
All data	0.874	0.874	0.296	-0.0214	0.232	65.8%	30

Sea Surface Temperature (SST) data were acquired for use in the satellite primary production product. These data were downloaded on 27/9/2019 from the GHRSST (https://www.ghrsst.org/ghrsst-data-services/products/). SST data were provided as a L4 gridded product, which is generated by combining complementary satellite and *in situ* observations within Optimal Interpolation systems. Validation results for the SST product are shown in Section 3.1.4.

Euphotic Depth (Z_{eu}) was derived from the Sentinel-3 C2RCC product as an exponential function of the ratio between R_{rs} at 560 and 490 nm. Validation results for Z_{eu} are provided in Section 3.1.5.

Daily irradiance (E_0) were acquired from the EUMETSAT data centre (https://archive.eumetsat.int/usc/) on 03/10/2019 from SEVIRI onboard the geostationary satellite Meteosat (9/10/11). The SSI (Shortwave solar irradiance) product was tuned to the 2019 *in situ* dataset as follows. See Section 0 for E_0 validation results.

Thus, the parameters for the *satellite* m2VGPM were defined as follows:

- P^B_{opt} = maximum C fixation rate (mg C mg Chl-a^{-1} h^{-1}), modelled as a function of the GHRSST L4 temperature (T) according to the General Lakes 3rd order polynomial function (INFORM project):

$$P^B_{opt} = 0.00137T^3 - 0.048T^2 + 0.6044T + 0.159 \qquad \text{Equation 42}$$

- E_0 = *in situ* daily sea surface photosynthetically available radiation (PAR; E m^{-2}), derived from Meteosat SSI data
- Z_{eu} = euphotic depth (m) derived from Sentinel-3 C2RCC product
- Chl-a_s = satellite Chlorophyll-*a* concentration derived from Sentinel-3 C2RCC product

This project has received funding from the European Union's Horizon 2020 research and innovation programme under grant agreement No 776348

- D_{irr} = daily photoperiod, calculated as a function of latitude and day of year using geosphere package in R *(note this is not a satellite derived parameter)*

3.2.3.4 Performance of satellite m2VGPM

Results for the satellite m2VGPM are shown in Figure 79, with errors presented in Table 46. Overall, the satellite model performed well when compared to *in situ* PP derived from FRRf (Act2). However, again, we emphasize that the *in situ* FRRf results require further investigation with regard to better characterising the $\phi_{E:C}$ parameter for each region. Furthermore, for application of this model to other regions, it is of importance to ensure the Chl-*a* algorithm performs well, as this could propagate error towards the satellite derived PP_{eu}. We also note there is a relatively small matchup dataset (n=21), as we were limited to the data collected during the 2019 field campaigns. Thus, we intend to collect *in situ* FRRf PP measurements in the Netherlands coastal waters during 2020 to increase our confidence in this product and the sample size.

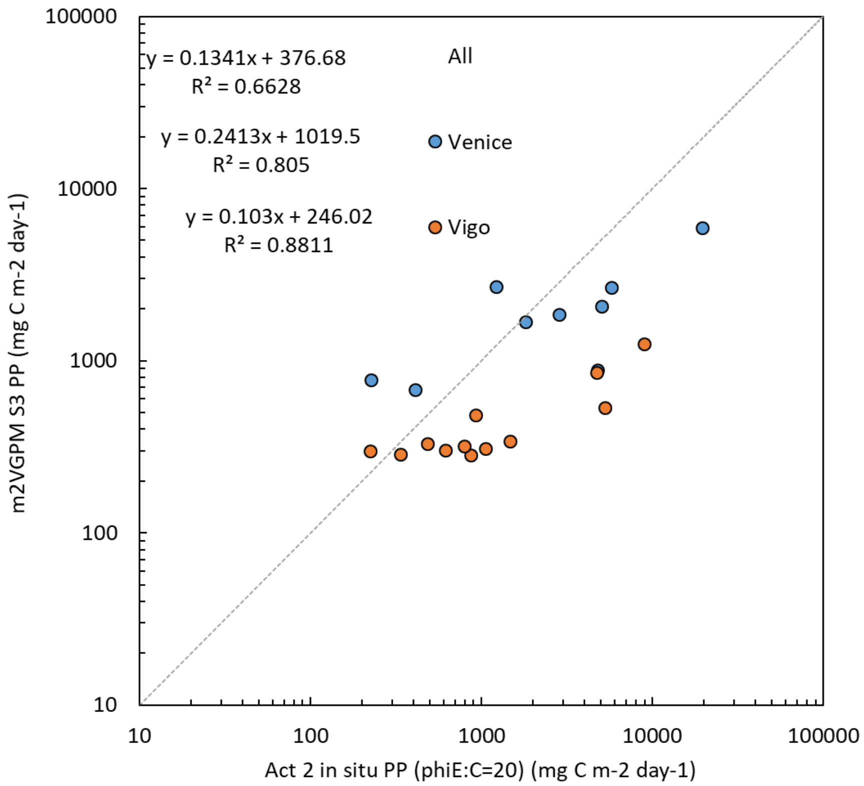

Figure 79 - Validation scatterplot for the Primary Productivity (PP_{eu}) CoastObs product, indicating R^2 and linear regression fit (note for Act2 *in situ* PP, $\phi_{E:C}$= 20 mol e- mol C^{-1}).

This project has received funding from the European Union's Horizon 2020 research and innovation programme under grant agreement No 776348

Table 46 - Error metrics for satellite m2VGPM PP_{eu} product (2019 dataset)

Product	R^2	slope	$RMSE_{log}$	$Bias_{log}$	MAE_{log}	MAPE (%)	N
Ria de Vigo, Spain	0.881	0.103	0.545	0.444	0.466	59.3%	12
Venice Lagoon and Adriatic Sea, Italy	0.805	0.241	0.415	0.121	0.365	81.4%	9
All	0.663	0.134	0.494	0.306	0.423	68.8%	21

An example map of PP derived from the S3 C2RCC OLCI, Meteosat and GHRSST datasets is shown in Figure 80. Each satellite product was reprojected to UTM/WGS84, and the Metosat and GHRSST datasets were resampled to a 348m pixel size to match the S3 OLCI dataset. PPeu was calculated with the m2VGPM, using the bandmath function in SNAP v.6.0.

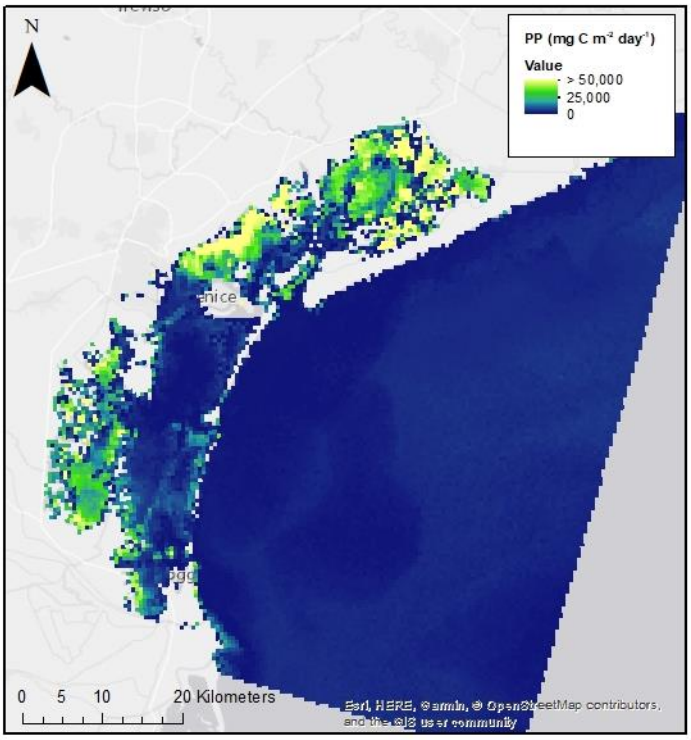

Figure 80 - Example map of PP_{eu} CoastObs product for the Venice Lagoon, Italy, 16.07.2019

3.2.4 Harmful Algal Blooms and Indicator Species (HABs)

Data and methods for HABs products were presented in the Harmful Algae Bloom Species Product Documentation (D 3.6). Species indicators were developed for two taxonomic groups: *Pseudo-nitzschia* spp. and *Alexandrium minutum*.

Species indicators for *Alexandrium minutum* based on Sentinel-2 and Sentinel-3 images were developed and validated using a dataset between May and August 2018 (see D 3.6 for details). Data of this species after August 2018 were not available for further validation, and hence it was not included in this deliverable.

The species indicator for *Pseudo-nitzschia* spp. is based on a Support Vector Machine (SVM) “bloom”/”no bloom” probability model developed using a match-ups dataset consisting of 383 data points from 34 Sentinel-3 images between May 2016 and November 2018. It contains 67 “bloom” situations and 316 “no bloom”.

Abundance of *Pseudo-nitzschia* spp. between December 2018 and April 2019 were available for further validation from the INTECMAR monitoring program. Unfortunately, although abundances lower than 10^5 cell/L were detected (in 51 of 168 data points), only there were two blooms (abundances greater than 10^5 cell/L).

After the match-ups analysis, only 32 valid data points, all “no bloom”, were available. The application of the *Pseudo-nitzschia* spp. species indicator produced a perfect result, i.e. 32 of 32 data points were correctly classified as “no bloom”.

Table 47 - A confusion matrix indicating instances of true positives (TP), true negatives (TN), false positives (FP) and false negatives (FN). It was obtained applying the *Pseudo-nitzschia* spp. indicator to the complete dataset (development + test).

		Actual Class (*in situ* data)	
		Bloom	No bloom
Predicted Class (EO data)	Bloom	*62*	*15*
	No bloom	*5*	*333*

Table 47 shows the confusion matrix obtained from applying the Support Vector Machine (SVM) probability model to the complete dataset, including the development dataset (67 “bloom”/316 “no bloom”) and the independent test dataset (32 “no bloom”). Note that metrics were not computed from the test dataset because it only contains “no bloom”. Since probability

This project has received funding from the European Union’s Horizon 2020 research and innovation programme under grant agreement No 776348

outputs (between 0 and 1) are used, the confusion matrix was obtained using an optimal threshold maximizing the sum *TPR + TNR*.

Table 48 shows the error metrics for the *Pseudo-nitzschia* spp. indicator computed from the cross-validation process (see D 3.6) and from the development and complete (development + test) datasets. Results are quite similar evidencing the robustness of the model. Note that the complete dataset includes 32 extra "no bloom", which are correctly classified leading to a slight improvement of *FNR* and *kappa*.

Table 48 - Error metrics for the *Pseudo-nitzschia* spp. indicator

Datasets	*TPR*	*FNR*	*Overall Accuracy*	*Kappa*	*AUC*
Cross-Validation	0.90	0.10	0.90	0.87	0.95
Development	0.93	0.05	0.95	0.94	0.97
Development + Test	0.93	0.04	0.95	0.95	0.97

Although this species indicator requires a further validation using an independent test dataset including blooms, the model is very robust and produces reliable results with a good balance between TPR and FPR, i.e. it is able to identify correctly more than 90% of blooms with a false alarm rate lower than 5 %.

Figure 81 shows an example of a bloom probability map obtained using the *Pseudo-nitzschia* spp. indicator.

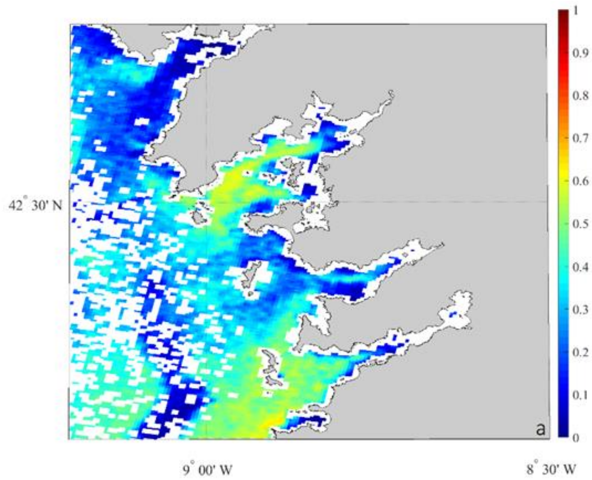

Figure 81 - Bloom probability map on 1 August 2018 obtained using the *Pseudo-nitzschia* spp. indicator.

3.3 Higher level products

The CoastObs higher level products and methods were described in detail in D3.8 Higher Level Products Report. These include phytoplankton bloom phenology, sediment plume morphology, coastal erosion and accretion, water framework directive reporting, and integration of EO products with modelling (mussel culture potential and harmful algal bloom forecasting). The foundation for these are the basic and innovative products, and these are validated in the previous sections, 3.1 and 3.2. However, some additional product detail and validation results are presented here for the mussel culture potential higher level CoastObs product.

3.3.1 Integration with modelling: mussel culture potential

This higher-level product to identify the spatial temporal dynamics in mussel growth integrates CoastObs S3 basic products with the DEB theory, with the overall aim of predicting mussel culture potential in Dutch case study areas and for Dutch users to be used as a tool for optimization of production efficiency.

A standard DEB model developed by Wijsman (2019) was used here, describing energy flow in mussels focusing on food assimilation and utilization for maintenance, growth and reproduction. The parameter set for *Mytilus edulis* specifically adapted for Dutch cultivation areas was also derived from Wijsman (2019). Simulations were conducted using an R-script, computing daily energy flows as a function of temperature (SST in degrees Celsius) and the food related variables Chl-*a* ($mg.m^{-3}$) and TSM ($g.m^{-3}$). From the S3 basic products, time series for SST, Chl-*a* and TSM were extracted for each pixel coordinate (resolution 300x300m) in the study areas Oosterschelde and western Wadden Sea. Missing values in time series resulting from missing images or cloud covered pixels were interpolated linearly to create a daily sequence and were used as forcing in the model.

The model was run for both 2017 and 2018 from April-October, starting with mussel seed sizes of 3.0 and 3.6 cm for 2017 and 2018, respectively. The model was then calibrated by adjusting the half saturation coefficient for food uptake for the different regions within a study area (for workflow steps and calibration details see D3.8). A validation dataset of mussel growth measurements in the field was obtained from INNOPRO (2018) - funded by the European Maritime and Fisheries Fund - where growth of blue mussels (*Mytilus edulis*) was measured from April to October in 2017 & 2018 at 12 locations in the Wadden Sea and 12 locations in the Oosterschelde.

Evaluation of goodness of fit was done by linear regression between observations in shell length (cm) and simulated length. The first values were excluded.

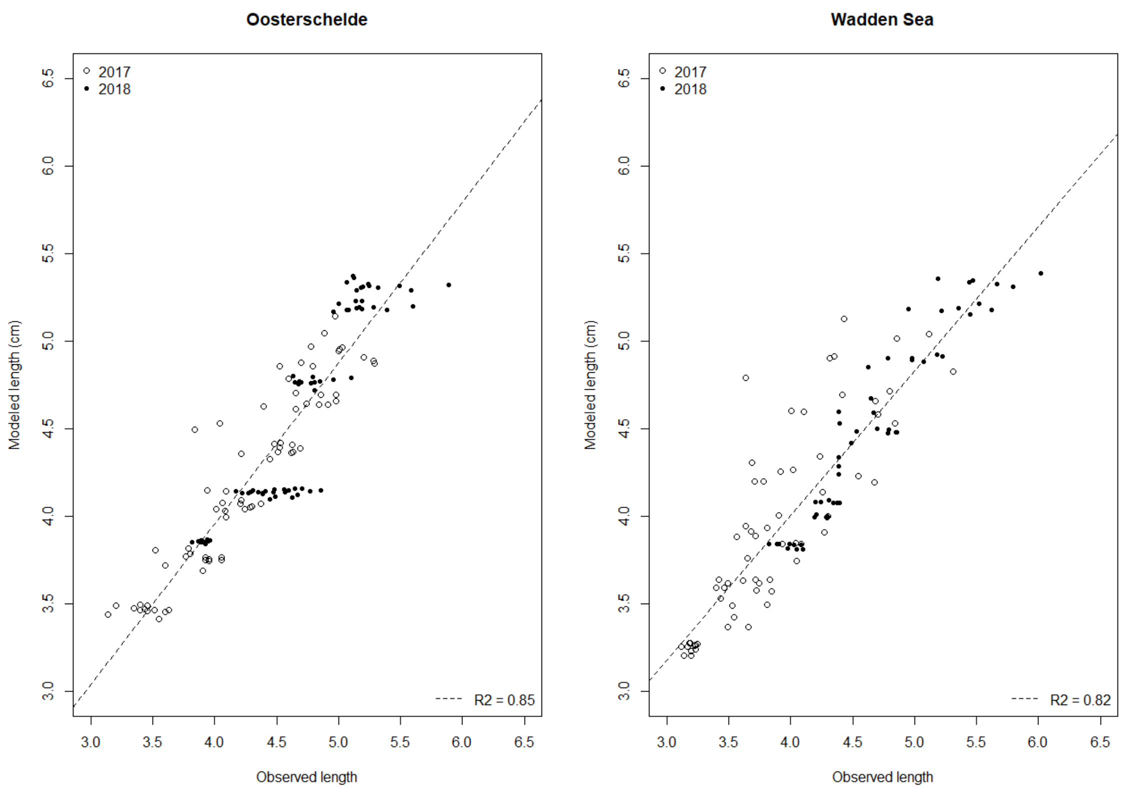

Figure 82 - Validation scatterplots for modeled shell length output (cm) from the spatio temporal mussel growth DEB model and observed growth in the Oosterschelde estuary and Wadden Sea, indicating R^2 and linear regression fit. Open circles represent 2017 data, black circles 2018 data.

Table 49 - Error metrics for higher level CoastObs product Spatio temporal DEB model for mussel growth

Spatio temporal DEB model for mussel growth	R^2	slope	RMSE_log	Bias_log	MAE_log
Oosterschelde estuary	0.85	0.90	0.054	0.014	0.041
Wadden Sea	0.82	0.86	0.068	-0.002	0.053

The integration of S3 spatial raster data of food variables and water temperature with an existing DEB model provide promising results. With an overall R^2 of 0.82 for the Wadden Sea

This project has received funding from the European Union's Horizon 2020 research and innovation programme under grant agreement No 776348

and 0.85 for the Oosterschelde estuary, the model already performs well (for error metrics see Table 49).

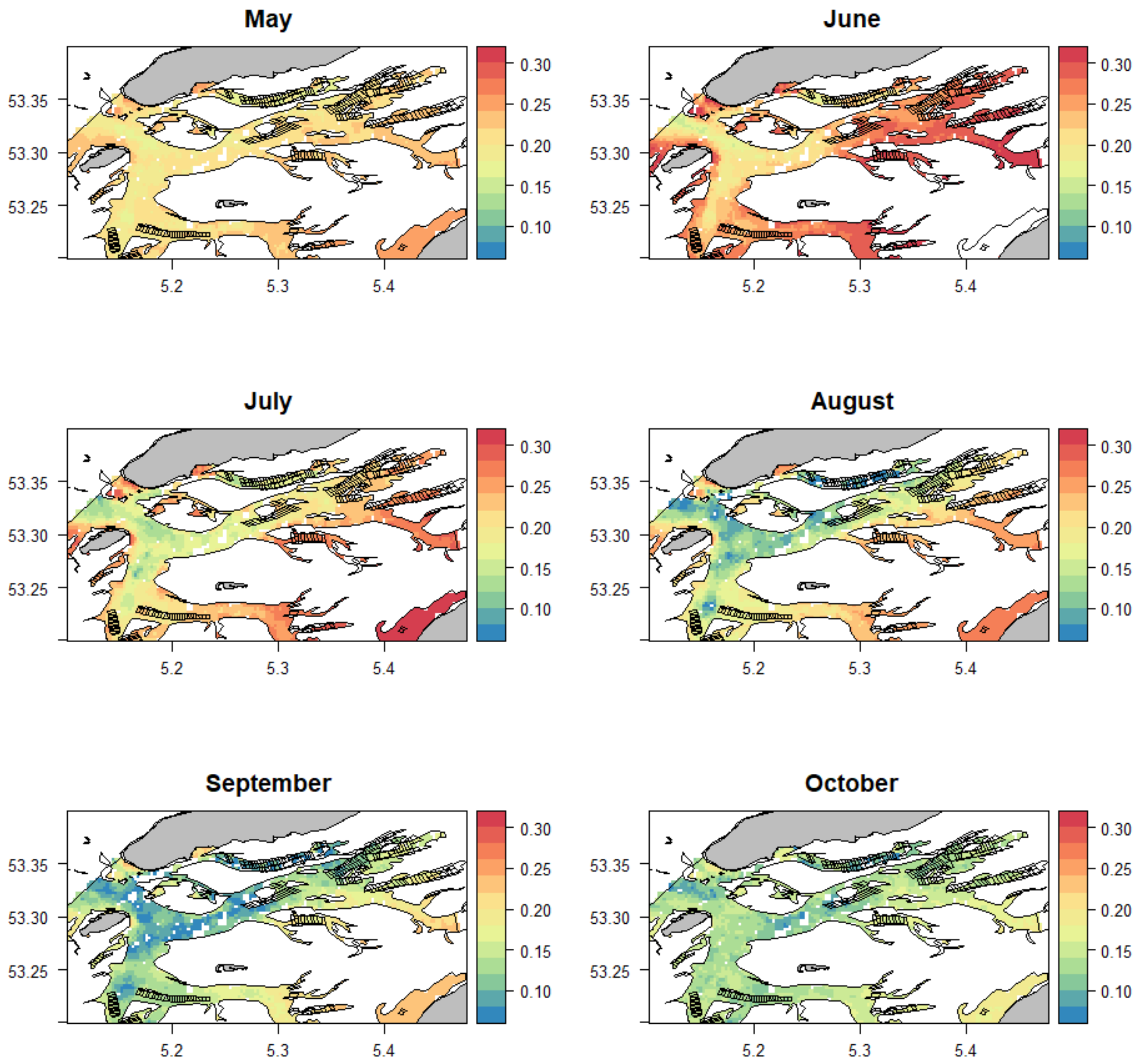

Figure 83 - Example of monthly aggregates from DEB model outputs transformed to relative growth rate (lenght increase in %) for the Wadden Sea in 2018

This project has received funding from the European Union's Horizon 2020 research and innovation programme under grant agreement No 776348

4 References

Behrenfeld, M.J. and Falkowski, P.G. (1997) Photosynthetic rates derived from satellite-based chlorophyll concentration. Limnology and Oceanography, 42(1): 1-20.

Braga, F., Zaggia, L., Bellafiore, D., Bresciani, M., Giardino, C., Lorenzetti, G., Maicu, F., Manzo, C., Riminucci, F., Ravaioli, M., Brando, V.E. (2017) Mapping turbidity patterns in the Po river prodelta using multi-temporal Landsat 8 imagery. Estuar. Coast. Mar. Sci. 198, 555-567.

Brando, V.E., Braga, F., Zaggia, L., Giardino, C., Bresciani, M., Matta, E., Bellafiore, D., Ferrarin, C., Maicu, F., Benetazzo, A., Bonaldo, D., Falcieri, F.M., Coluccelli, A., Russo, A., Carniel, S. (2015) High-resolution satellite turbidity and sea surface temperature observations of river plume interactions during a significant flood event. Ocean Sci. 11 (6), 909-920.

Brockmann, C., Doerffer, R., Peters, M., Stelzer, K., Embacher, S., Reuscas, A. (2016) Evolution of the C2RCC neural network for Sentinel 2 and 3 fo rthe retrieval of ocean colour products in normal and extreme optically complex waters, Proc. Living Planet Symposium, Prague, Czech Republic, 9-13 May 2016.

Dall'Olmo, G., Gitelson, A. A., & Rundquist, D. C. (2003). Towards a unified approach for remote estimation of chlorophyll‐a in both terrestrial vegetation and turbid productive waters. Geophysical Research Letters, 30(18).

De Keukelaere, L., Sterckx, S., Adriaensen, S., Knaeps, E., Reusen, I., Giardino, C., Bresciani, M., Hunter, P., Neil, C., Van der Zande, D. and Vaiciute, D. (2018). Atmospheric correction of Landsat-8/OLI and Sentinel-2/MSI data using iCOR algorithm: validation for coastal and inland waters, European Journal of Remote Sensing, 51(1): 525-542.

Doerffer, R., Schiller, H., (2008). MERIS regional coastal and lake case 2 water project atmospheric correction ATBD.

Dogliotti, A. I., Ruddick, K. G., Nechad, B., Doxaran, D., Knaeps, E. (2015) A single algorithm to retrieve turbidity from remotely-sensed data in all coastal and estuarine waters. Remote Sens. Environ., 156, 157-168.

Gernez, P., Doxaran, D., & Barillé, L. (2017). Shellfish aquaculture from space: potential of Sentinel2 to monitor tide-driven changes in turbidity, chlorophyll concentration and oyster physiological response at the scale of an oyster farm. Frontiers in Marine Science, 4, 137.

Gitelson, A. A., Gao, B. C., Li, R. R., Berdnikov, S., & Saprygin, V. (2011). Estimation of chlorophyll-a concentration in productive turbid waters using a Hyperspectral Imager for the Coastal Ocean—the Azov Sea case study. Environmental Research Letters, 6(2), 024023.

This project has received funding from the European Union's Horizon 2020 research and innovation programme under grant agreement No 776348

Gitelson, A. A., & Kondratyev, K. Y. (1991). Optical models of mesotrophic and eutrophic water bodies. International Journal of Remote Sensing, 12(3), 373-385.

Gons, H. J., Auer, M. T., & Effler, S. W. (2008). MERIS satellite chlorophyll mapping of oligotrophic and eutrophic waters in the Laurentian Great Lakes. Remote Sensing of Environment, 112(11), 4098-4106.

Gons, H. J., Rijkeboer, M., & Ruddick, K. G. (2005). Effect of a waveband shift on chlorophyll retrieval from MERIS imagery of inland and coastal waters. Journal of Plankton research, 27(1), 125-127.

Hommersom, A., Peters, S., Wernand, M.R. and de Boer, J. (2009) Spatial and temporal variability in bio-optical properties of the Wadden Sea. Estuarine, Coastal and Shelf Science 83(3): 360–370.

Hu, C., Lee, Z., & Franz, B. (2012). Chlorophyll aalgorithms for oligotrophic oceans: A novel approach based on three - band reflectance difference. Journal of Geophysical Research: Oceans, 117(C1).

Hughes, D., Varkey, D., Doblin, M. A., Ingleton, T., Mcinnes, A., Ralph, P. J., et al. (2018). Impact of nitrogen availability upon the electron requirement for carbon fixation in Australian coastal phytoplankton communities. Limnol. Oceanogr. 63, 1891–1910. doi: 10.1002/lno.10814

INNOPRO (2018) Mussel growth results - Funded by European Maritime and Fisheries Fund, Innovatie en rendementsverbetering mosselproductie (INNOPRO) - WUR. Available at: https://www.wur.nl/en/project/Innovatie-en-rendementsverbetering-mosselproductie-INNOPRO.htm (Accessed: 14 August 2019).

IOCCG (2006). Remote Sensing of Inherent Optical Properties: Fundamentals, Tests of Algorithms, and Applications. Lee, Z.-P. (ed.), Reports of the International Ocean-Colour Coordinating Group, No. 5, IOCCG, Dartmouth, Canada.

IOCCG (2018). IOCCG Ocean Optics and Biogeochemistry Protocols for Satellite Ocean Colour Sensor Validation; Volume 1.0. Inherent Optical Property Measurements and Protocols: Absorption Coefficient (eds. Neeley, A. R. and Mannino, A.). Dartmouth, NS, Canada.

Keys, M., Tilstone, G., Findlay, H.S., Widdicombe, C.E., Lawson, T. (2018) Effects of elevated CO2 and temperature on phytoplankton community biomass, species composition and photosynthesis during an experimentally induced autumn bloom in the western English Channel, Biogeosciences (15): 2303-3222.

Kirk, J. T. O. (1994), Light and Photosynthesis in Aquatic Ecosystems, Cambridge Univ. Press, New York.

This project has received funding from the European Union's Horizon 2020 research and innovation programme under grant agreement No 776348

Kleywegt, G.J., 2007. Quality control and validation. In Macromolecular crystallography protocols (pp. 255-272). Humana Press.

Kolber, Z.S., Prasil, O;., Falkowski, P.G. (1998) Measurements of variable chlorophyll fluorescence using fast repetition rate techniques: defining methodology and experimental protocols, Biochimica et a Biophysica Acta (BBA) – Bioenergetics, 1367(1-3): 88-106.

Lawrenz, E., Silsbe, G., Capuzzo, El., Ylostalo, P., Forster, R.M., Simis, S.G.H., Prasil, O., Kromkamp, J.C., Hickman, A.E., Moore, C.M., Forget, M., Geider, R.J., Suggett, D.J. (2013) Predicting the electron requirement for carbon fixation in seas and oceans. PLoS One 8: e58137.

Lebreton., C., Stelzer, K., Brockmann, C., Bertels, L., Pringle, N., Paperin, M., Danne, O., Knaeps, E., Ruddick., K. (2016). Cloud and Cloud Shadow masking of high and medium resolution optical sensors –an algorithm inter-comparisonexample for Landsat 8. Proceedings of ESA Living Planet Symposium, Prague, 9-13 May 2016.

Lee, Z. (2014). Update of the Quasi-Analytical Algorithm (QAA_v6). http://www.ioccg.org/groups/software.html

Lee, Z., Carder, K. L., Arnone, R. A. (2002). Deriving inherent optical properties from water color: a multiband quasi-analytical algorithm for optically deep waters. Applied optics, 41(27), 5755-5772.

Main-Knorn, M., Pflug, B., Louis, J., Debaecker, V., Müller-Wilm, U., & Gascon, F. (2017, October). Sen2Cor for Sentinel-2. In Image and Signal Processing for Remote Sensing XXIII (Vol. 10427, p. 1042704). International Society for Optics and Photonics.

Mishra, S. And Mishra, D.R. (2012) Normalized difference chlorophyll index: A novel model for remote estimation of chlorophyll-a concentration in turbid productive waters, Remote Sensing of Environment, 117: 394-406.

Moses, W. J., Gitelson, A. A., Berdnikov, S., & Povazhnyy, V. (2009). Estimation of chlorophyll-a concentration in case II waters using MODIS and MERIS data—successes and challenges. Environmental Research Letters, 4(4), 045005.

Nechad, B., Ruddick, K.G., Neukermans, G. (2009) Calibration and validation of a generic multisensor algorithm for mapping of turbidity in coastal waters. Proc. of SPIE 7473. Remote Sens. of the Ocean, Sea Ice, and Large Water Regions 2009 7473, 11.

Nechad, B., Ruddick, K. G., & Park, Y. (2010). Calibration and validation of a generic multisensor algorithm for mapping of total suspended matter in turbid waters. Remote Sensing of Environment, 114(4), 854-866.

Nechad, B.; van der Zande, D.; Hieronymi, M.; Kraseman, H.; Mueller, D.; Stenimetz, F.; Tilstone, G.; Simis, S.; Brockmann, C.; Ruescas, A.; et al. (2017) C2X Product Validation Report; Technical Report; ESA: Paris, France.

Novoa, S., Doxaran, D., Ody, A., Vanhellemont, Q., Lafon, V., Lubac, B., & Gernez, P. (2017). Atmospheric corrections and multi-conditional algorithm for multi-sensor remote sensing of suspended particulate matter in low-to-high turbidity levels coastal waters. Remote Sensing, 9(1), 61.

Park, Y. J., & Ruddick, K. (2005). Model of remote-sensing reflectance including bidirectional effects for case 1 and case 2 waters. Applied Optics, 44(7), 1236-1249.

Platt, T. G. C. L., Gallegos, C. L., & Harrison, W. G. (1980). Photoinhibition of photosynthesis in natural assemblages of marine phytoplankton.O'Reilly, J.E., & 24 co-authors (2000). SeaWiFS Postlaunch Calibration and Validation Analyses, Part 3. NASA Tech. Memo. 2000-206892, Vol. 11, S.B. Hooker and E.R. Firestone, Eds., NASA Goddard Space Flight Center, 49 pp.

Oxborough et al (2012). Direct estimation of functional PSII reaction center concentration and PSII electron flux on a volume basis: a new approach to the analysis of Fast Repetition Rate fluorometry (FRRf) data, Limnology and Oceanography – Methods, 10(3): 142-154.

Pahlevan, N., Lee, Z., Wei, J., Schaaf, C. B., Schott, J. R., & Berk, A. (2014) On-orbit radiometric characterization of OLI (Landsat-8) for applications in aquatic remote sensing. Remote Sens. Environ., 154, 272-284.

Pahlevan, N., Chittimalli, S. K., Balasubramanian, S. V., & Vellucci, V. (2019) Sentinel-2/Landsat-8 product consistency and implications for monitoring aquatic systems. Remote Sens. Environ., 220, 19-29.

Pierson, D.C., Kratzer, S., Strombeck, N. And Hakansson, B. (2008) Relationship between the attenuation of downwelling irradiance at 490 nm with the attenuation of PAR (400 nm-700 nm) in the Baltic Sea, Remote Sensing of Environment, 112(3) 668-680.

Qin, P., Simis, S.G.H., Tilstone G.H. (2017). Radiometric validation of atmospheric correction for MERIS in the Baltic Sea based on continuous observations from ships and AERONET-OC, Remote Sens. Environ., 200: 263-280.

Robinson, C., D. J. Suggett, N. Cherukuru, P. J. Ralph, and M. A. Doblin. (2014) Performance of fast repetition rate fluorometry based estimates of primary productivity in coastal waters. J. Mar. Syst. 139: 299–310.

Roettgers, R., Doerffer, R., McKee, D., Schoenfeld W. (2011) Pure water spectral absorption, scattering, and real part of refractive index model: ATBD, ESA Water Radiance Project.

This project has received funding from the European Union's Horizon 2020 research and innovation programme under grant agreement No 776348

Roy, R., Pratihary, A., Narvenkar, G., Mochemadkar, S., Gauns, M., Naqvi, S. W. A. (2011). The relationship between volatile halocarbons and phytoplankton pigments during a Trichodesmium bloom in the coastal eastern Arabian Sea. Estuarine, Coastal and Shelf Science, 95(1), 110-118.

Roy, S., Sathyendranath, S., Bouman, H., Platt, T. (2013). The global distribution of phytoplankton size spectrum and size classes from their light-absorption spectra derived from satellite data. Remote sensing of environment, 139, 185-197.

Silsbe, G.M. and Kromkamp, J.C. (2012) Modeling the irradiance dependency of the quantum efficiency of photosynthesis, Limnology and Oceanography: Methods, 10: 645-652.

Simis, S.G.H., & Olsson, J. (2013). Unattended processing of shipborne hyperspectral reflectance measurements. Remote Sensing of Environment, 135, 202-212.

Steinmetz, F., Deschamps, P.-Y. and Ramon D. (2011) Atmospheric correction in presence of sun glint: application to MERIS, Opt. Express 19, 9783-9800.

Sterckx, S., Knaeps, E., Adriaensen, S., Reusen, I., Keukelaere, L.D., & Hunter, P. (2015). Opera : An atmospheric correction for land and water. Proceedings of the Sentinel-3 for Science Workshop, (1), 3–6.

Suggett, D. J., H. L. Macintyre, T. M. Kana, and R. J. Geider. (2009) Comparing electron transport with gas exchange: Parameterising exchange rates between alternative photosynthetic currencies for eukaryotic phytoplankton. Aquat. Microb. Ecol. 56: 147–162.

Toming, K., Kutser, T., Uiboupin, R., Arikas, A., Vahter, K., & Paavel, B. (2017). Mapping water quality parameters with sentinel-3 ocean and land colour instrument imagery in the Baltic Sea. Remote Sensing, 9(10), 1070.

Vanhellemont, Q., (2019). Adaptation of the dark spectrum fitting atmospheric correction for aquatic applications of the Landsat and Sentinel-2 archives. Remote Sensing of Environment 225, 175–192. (https://doi.org/10.1016/j.rse.2019.03.010)

Vanhellemont, Q., Ruddick, K. (2018). Atmospheric correction of metre-scale optical satellite data for inland and coastal water applications. Remote Sens. Environ. (https://doi.org/10.1016/j.rse.2018.07.015)

Vanhellemont, Q., Ruddick, K. (2014). Turbid wakes associated with offshore wind turbines observed with Landsat 8. Remote Sens. Environ. 145, 105–115. (http://dx.doi.org/10.1016/j.rse.2014.01.009)

Vanhellemont, Q., Ruddick, K. (2015). Advantages of high quality SWIR bands for ocean colour processing: examples from Landsat-8. Remote Sens. Environ. 161, 89–106. (http://dx.doi.org/10.1016/j.rse.2015.02.007)

This project has received funding from the European Union's Horizon 2020 research and innovation programme under grant agreement No 776348

Vanhellemont Q. & Ruddick K. (2016). ACOLITE For Sentinel-2: Aquatic Applications of MSI imagery. Submitted for the proceedings of the 2016 ESA Living Planet Symposium held in Prague, Czech Republic, 9-13 May 2016, ESA Special Publication SP-740.

Vilas, L. G., Spyrakos, E., & Palenzuela, J. M. T. (2011). Neural network estimation of chlorophyll a from MERIS full resolution data for the coastal waters of Galician rias (NW Spain). Remote Sensing of Environment, 115(2), 524-535.

Wettle, M., Brando, V. E., 2006. SAMBUCA—Semi-analytical model for bathymetry, unmixing and concentration assessment. CSIRO Land and Water Science Report 22/06 Canberra: CSIRO Land and Water.

Wijsman, J. (2019) Dynamic Energy Budget (DEB) model Blue mussels (Mytilus edulis)- Technical report INNOPRO project.

Zhu, Y., Suggett, D., Liu, C., He, J., Lin, L., Le, F., ... & Hao, Q. (2019). Primary productivity dynamics in the summer Arctic Ocean confirms broad regulation of the electron requirement for carbon fixation by light-phytoplankton community interaction. Frontiers in Marine Science, 6, 275.

This project has received funding from the European Union's Horizon 2020 research and innovation programme under grant agreement No 776348